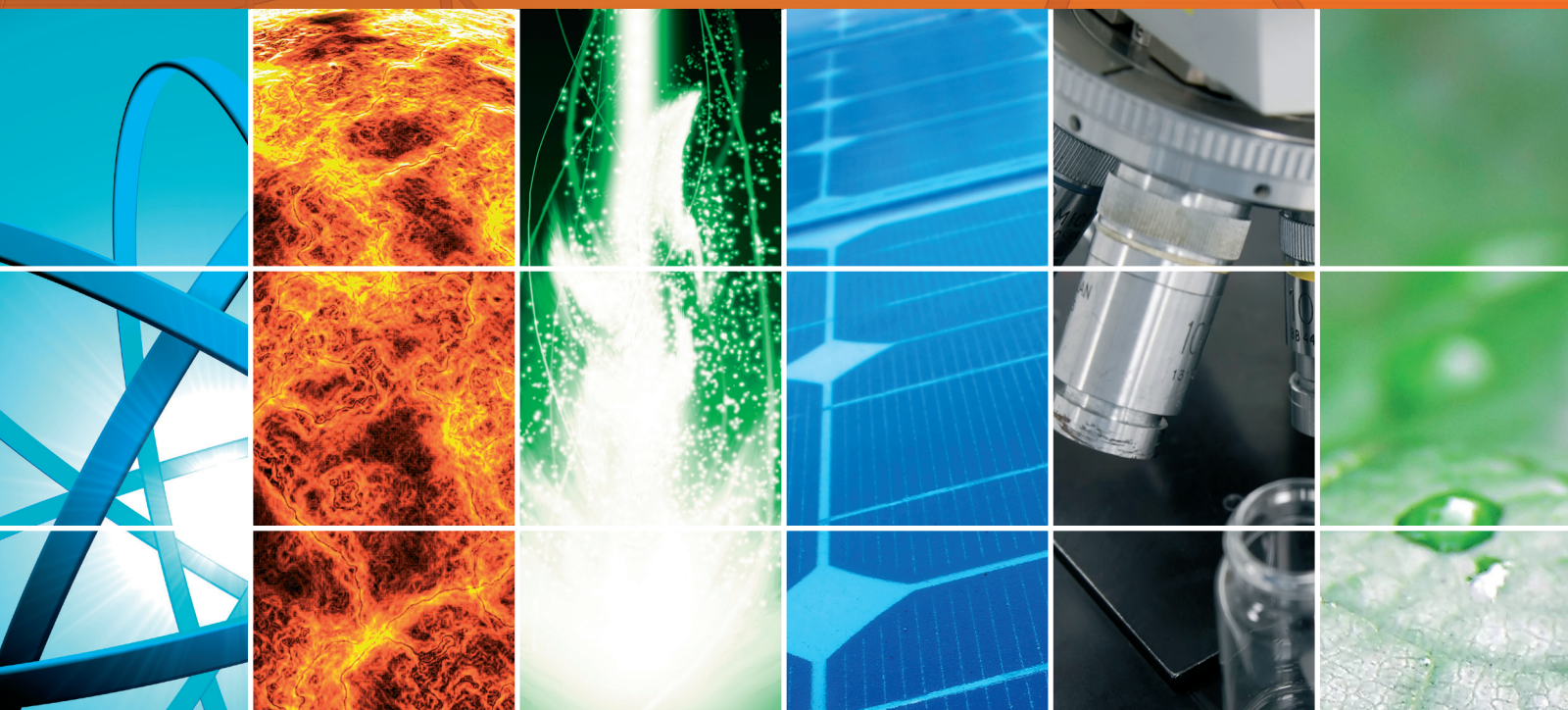


Solar Thermal Engineering

Lead Guest Editor: Alibakhsh Kasaeian

Guest Editors: Adel Mellit, Stoian Petrescu, and Michel Feidt





Solar Thermal Engineering

International Journal of Photoenergy

Solar Thermal Engineering

Lead Guest Editor: Alibakhsh Kasaeian

Guest Editors: Adel Mellit, Stoian Petrescu, and Michel Feidt



Copyright © 2017 Hindawi. All rights reserved.

This is a special issue published in "International Journal of Photoenergy." All articles are open access articles distributed under the Creative Commons Attribution License, which permits unrestricted use, distribution, and reproduction in any medium, provided the original work is properly cited.

Editorial Board

M. S.A. Abdel-Mottaleb, Egypt
Angelo Albini, Italy
Alberto Álvarez-Gallegos, Mexico
Vincenzo Augugliaro, Italy
Detlef W. Bahnemann, Germany
Simona Binetti, Italy
Fabio Bisegna, Italy
Thomas M. Brown, Italy
Joaquim Carneiro, Portugal
Yatendra S. Chaudhary, India
Věra Cimrová, Czech Republic
Juan M. Coronado, Spain
P. Davide Cozzoli, Italy
Dionysios D. Dionysiou, USA
Abderrazek Douhal, Spain
Mahmoud M. El-Nahass, Egypt
Polycarpos Falaras, Greece
Chris Ferekides, USA
Paolo Fornasiero, Italy
Manuel Fuentes Conde, Spain

Germà Garcia-Belmonte, Spain
Elisa Isabel Garcia-Lopez, Italy
Mohammed Ashraf Gondal, KSA
Giulia Grancini, Switzerland
Pierluigi Guerriero, Italy
Michael D. Heagy, USA
Wing-Kei Ho, Hong Kong
Jürgen Hüpkens, Germany
Tariq Iqbal, Canada
Adel A. Ismail, Kuwait
Chun-Sheng Jiang, USA
Cooper H. Langford, Canada
Manuel Ignacio Maldonado, Spain
Dionissios Mantzavinos, Greece
Santolo Meo, Italy
Claudio Minero, Italy
Antoni Morawski, Poland
Fabrice Morlet-Savary, France
Mohammad Muneer, India
Maria da Graça P. Neves, Portugal

Tsuyoshi Ochiai, Japan
Kei Ohkubo, Japan
Leonardo Palmisano, Italy
Thierry Pauporté, France
Philippe Poggi, France
Francesco Riganti Fulginei, Italy
Leonardo Sandrolini, Italy
Jinn Kong Sheu, Taiwan
Zofia Stasicka, Poland
Elias Stathatos, Greece
Jegadesan Subbiah, Australia
K. R. Justin Thomas, India
Nikolai V. Tkachenko, Finland
Ahmad Umar, KSA
Thomas Unold, Germany
Mark van Der Auweraer, Belgium
Wilfried G.J.H.M. Van Sark, Netherlands
Xuxu Wang, China
Yanfa Yan, USA
Jiangbo Yu, USA

Contents

Solar Thermal Engineering

Alibakhsh Kasaeian, Michel Feidt, Stoian Petrescu, and Adel Mellit
Volume 2017, Article ID 7493781, 2 pages

Effects of Ambient Parameters on the Performance of a Direct-Expansion Solar-Assisted Heat Pump with Bare Plate Evaporators for Space Heating

Wenzhu Huang, Jie Ji, Mawufemo Modjinou, and Jing Qin
Volume 2017, Article ID 3082740, 10 pages

Small-Scale Flat Plate Collectors for Solar Thermal Scavenging in Low Conductivity Environments

Emmanuel Ogbonnaya and Leland Weiss
Volume 2017, Article ID 7956879, 9 pages

A Solar Heating and Cooling System in a Nearly Zero-Energy Building: A Case Study in China

Zhifeng Sun, Yaohua Zhao, Wei Xu, Xinyu Zhang, Huai Li, Min Wang, Tao He, and Dongxu Wang
Volume 2017, Article ID 2053146, 11 pages

Thermal Storage Capacity and Night Ventilation Performance of a Solar Chimney Combined with Different PCMs

Jun Lu, Xiaolong Gao, Qianru Li, and Yongcai Li
Volume 2017, Article ID 8363190, 10 pages

Detailed Modeling of Flat Plate Solar Collector with Vacuum Glazing

Viacheslav Shemelin and Tomas Matuska
Volume 2017, Article ID 1587592, 9 pages

Performance Analysis of Photovoltaic Water Heating System

Tomas Matuska and Borivoj Sourek
Volume 2017, Article ID 7540250, 10 pages

Design and Optimization of Elliptical Cavity Tube Receivers in the Parabolic Trough Solar Collector

Fei Cao, Lei Wang, and Tianyu Zhu
Volume 2017, Article ID 1471594, 7 pages

Editorial

Solar Thermal Engineering

Alibakhsh Kasaeian,¹ Michel Feidt,² Stoian Petrescu,³ and Adel Mellit⁴

¹*Department of Renewable Energies, Faculty of New Sciences & Technologies, University of Tehran, Tehran, Iran*

²*Department of Physics and Mechanics, Faculty of Sciences and Technology, University Henri Poincaré, Nancy, France*

³*Department of Engineering Thermodynamics, Engines, Thermal and Refrigeration Equipments, University Politehnica of Bucharest, Bucharest, Romania*

⁴*Renewable Energy Laboratory, Jijel University, 1800 Jijel, Algeria*

Correspondence should be addressed to Alibakhsh Kasaeian; akasa@ut.ac.ir

Received 14 August 2017; Accepted 14 August 2017; Published 2 November 2017

Copyright © 2017 Alibakhsh Kasaeian et al. This is an open access article distributed under the Creative Commons Attribution License, which permits unrestricted use, distribution, and reproduction in any medium, provided the original work is properly cited.

The increasing demands to energy, from one side, and the global warming crisis of the world, from other side, are the reasons for developing renewable energies [1]. Among all resources of renewable energies, solar energy is the unlimited resource which can be exploited all over the world. The prices for solar generation technologies continue to rapidly decrease; so that, in some cases, the cost is competitive with the fossil fuel costs [2]. The thermal conversion of solar energy is possible by different collectors including flat and concentrating collectors. For the purpose of reaching large-scale energy conversion in both forms of electricity and thermal, the usage of different solar concentrating collectors would be a favorite selection [1]. Besides the application of solar flat and concentrating collectors, other kinds of energy conversion units have been focused by different researchers. For achieving wind and rotating turbines, solar chimneys would be a preferred option in the windless zones [3]. Also, for the purpose of supplying potable water, the solar stills have been developed in different types and designs [4].

In the recent years, in case of the application of solar thermal systems, the usage of special materials has been paid attention for increasing the efficiency. For instance, using of nanofluids has been the subject of research by many researchers [5]. Nanofluids are capable to enhance the heat transfer coefficient of the working fluids, which are circulating through the absorber tubes of the solar thermal units. Also, the phase change materials (PCMs) are another materials which have found a special situation in the solar

thermal systems. PCMs can store/release a large amount of heat during melting/solidification or gasification/liquefaction processes. Since the phase-transition enthalpy of PCMs is usually much higher than sensible heat, latent heat storage has much higher storage density than sensible heat storage [6]. So, this case will be another potential for the future studies in the field of solar thermal energy.

Regarding the importance of solar energy as the main sustainable resource among all renewable resources, it was interesting to gather the research findings of this subject in a special issue. The issue covers all new research articles about solar radiation and solar thermal energy systems. The aim was focused on the thermal conversion aspect of solar energy. So, the conversion systems including flat collecting and concentrating systems were gathered in this issue. Besides the technical issues related to solar thermal energy, the economic and environmental subjects were of interest for review. So, the topics including solar radiation, potential and feasibility study, flat and evacuated tube collectors, trough and Fresnel collectors, solar Stirling systems, heliostat fields, solar chimney, solar desalination, nanofluid in solar thermal systems, green buildings, passive solar systems, solar biomimetic systems, optimization in solar thermal systems, economic aspects of solar power plants, and solar CHP were announced for this special issue. Here, the published papers are placed in the categories of flat and evacuated tube collectors, trough and Fresnel collectors, solar chimney, green buildings, and photovoltaic thermal systems.

In case of flat collectors, the authors investigated a small-scale solar thermal collector. The absorber was coated with a selective coating, and the study was carried out for a low-pressure environment to increase the performance. Then, a numerical model was developed to predict the performance of the collector plate. In another study, the researchers conducted a detailed modelling of flat plate solar collectors with vacuum glazing, based on the combined external and internal energy balance of the absorber. In this special issue, some authors report the application of phase change materials for a solar chimney, and the storage capability and the night ventilation performance of the system have been assessed. Regarding solar trough collector, a paper is presented for elliptical cavity tube receivers in a parabolic trough solar collector. The authors have designed and optimized the cavity receivers and concluded that the focal distance has a negative relation with the cavity open length, whereas the concentration ratio has a positive relation with the cavity open length. Another paper in this special issue is allocated to a water-cooled PVT (photovoltaic thermal) unit. The authors have demonstrated that the use of maximum power point tracking has a much better function than the fixed optimized.

In the field of energy in buildings and space heating, two papers are reported in this special issue. One is specified for a nearly zero-energy building, which has been done in China as a case study. A solar heating and cooling system including a 35.17 kW cooling absorption chiller, an evacuated tube solar collector, two hot-water storage tanks, two cold-water storage tanks, and a 281 kW cooling tower has been designed and built by the researchers. Another study talks about the effects of ambient conditions on the performance of a direct-expansion solar-assisted heat pump. In this paper, by applying bare plate evaporators for space heating, the effects of ambient temperature, solar irradiation, and relative humidity on the system performance are assessed.

We hope that many researchers from universities, research centers, and industry read the papers of this special issue. Also, it is our pleasure to present this special issue in the field of solar thermal energy; so we hope that the readers find this special issue helpful and effective.

Alibakhsh Kasaeian
Michel Feidt
Stoian Petrescu
Adel Mellit

References

- [1] F. Wang, Z. Cheng, J. Tan, Y. Yuan, Y. Shuai, and L. Liu, "Progress in concentrated solar power technology with parabolic trough collector system: a comprehensive review," *Renewable and Sustainable Energy Reviews*, vol. 79, pp. 1314–1328, 2017.
- [2] W. Herche, "Solar energy strategies in the U.S. utility market," *Renewable and Sustainable Energy Reviews*, vol. 77, pp. 590–595, 2017.
- [3] M. Ghalamchi, A. B. Kasaeian, M. Ghalamchi, and A. Hajiseyed Mirzahosseini, "An experimental study on the thermal performance of a solar chimney with different dimensional parameters," *Renewable Energy*, vol. 91, pp. 477–483, 2016.
- [4] H. Panchal and I. Mohan, "Various methods applied to solar still for enhancement of distillate output," *Desalination*, vol. 415, pp. 76–89, 2017.
- [5] O. Mahian, A. Kianifar, S. A. Kalogirou, I. Pop, and S. Wonwises, "A review of the applications of nanofluids in solar energy," *International Journal of Heat and Mass Transfer*, vol. 57, no. 2, pp. 582–594, 2013.
- [6] Y. Tian and C. Y. Zhao, "A review of solar collectors and thermal energy storage in solar thermal applications," *Applied Energy*, vol. 104, pp. 538–553, 2013.

Research Article

Effects of Ambient Parameters on the Performance of a Direct-Expansion Solar-Assisted Heat Pump with Bare Plate Evaporators for Space Heating

Wenzhu Huang, Jie Ji, Mawufemo Modjinou, and Jing Qin

Department of Thermal Science and Energy Engineering, University of Science and Technology of China, No. 96 Jinzhai Road, Hefei City, Anhui Province, China

Correspondence should be addressed to Jie Ji; jijie@ustc.edu.cn

Received 29 December 2016; Revised 3 June 2017; Accepted 4 July 2017; Published 1 October 2017

Academic Editor: Michel Feidt

Copyright © 2017 Wenzhu Huang et al. This is an open access article distributed under the Creative Commons Attribution License, which permits unrestricted use, distribution, and reproduction in any medium, provided the original work is properly cited.

Research on the direct-expansion solar-assisted heat pump (DX-SAHP) system with bare plate evaporators for space heating is meaningful but insufficient. In this paper, experiments on a DX-SAHP system applying bare plate evaporators for space heating are conducted in the enthalpy difference lab with a solar simulator, with the ambient conditions stable. The independent effects of ambient temperature, solar irradiation, and relative humidity on the system performance are investigated. When ambient temperature changes as 5°C, 10°C, and 15°C, COP increases as 2.12, 2.18, and 2.26. When solar irradiance changes as 0 W m⁻², 100 W m⁻², 200 W m⁻², 300 W m⁻², and 500 W m⁻², COP of the system changes as 2.07, 2.09, 2.14, 2.26, and 2.36. With ambient temperature of 5°C and solar irradiance of 0 W m⁻², when relative humidity is 50%, no frost formed. Whereas with relative humidity of 70% and 90%, frost formed but not seriously frosted after 120 min of operating. Frost did not deteriorate but improved the heating performance of the DX-SAHP system. The change of relative humidity from 70% to 90% improves the evaporating heat exchange rate by 35.0% and increases COP by 16.3%, from 1.78 to 2.07.

1. Introduction

Energy consumed for space heating is a large part of domestic energy consumption. The idea of using solar energy is one of the methods to face the energy crisis, since it is renewable and clean. To introduce solar energy into space heating, solar-assisted heat pump system was proposed. Solar-assisted heat pump systems can effectively utilize solar energy and perform better than conventional heat pumps. Many researches have been published on solar-assisted heat pumps [1–5].

Sporn et al. proposed the idea of direct-expansion solar-assisted heat pump (DX-SAHP), as one type of solar-assisted heat pumps [6]. The components in DX-SAHP systems are reduced compared to that in indirect-expansion solar-assisted heat pumps, because refrigerant absorbs heat directly in the collectors of the system, which work as the evaporator. DX-SAHP is promising due to the advantages of having low cost and nonfreeze-up at nighttime. Lots of researches have been reported on DX-SAHP [7–13].

Chaturvedi and Shen [7] proved that DX-SAHP had better performance compared to traditional heat pump systems, with COP range of 2 to 3. Huang and Chyng [8] built an integral type solar-assisted heat pump water heater with a collector/evaporator and a thermosyphon heat exchanger. The COP of the system was 2.5–3.7 at water temperature between 61°C and 25°C. Krakow and Lin [9] studied the performance of the direct-expansion solar source heat pump systems with solar collectors. They concluded that the system was promising to utilize solar energy in cold climates. Ito et al. [10] analyzed and optimized the structure parameters of a DX-SAHP system in theoretical and experimental methods. Hawlader et al. [11] paid attention to the effect of the volume of water tank on the performance of a DX-SAHP water heater. Chyng et al. [12] theoretically researched the annual performance of an integrated solar-assisted heat pump water heater with a bare collector. Xu et al. [13] simulated the operating performance of a DX-SAHP water heater using the meteorological data in Nanjing. They showed that the system could heat

150 L of water to 55°C efficiently under various weather conditions at different time of the year.

Recently, Li et al. [14] compared two DX-SAHP water heater systems. An optimization method for the collector was concluded. They also suggested that variable frequency compressor and electronic expansion valve should be applied in the system. A DX-SAHP water heater was numerically simulated by Kong et al. [15]. It is concluded that wind speed has no great effect on the system performance. Chow et al. [16] developed a theoretical model of a DX-SAHP water heater with an unglazed solar collector. They simulated the performance of the system in a whole year, obtained a year-long average COP of 6.46 in Hong Kong, and proved the system promising. Sun et al. [17] designed and tested a DX-SAHP water heating system using an optimized-channel roll-bond collector/evaporator. They proved the roll-bond panel with optimized channel pattern could improve the performance of the DX-SAHP system significantly. The performance of a DX-SAHP water heater with integral storage tank with solar irradiance of zero was experimentally investigated [18]. The solar collectors were installed in a climate chamber to work at stable ambient air temperature. Applying the Huang and Lee's performance evaluation method, the characteristic COP for the system is 3.23 under zero solar irradiance conditions at a water-ambient air temperature difference of 15°C. Kuang and Wang [19] tested a DX-SAHP system for domestic use. The system can operate under space heating mode, air conditioning mode, and water heating mode. Space heating was realized by radiant floor heating unit. The experiment data revealed that the system reached COP of 2.6 to 3.3 for space heating and could supply 200 L or 1000 L hot water daily under various weather conditions. Zhang et al. [20] analyzed the effect of R22, R134a, and R744 on the performance of a solar-air hybrid heat source heat pump water heater. They pointed out that three refrigerants had a similar operating performance.

On one hand, the published researches mostly focused on DX-SAHP for water heating instead of space heating. However, the application of DX-SAHP for space heating is also common. But the system performance under this condition has not been researched sufficiently, because the heating capacity is difficult to measure. On the other hand, the most experimental researches on DX-SAHP were tested in outdoor environment. The shortcoming is that the experiments are unrepeatable and unable to present accurate parametric analysis. The experimental study with the system of the four features, as direct-expansion, solar-assisted, space heating, and steady environment is rare. In this paper, a DX-SAHP system for space heating is experimentally studied under stable conditions. During the experiments, the ambient temperature, solar irradiation, and relative humidity were controlled to be constant in the enthalpy difference lab with a solar simulator. Previous investigation [21] showed that DX-SAHP with bare plate evaporators was applicable under frosting conditions but the performance of the system was not sufficiently investigated. Bare plate evaporators also have the advantages of low cost and simple structure. Therefore, bare plate evaporators are selected for the tested system. Based on the experimental data, parametric analysis is conducted,

including ambient temperature, solar irradiation, and relative humidity. The data can be referenced for further experimental and theoretical study of DX-SAHP. The conclusions may benefit the design and optimization of DX-SAHP systems of similar structure.

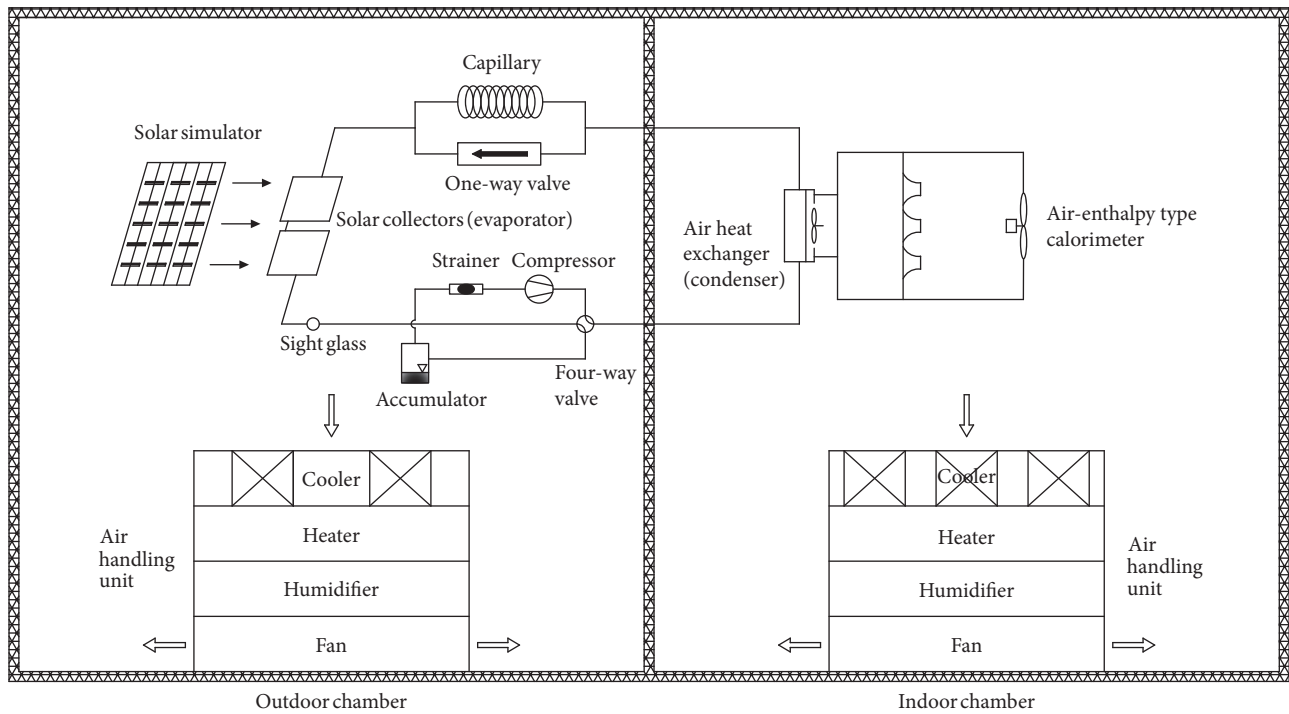
2. Experimental Setup

Using the enthalpy difference lab, which is the standard testing lab for heat pumps, stable test conditions could be realized. The DX-SAHP prototype for space heating is installed in the two chambers of the enthalpy difference lab, as shown in Figure 1(a). The condenser of the DX-SAHP system is the air heat exchanger in the indoor chamber. It is connected directly to the air-enthalpy type calorimeter. Therefore, the heating capacity of the system can be measured and the space heating performance can be analyzed. A rotary-type hermetic compressor with rated input power of 750 W is used, and the refrigerant is R22. In the outdoor chamber, the solar simulator is installed, to generate stable and controllable solar irradiation on the solar collectors, with the instability and heterogeneity under $\pm 5\%$. The spectrum distribution of the solar simulator meets the China National Class B level standard and can simulate solar irradiation in solar thermal research. The luminous area is $2 \times 2 \text{ m}^2$, perfectly covering the collectors.

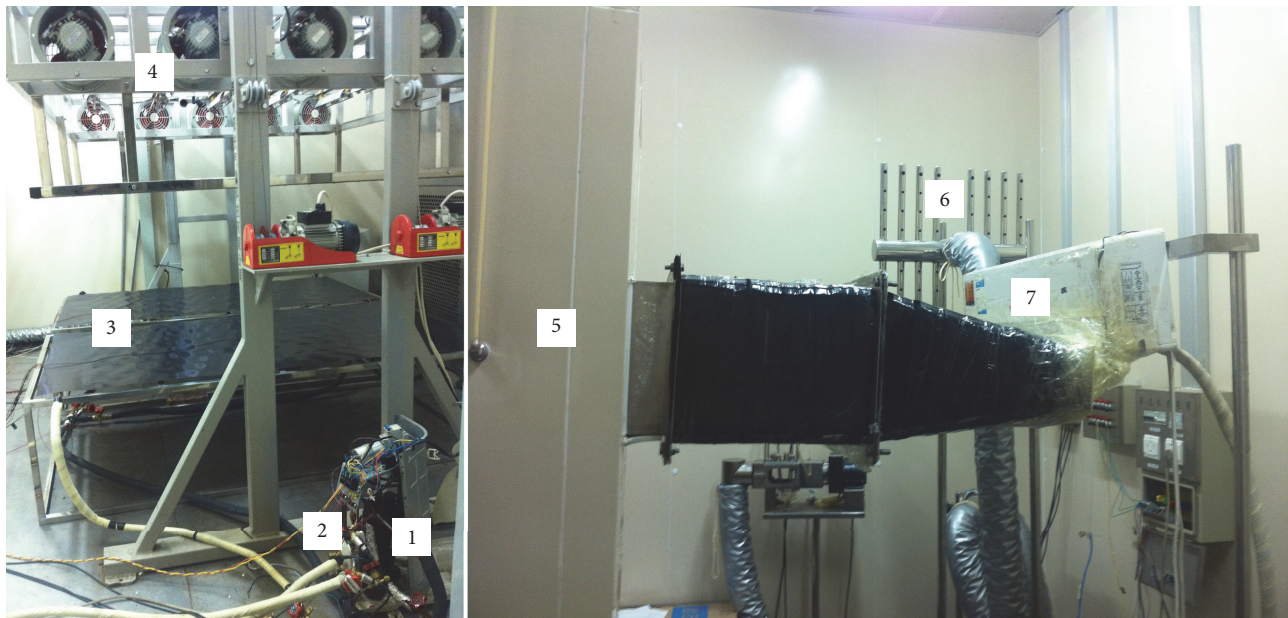
Bare plate evaporators have advantages such as low cost, easy manufactural structure, and slow frosting rate, but DX-SAHP systems with bare plate evaporators are not sufficiently researched. Therefore, two bare flat plate collectors are applied in the experimental prototype of DX-SAHP. The temperature, pressure, solar irradiation, ambient temperature, relative humidity, and heating capacity of the system were measured and recorded. The specifications of the measurement instruments and more detailed experimental settings were presented in our previous work [21].

3. Experimental Procedure and Thermodynamic Analysis Methods

3.1. Experimental Procedure. To research the independent influence of the ambient parameters on the performance of the DX-SAHP system, specific stable conditions were arranged during the experiments, with the help of the enthalpy difference lab with a solar simulator. In the outdoor chamber, the ambient are under winter meteorological conditions. The ambient temperature was chosen as 5°C, 10°C, and 15°C when the relative humidity was maintained as 50% and solar irradiance was 300 W m^{-2} ; solar irradiance was 0 W m^{-2} , 100 W m^{-2} , 200 W m^{-2} , 300 W m^{-2} , and 500 W m^{-2} when the ambient temperature was 15°C and the relative humidity was 50%; the ambient temperature was 5°C and solar irradiance 0 W m^{-2} was when the relative humidity was 50%, 70%, and 90%. When solar irradiance was higher, more thermal load was produced by the solar simulator, and it got harder for the enthalpy difference lab to maintain a constant ambient temperature. Therefore, solar irradiance higher than 500 W m^{-2} was not tested in the experiments. According to GB/T 7725-2004



(a)



(b)

FIGURE 1: (a) A schematic diagram of the enthalpy difference lab and the tested system (b) photo of the DX-SAHP system. (1) Compressor; (2) capillary tube; (3) bare plate evaporators; (4) solar simulator; (5) air-enthalpy type calorimeter; (6) indoor sampling device; (7) indoor air heat exchanger.

(the National Standard of China for air conditioners), the indoor temperature was chosen as 20°C/15°C (dry bulb/wet bulb).

In the experiments, as the first step, the ambient temperature and humidity of the two chambers reached the set values by the operation of the enthalpy difference lab. Then, the solar simulator was activated and generated solar

irradiance, with the values adjustable. The DX-SAHP system was started afterwards and operated for 120 min. The data acquisition system recorded the data at a 6-second interval. Because of the stable conditions, the DX-SAHP system can reach stable operating state and last till the end of the experiments. When the fluctuation of condensing heat exchange rate and energy consumption of the tested

system is under 0.5%, the system is considered as under stable operating state.

3.2. Thermodynamic Analysis Methods. To analyze the thermal performance of the DX-SAHP system, the evaporating heat exchange rate Q_{evap} , the condensing heat exchange rate Q_{cond} , and COP are needed, while the energy consumption is directly measured. For the calculation of the above parameters, the derivations of the mass and energy balance equations are applied as follows.

The mass balance equation is

$$\sum m_{\text{in}} = \sum m_{\text{out}} \quad (1)$$

The energy balance equation is

$$Q + m_{\text{in}}h_{\text{in}} = W + m_{\text{out}}h_{\text{out}}, \quad (2)$$

where Q is the rate of heat input, W is the rate of work output, and h_{in} and h_{out} are the enthalpy of inlet refrigerant and outlet refrigerant.

The compression indicated power can be calculated by [22]

$$W_i = W_{\text{in}}\eta_{\text{comp}}, \quad (3)$$

where η_{comp} is the ratio of the compression indicated power and the compressor input power. η_{comp} can be calculated as

$$\eta_{\text{comp}} = nf\eta_{\text{el}}, \quad (4)$$

where η_{el} is the compression electromechanical efficiency, as 0.78. nf is the correction factor. The manufacturer has given the expression of nf as

$$\begin{aligned} nf = & (0.24105 + 0.02868T_c - 2.77389E - 4T_c^2) \\ & + 1.0E - 4 \times (-61.10691 + 1.7067T_c)T_e \\ & + 1.0E - 4 \times (6.06781 - 0.10841T_c + 0.00124T_c^2)T_e^2, \end{aligned} \quad (5)$$

where T_e is the evaporating temperature and T_c is the condensing temperature. After calculation, the approximate value of η_{comp} is 0.75.

For the DX-SAHP system, the energy balance equation can be written as

$$Q_{\text{evap}} = Q_{\text{cond}} - W_{\text{in}}\eta_{\text{comp}}, \quad (6)$$

where W_{in} is the compressor input power. In the tested system, W_{in} is the energy consumption of the compressor.

According to the air-enthalpy difference method, the condensing heat exchange rate can be calculated by

$$Q_{\text{cond}} = \frac{V_a(h_{\text{in-a}} - h_{\text{out-a}})}{[V_n(1 + D_n)]}. \quad (7)$$

The coefficient of performance COP can present the thermal performance of heat pump systems. COP is expressed as

$$\text{COP} = \frac{Q_{\text{cond}}}{W_{\text{in}} + W_{\text{fan}}}, \quad (8)$$

where W_{fan} is the fan energy consumption in the condenser, as 36 W.

As the mean value of the evaporator inlet and outlet temperatures, the evaporator temperature is written as

$$T_e = \frac{T_{\text{ein}} + T_{\text{eout}}}{2}. \quad (9)$$

According to (9), the evaporator temperature uncertainty equals to the T-type thermocouple uncertainty, with the maximum value of 0.2°C.

The relative error (RE) of COP and the evaporating heat exchange rate can be calculated by

$$\text{RE}_{Q_{\text{evap}}} = \frac{dQ_{\text{evap}}}{Q_{\text{evap}}} = \frac{dQ_{\text{cond}} + \eta dW_{\text{in}}}{Q_{\text{cond}} - \eta W_{\text{in}}}, \quad (10)$$

$$\text{RE}_{\text{COP}} = \frac{d\text{COP}}{\text{COP}} = \left| \frac{1}{Q_{\text{cond}}} \right| dQ_{\text{cond}} + \left| \frac{1}{W_{\text{in}}} \right| dW_{\text{in}}. \quad (11)$$

The experimental RE of COP is 1.3% based on (11).

4. Results and Discussion

As shown in Table 1, the representative tests are selected from which the independent effect of ambient temperature, solar irradiation, and relative humidity on the thermal performance of DX-SAHP can be analyzed. The data in Table 1 are the average value of the parameters during the stable operating state of the DX-SAHP system.

4.1. The Effect of Ambient Temperature. To research the influence of the ambient temperature on the thermal performance of DX-SAHP, the experiment conditions were solar irradiance of 300 W m⁻² and the indoor temperature was 20°C/15°C (DB/WB), while the outdoor temperatures were 5°C, 10°C, and 15°C and the relative humidity was 50%. The results are shown in Figures 2–4.

Under the ambient temperature of 5°C, 10°C, and 15°C and solar irradiance of 300 W m⁻², the evaporator temperature is lower than the ambient temperature, and the specific values are 3.1°C, 7.4°C, and 12.0°C, respectively. The evaporator temperature increases as the ambient temperature increases. Because the evaporator temperature is lower than the ambient temperature, heat transfer occurs from the ambient to the collector. Hence, the heat absorbed by the collector contains ambient heat and solar irradiation heat. It is also observed that the difference between the evaporator temperature and the ambient temperature is 1.9°C, 2.6°C, and 3.0°C corresponding to the ambient temperature of 5°C, 10°C, and 15°C. Therefore, based on the experimental data, it can be concluded that when evaporator temperature is lower than ambient temperature, the difference between the evaporator temperature and the ambient temperature increases with the increase of the ambient temperature. Due to the increase of evaporator temperature, the evaporating pressure also increases as 415.0 kPa, 426.5 kPa, and 473.9 kPa, which in turn, leads to the rise of condensing pressure, with the specific value as 1387.5 kPa, 1533.3 kPa, and 1736.9 kPa.

TABLE 1: Experimental data.

Test number	T_a (°C)	RH (%)	I ($\text{W}\cdot\text{m}^{-2}$)	T_e (°C)	T_c (°C)	P_{evap} (kPa)	P_{cond} (kPa)	W_{in} (W)	Q_{evap} (W)	Q_{cond} (W)	COP
1	5	50	300	3.1	37.4	415.0	1387.5	661	920	1416	2.12
2	10	50	300	7.4	42.1	426.5	1533.3	709	1005	1537	2.18
3	15	50	500	16.8	52.1	590.0	1954.4	877	1415	2073	2.36
4	15	50	300	12.0	46.9	473.9	1736.9	780	1181	1766	2.26
5	15	50	200	11.0	44.2	444.1	1633.7	742	1028	1585	2.14
6	15	50	100	10.0	41.7	404.2	1525.9	707	922	1452	2.09
7	15	50	0	7.6	37.4	392.0	1358.3	632	835	1309	2.07
8	5	50	0	0.0	29.6	282.9	1118.1	559	556	975	1.75
9	5	70	0	0.1	30.2	298.3	1109.9	562	577	998	1.78
10	5	90	0	2.6	30.4	303.5	1120.1	577	779	1191	2.07

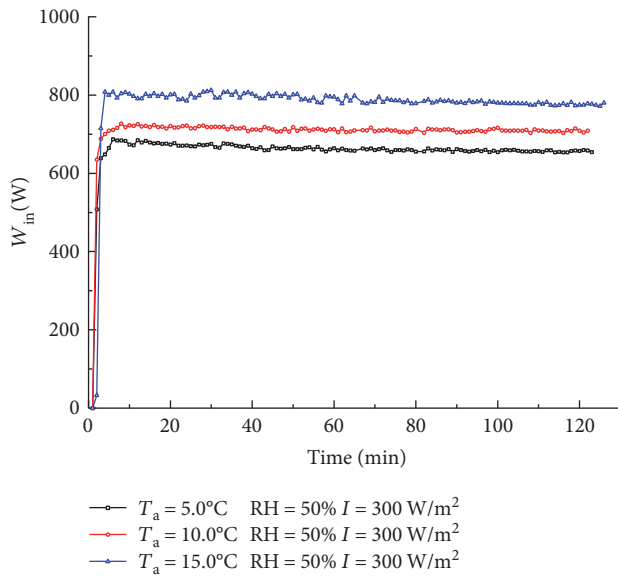


FIGURE 2: Variation of the energy consumption with the ambient temperature of 5°C, 10°C, and 15°C.

Figure 2 shows variation of the energy consumption when the ambient temperature is 5°C, 10°C, and 15°C. It indicates that the energy consumption of DX-SAHP increases with the increase of the ambient temperature. When the evaporator temperature increases, the evaporating pressure, the pressure ratio, and the refrigeration mass flow rate of compressor increase, leading to the rise of the compressor energy consumption. The specific values of the energy consumption are 661 W, 709 W, and 780 W.

Figure 3 shows the condensing and evaporating heat exchange rate under the three experiment conditions. As the ambient temperature increases from 5°C to 15°C, since the indoor temperature is constant and the evaporator temperature is higher, the condensing temperature rises. The condensing heat exchange rate increases by 350 W, and the evaporating heat exchange rate increases by 261 W. The increment of the condensing heat exchange rate is larger than that of the evaporating heat exchange rate because the energy consumption also increases. The evaporating heat exchange rates are 920 W, 1005 W, and 1181 W (with the REs of

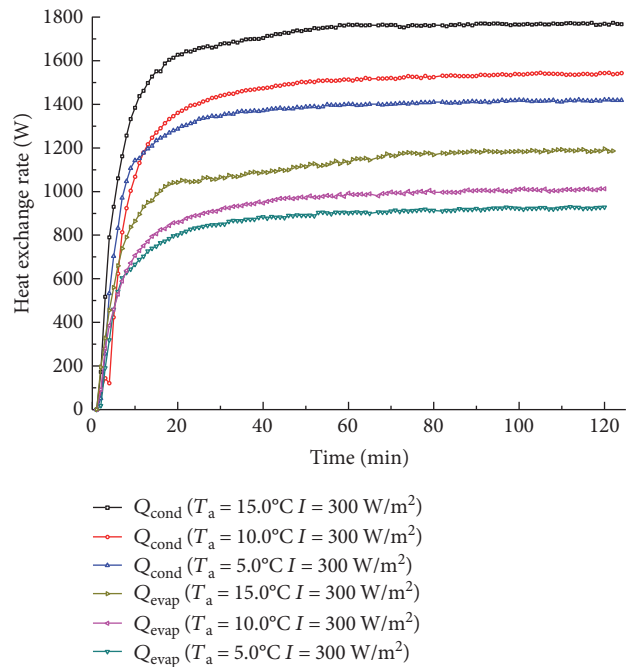


FIGURE 3: Variation of the evaporating and condensing heat exchange rate with the ambient temperature of 5°C, 10°C, and 15°C.

1.9%, 1.9%, and 1.8%) while the condensing heat exchange rates are 1416 W, 1537 W, and 1766 W with the ambient temperature of 5°C, 10°C, and 15°C.

Figure 4 shows the variation of COP when the ambient temperature is 5°C, 10°C, and 15°C. Under the tested conditions, COP is 2.12, 2.18, and 2.26. The increase of COP with the increase of the ambient temperature is not significant. This is because the energy consumption also increases, and to some extent, it thwarts the increase of COP although the condensing heat exchange rate increases.

4.2. The Effect of Solar Irradiation. To research the influence of solar irradiation on the thermal performance of the DX-SAHP system, the following experiment conditions were chosen. The indoor temperature was 20°C/15°C (DB/WB), while the outdoor temperature was 15°C, the relative humidity was 50%, and solar irradiance was 0 W m^{-2} , 100 W m^{-2} ,

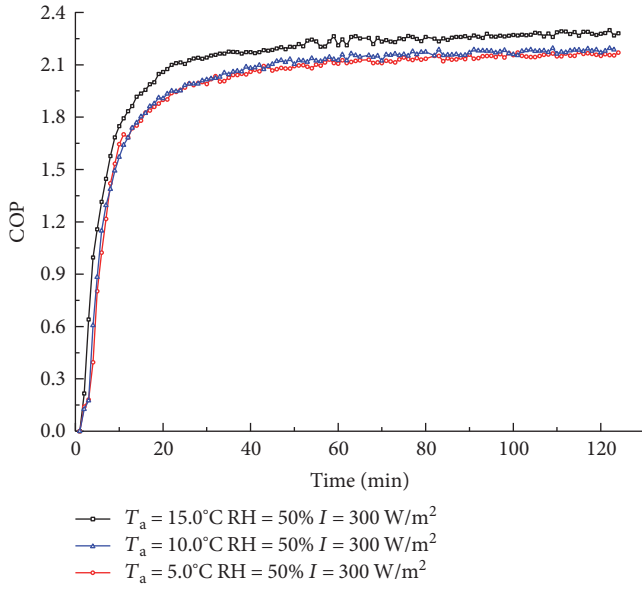


FIGURE 4: Variation of COP with the ambient temperature of 5°C, 10°C, and 15°C.

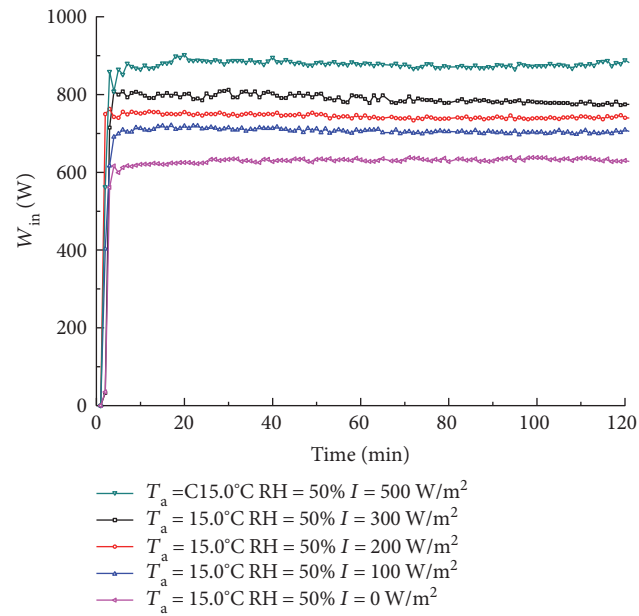


FIGURE 5: Variation of the energy consumption with solar irradiance of 0 W m⁻², 100 W m⁻², 200 W m⁻², 300 W m⁻², and 500 W m⁻².

200 W m⁻², 300 W m⁻², and 500 W m⁻². The results are shown in Figures 5–7.

Under solar irradiance of 0 W m⁻², 100 W m⁻², 200 W m⁻², 300 W m⁻², and 500 W m⁻², the evaporator temperature is 7.6°C, 10.0°C, 11.0°C, 12.0°C, and 16.8°C, respectively. Therefore, the enhancement of solar irradiance can effectively increase the evaporator temperature. Under solar irradiance of 0 W m⁻², 100 W m⁻², 200 W m⁻², and 300 W m⁻² in the tested conditions, the evaporator works at temperature lower

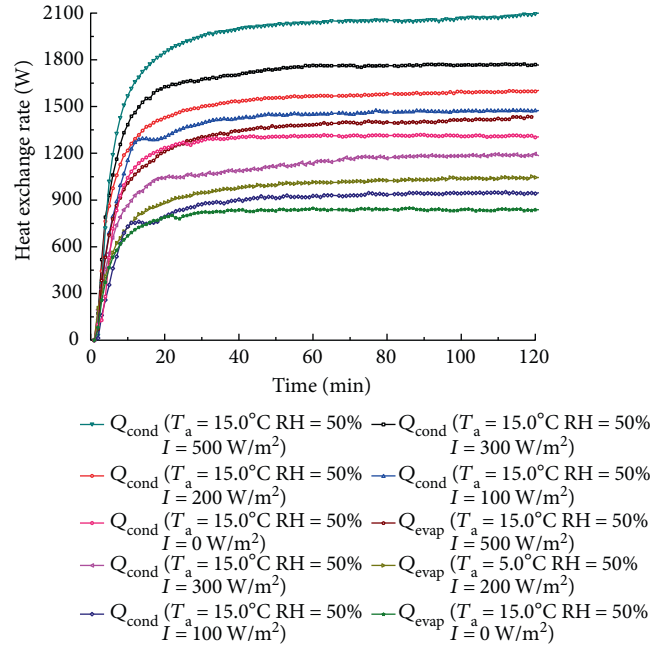


FIGURE 6: Variation of the evaporating and condensing heat exchange rate with solar irradiance of 0 W m⁻², 100 W m⁻², 200 W m⁻², 300 W m⁻², and 500 W m⁻².

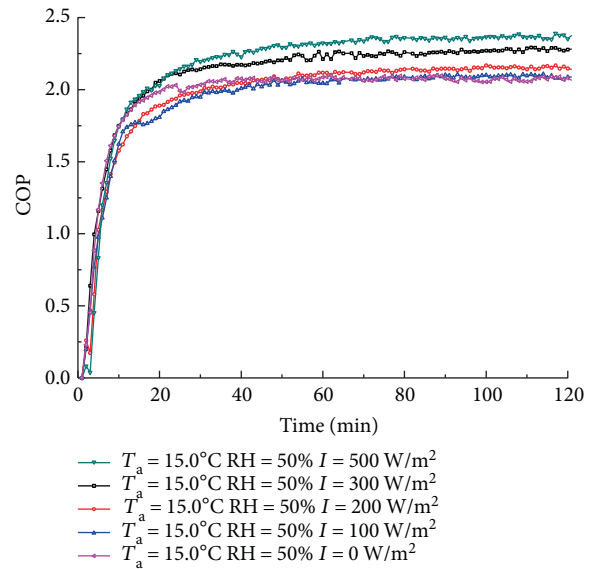


FIGURE 7: Variation of COP with solar irradiance of 0 W m⁻², 100 W m⁻², 200 W m⁻², 300 W m⁻², and 500 W m⁻².

than the ambient temperature. Thus, the evaporator-collector can absorb energy from both solar irradiance and the ambient. While under solar irradiance of 500 W m⁻², the evaporator works at temperature higher than the ambient temperature. A portion of the energy that the evaporator-collector absorbs from solar irradiance is dissipated into the ambient. As the evaporator temperature increases with solar irradiance, the evaporating pressure increases as 392.0 kPa, 404.2 kPa, 444.1 kPa, 473.9 kPa, and 590.0 kPa.

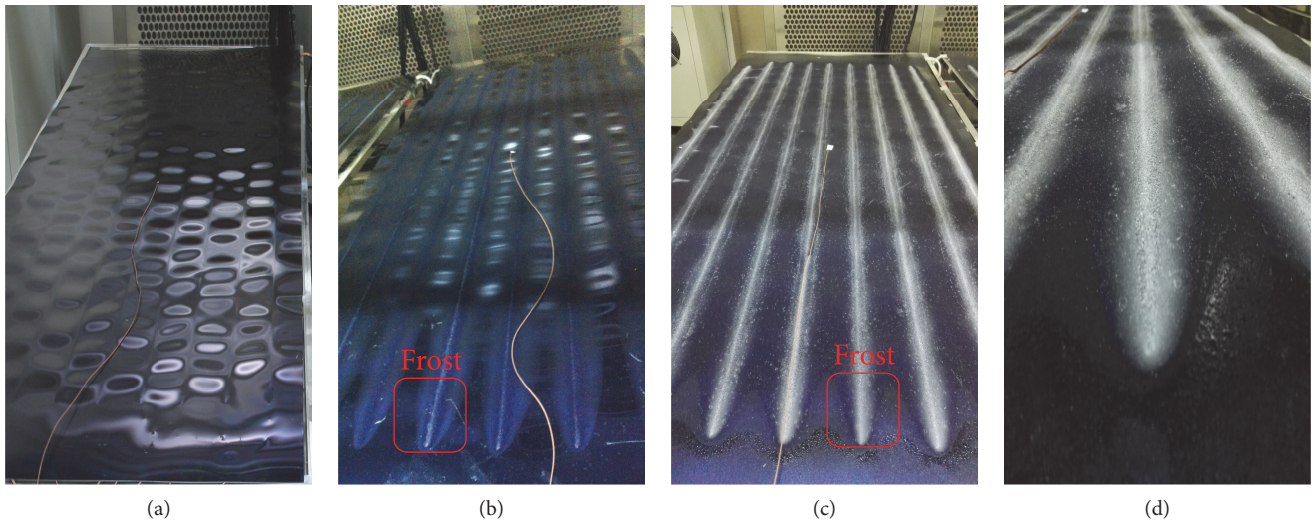


FIGURE 8: Photo of the surface of the collectors after 120 min of operating (a) RH = 50%; (b) RH = 70%; (c) RH = 90%; (d) details of the frost when RH = 90%.

Therefore, the condensing pressure also rises, with the specific values of 1358.3 kPa, 1525.9 kPa, 1633.7 kPa, 1736.9 kPa, and 1954.4 kPa.

Figure 5 shows the variation of the energy consumption with solar irradiance of 0 W m^{-2} , 100 W m^{-2} , 200 W m^{-2} , 300 W m^{-2} , and 500 W m^{-2} . Since the evaporator temperature rises, the evaporating pressure and the refrigerant mass flow rate also rise, which in turn, causes the rise of the system energy consumption. As shown in Figure 6, the energy consumption is 632 W, 707 W, 742 W, 780 W, and 877 W.

The enhancement of solar irradiation can offer more energy to the evaporator-collector. Although higher evaporator temperature could cause part of the gained solar energy dissipated to the ambient, higher evaporator temperature still results in higher evaporating heat exchange rate, which is presented in Figure 6. The specific values are 835 W, 922 W, 1028 W, 1181 W, and 1415 W corresponding to solar irradiance of 0 W m^{-2} , 100 W m^{-2} , 200 W m^{-2} , 300 W m^{-2} , and 500 W m^{-2} (with the REs of 1.9%, 1.9%, 1.9%, 1.8%, and 1.8%). Obviously, the increase of both energy consumption and the evaporating heat exchange rate raises the condensing heat exchange rate. The condensing heat exchange rate changes as 1309 W, 1452 W, 1585 W, 1766 W, and 2073 W. COP of the system also rises with the increase of solar irradiance, with the specific value as 2.07, 2.09, 2.14, 2.26, and 2.36, as shown in Figure 7.

4.3. The Effect of Relative Humidity. To research the influence of the relative humidity on the thermal performance of the DX-SAHP system, the experiment conditions were the indoor temperature of $20^\circ\text{C}/15^\circ\text{C}$ (DB/WB), while the outdoor temperature was 5°C , solar irradiance was 0 W m^{-2} , and the relative humidity was 50%, 70%, and 90%. The results are shown in Figures 8–11.

When the relative humidity was 50%, the surface of the collectors was not frosted after 120 min of operating, as can be observed in Figure 8(a), while when the relative humidity was 70% and 90%, frost occurred during the

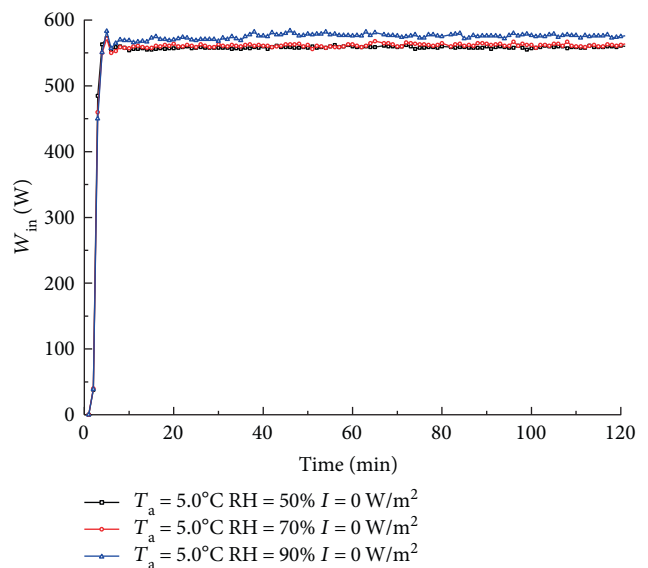


FIGURE 9: Variation of the energy consumption with the relative humidity of 50%, 70%, and 90%.

experiment. The frosting process began after the startup of the system. When the relative humidity was 90%, frost was more serious than that when the relative humidity was 70% after 120 min of operating, as presented in Figures 8(b) and 8(c). The details of the frost are shown in Figure 8(d). The frost is not column shaped, but in the form of ice particles.

Figures 9–11 show the energy consumption, heat exchange rate, and COP when the relative humidity is 50%, 70%, and 90%. Although the collectors are frosted when the relative humidity is 70% and 90%, the heating performance of the system did not decrease significantly, as presented in Figures 9–11. The reason is that the frosting process is slow and the collectors are not seriously frosted

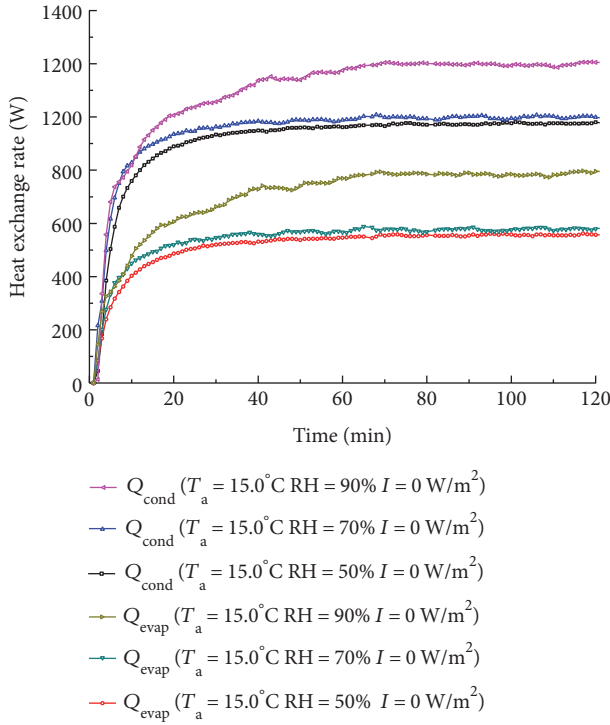


FIGURE 10: Variation of the evaporating and condensing heat exchange rate with the relative humidity of 50%, 70%, and 90%.

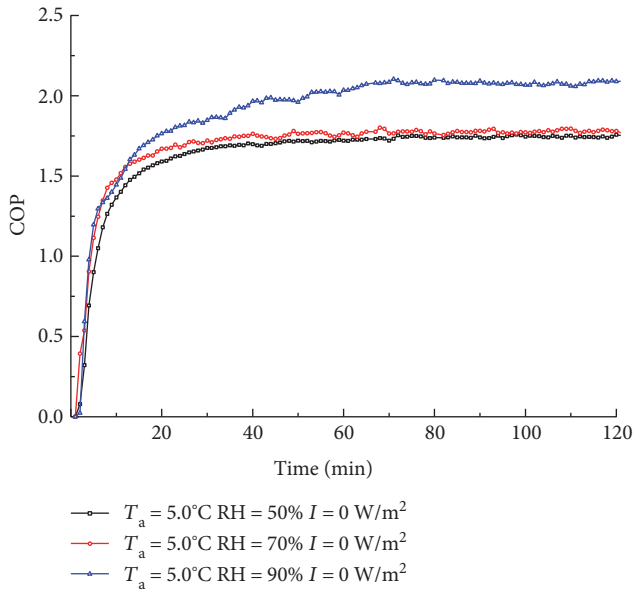


FIGURE 11: Variation of the energy consumption with the relative humidity of 50%, 70%, and 90%.

in 120 min, because the heat exchange area of the collectors is large and the heat exchange mode is natural convection, not forced convection.

The system energy consumption increases with the increase of the relative humidity, which is shown in Figure 9. Because as the relative humidity rises, frost forms on the collectors, and the condensing latent heat raises the

evaporating pressure, leading to the increase of the compressor energy consumption. On the other hand, since the frost is slight, the difference between the values is small, with the values of 559 W, 562 W, and 577 W. As shown in Figure 10, when the relative humidity rises, the evaporating and condensing heat exchange rate increases. The condensing heat exchange rates are 975 W, 998 W, and 1191 W, with the relative humidity of 50%, 70%, and 90%. The evaporating heat exchange rates are 556 W, 577 W, and 779 W (with the REs of 2.2%, 2.1%, and 1.9%). Because the frost formed during the experiments is not thick, thermal resistance between the evaporator and the ambient increases little. Besides, the condensing process brings latent heat which helps the heat exchange between the evaporator and the ambient. Frost deposition increases the roughness of the surface, which is also good for the heat exchange. Consequently, the heat exchange is improved by the frosting process. The differences between the evaporating and condensing heat exchange rates when the relative humidity is 50% and 70% are not significant. When the relative humidity is 50%, no frost occurs. The amount of frost is very little when the relative humidity is of 70%; hence, the system performance is not significantly improved. The same reason can also explain the difference of COP between the two cases, with the values of 1.75 and 1.78 when the relative humidity is 50% and 70%. In comparison, the evaporating heat exchange rate and COP are raised by 35.0% and 16.3% as the relative humidity rising from 70% to 90%, because frost when the relative humidity is 90% is more serious than that when the relative humidity is 70%, as can be observed comparing Figures 8(b) and 8(c).

The phenomenon of the frosting improving the system performance is opposite to the common phenomenon of heat pumps. In the previous work of Guo et al. [23], the frost growth of heat pump systems was divided into three stages. In the first stage, water freezes into a thin ice layer on the evaporator surface, and the granular ices grow gradually to form ice crystals. The performance of the heat pump can be improved. In the second stage, the radius of the ice crystals grows and the performance of the heat pump system is not significantly influenced. In the third stage, the frost thickness grows rapidly, leading to a sharp decrease of the system performance. For common heat pumps, frosting can be fast and serious. The frosting process enters the third stage, and the performance of the system decays rapidly. While for the tested DX-SAHP system, the frosting process is not as serious as common heat pumps due to the flat plate structure of the evaporator. The frost formed during the experiment was not serious, which is in the first stage. Therefore, the frosting process benefits the performance of the DX-SAHP system, as can be seen from the above result analysis.

5. Conclusions

To research the independent influence of ambient temperature, solar irradiation, and relative humidity on the thermal performance of the direct-expansion solar-assisted heat pump (DX-SAHP) system, experiments on a DX-SAHP

system applying bare plate evaporators for space heating are conducted in the enthalpy difference lab with a solar simulator, with the ambient conditions stable. The heating capacity of the DX-SAHP system is measured by an air-enthalpy type calorimeter with high degree of accuracy. The present study tested the DX-SAHP system under winter meteorological conditions, with the ambient temperature of 5°C, 10°C, and 15°C when the relative humidity was 50% and solar irradiance was 300 W m⁻². Solar irradiance was 0 W m⁻², 100 W m⁻², 200 W m⁻², 300 W m⁻², and 500 W m⁻² with the ambient temperature of 15°C and the relative humidity of 50%. The relative humidity was 50%, 70%, and 90% when the ambient temperature was 5°C and solar irradiance was 0 W m⁻².

- (1) When the ambient temperature changes as 5°C, 10°C, and 15°C with solar irradiance of 300 W m⁻² and the relative humidity of 50%, the influence of ambient temperature on the system performance is analyzed. The rise of the ambient temperature leads to higher evaporating pressure and higher evaporator temperature, with the value of 3.1°C, 7.4°C, and 12.0°C. The condensing pressure, energy consumption, the evaporating and condensing heat exchange rate, and COP of the system increase accordingly. The energy consumption is 661 W, 709 W, and 774 W, and the condensing heat exchange rate is 1416 W, 1537 W, and 1766 W. COP increases as 2.12, 2.18, and 2.26, respectively.
- (2) When solar irradiance changes as 0 W m⁻², 100 W m⁻², 200 W m⁻², 300 W m⁻², and 500 W m⁻² with the ambient temperature of 15°C and the relative humidity of 50%, the influence of solar irradiation on the system performance is analyzed. Higher solar irradiation could improve the evaporating pressure and the evaporator temperature, with the values of 7.6°C, 10.0°C, 11.0°C, 12.0°C, and 16.8°C. Therefore, the energy consumption, the condensing and evaporating heat exchange rate, and COP also rise. The energy consumption is 632 W, 707 W, 742 W, 780 W, and 877 W. The condensing heat exchange rate changes as 1309 W, 1452 W, 1585 W, 1766 W, and 2073 W. COP of the system is 2.07, 2.09, 2.14, 2.26, and 2.36.
- (3) When the relative humidity is 50%, 70%, and 90%, the ambient temperature is 5°C, and solar irradiance is 0 W m⁻², the influence of relative humidity is analyzed. With the relative humidity of 50%, no frost occurred on the collectors. While with the relative humidity of 70% and 90%, the collectors were frosted, and under the latter condition, frost is more serious. Results show that frost did not degrade but improved the thermal performance of the DX-SAHP system, because the frost is not serious after 120 min of operating. The increase of the relative humidity from 70% to 90% raises the evaporating heat exchange rate by 35.0% and increases COP by 16.3%, from 1.78 to 2.07.

Nomenclature

Symbols

A_c :	Total collector surface area, m ²
COP:	Coefficient of performance
D_n :	Humidity ratio of air at the nozzle
h :	Enthalpy, J kg ⁻¹ .
I :	Solar irradiance, W m ⁻²
m :	Mass flow rate, kg s ⁻¹
P :	Pressure, kPa
Q :	Rate of heat transfer, W
RH:	Relative humidity, %
t :	Time, min
T :	Temperature, °C
T_a :	Ambient temperature, °C
T_e :	Evaporating temperature, °C
V_a :	Air volume flow rate at the nozzle, m ³ s ⁻¹
V_n :	Specific volume of air at the nozzle, m ³ kg ⁻¹
W :	Energy consumption, W
η :	Efficiency.

Subscripts

cond:	Condenser
evap:	Evaporator
in:	Inlet
in-a:	Air inlet
out-a:	Air outlet
out:	Outlet
comp:	Compressor.

Conflicts of Interest

The authors declare that they have no conflicts of interest.

Acknowledgments

This work is supported by the National Natural Science Foundation of China (no. 51378483), Projects in the National Science & Technology Pillar Program during the Twelfth Five-Year Plan Period (no. 2015BAA02B03), and DongGuan Innovative Research Team Program (no. 2014607101008).

References

- [1] O. Ozgener and A. Hepbasli, "A review on the energy and exergy analysis of solar assisted heat pump systems," *Renewable and Sustainable Energy Reviews*, vol. 11, no. 3, pp. 482–496, 2007.
- [2] K. J. Chua, S. K. Chou, and W. M. Yang, "Advances in heat pump systems: a review," *Applied Energy*, vol. 87, no. 12, pp. 3611–3624, 2010.
- [3] Z. M. Amin and M. N. A. Hawlader, "A review on solar assisted heat pump systems in Singapore," *Renewable and Sustainable Energy Reviews*, vol. 26, pp. 286–293, 2013.
- [4] M. Z. H. Khan, M. R. Al-Mamun, S. Sikdar, P. K. Halder, and M. R. Hasan, "Design, fabrication, and efficiency study of a novel solar thermal water heating system: towards sustainable

- development,” *International Journal of Photoenergy*, vol. 2016, Article ID 9698328, 8 pages, 2016.
- [5] Y. Bai, T. T. Chow, C. Ménézo, and P. Dupeyrat, “Analysis of a hybrid PV/thermal solar-assisted heat pump system for sports center water heating application,” *International Journal of Photoenergy*, vol. 2012, Article ID 265838, 13 pages, 2012.
- [6] P. Sporn and E. R. Ambrose, “The heat pump and solar energy,” in *Proceeding of the World Symposium on Applied Solar Energy*, 1955.
- [7] S. K. Chaturvedi and J. Y. Shen, “Thermal performance of a direct expansion solar-assisted heat-pump,” *Solar Energy*, vol. 33, no. 2, pp. 155–162, 1984.
- [8] B. J. Huang and J. P. Chyng, “Performance characteristics of integral type solar-assisted heat pump,” *Solar Energy*, vol. 71, no. 6, pp. 403–414, 2001.
- [9] K. I. Krakow and S. Lin, “A solar source heat pump with refrigerant-cooled solar collectors for cold climates,” *International Journal of Refrigeration*, vol. 6, no. 1, pp. 20–33, 1983.
- [10] S. Ito, N. Miura, and K. Wang, “Performance of a heat pump using direct expansion solar collectors,” *Solar Energy*, vol. 65, no. 3, pp. 189–196, 1999.
- [11] M. N. A. Hawlader, S. K. Chou, and M. Z. Ullah, “The performance of a solar assisted heat pump water heating system,” *Applied Thermal Engineering*, vol. 21, no. 10, pp. 1049–1065, 2001.
- [12] J. P. Chyng, C. P. Lee, and B. J. Huang, “Performance analysis of a solar-assisted heat pump water heater,” *Solar Energy*, vol. 74, no. 1, pp. 33–44, 2003.
- [13] G. Y. Xu, X. S. Zhang, and S. M. Deng, “A simulation study on the operating performance of a solar-air source heat pump water heater,” *Applied Thermal Engineering*, vol. 26, no. 11–12, pp. 1257–1265, 2006.
- [14] Y. W. Li, R. Z. Wang, J. Y. Wu, and Y. X. Xu, “Experimental performance analysis and optimization of a direct expansion solar-assisted heat pump water heater,” *Energy*, vol. 32, no. 8, pp. 1361–1374, 2007.
- [15] X. Q. Kong, D. Zhang, Y. Li, and Q. M. Yang, “Thermal performance analysis of a direct-expansion solar-assisted heat pump water heater,” *Energy*, vol. 36, no. 12, pp. 6830–6838, 2011.
- [16] T. T. Chow, G. Pei, K. F. Fong, Z. Lin, A. L. S. Chan, and M. He, “Modeling and application of direct-expansion solar-assisted heat pump for water heating in subtropical Hong Kong,” *Applied Energy*, vol. 87, no. 2, pp. 643–649, 2010.
- [17] X. L. Sun, J. Wu, Y. Dai, and R. Wang, “Experimental study on roll-bond collector/evaporator with optimized-channel used in direct expansion solar assisted heat pump water heating system,” *Applied Thermal Engineering*, vol. 66, no. 1–2, pp. 571–579, 2014.
- [18] J. Fernandez-Seara, C. Piñeiro, J. Alberto Dopazo, F. Fernandes, and S. PXB, “Experimental analysis of a direct expansion solar assisted heat pump with integral storage tank for domestic water heating under zero solar radiation conditions,” *Energy Conversion and Management*, vol. 59, pp. 1–8, 2012.
- [19] Y. H. Kuang and R. Z. Wang, “Performance of a multi-functional direct-expansion solar assisted heat pump system,” *Solar Energy*, vol. 80, no. 7, pp. 795–803, 2006.
- [20] D. Zhang, Q. B. Wu, J. P. Li, and X. Q. Kong, “Effects of refrigerant charge and structural parameters on the performance of a direct-expansion solar-assisted heat pump system,” *Applied Thermal Engineering*, vol. 73, no. 1, pp. 522–528, 2014.
- [21] W. Z. Huang, J. Ji, N. Xu, and G. Li, “Frosting characteristics and heating performance of a direct-expansion solar-assisted heat pump for space heating under frosting conditions,” *Applied Energy*, vol. 171, pp. 656–666, 2016.
- [22] Y. W. Li, R. Z. Wang, J. Y. Wu, and Y. X. Xu, “Experimental performance analysis on a direct-expansion solar-assisted heat pump water heater,” *Applied Thermal Engineering*, vol. 27, no. 17–18, pp. 2858–2868, 2007.
- [23] X. M. Guo, Y.-G. Chen, W.-H. Wang, and C.-Z. Chen, “Experimental study on frost growth and dynamic performance of air source heat pump system,” *Applied Thermal Engineering*, vol. 28, no. 17–18, pp. 2267–2278, 2008.

Research Article

Small-Scale Flat Plate Collectors for Solar Thermal Scavenging in Low Conductivity Environments

Emmanuel Ogbonnaya and Leland Weiss

College of Engineering and Science, Louisiana Tech University, P.O. Box 10348, Ruston, LA 71272, USA

Correspondence should be addressed to Leland Weiss; lweiss@latech.edu

Received 10 February 2017; Revised 18 May 2017; Accepted 29 May 2017; Published 3 August 2017

Academic Editor: Michel Feidt

Copyright © 2017 Emmanuel Ogbonnaya and Leland Weiss. This is an open access article distributed under the Creative Commons Attribution License, which permits unrestricted use, distribution, and reproduction in any medium, provided the original work is properly cited.

There is great opportunity to develop power supplies for autonomous application on the small scale. For example, remote environmental sensors may be powered through the harvesting of ambient thermal energy and heating of a thermoelectric generator. This work investigates a small-scale (centimeters) solar thermal collector designed for this application. The absorber is coated with a unique selective coating and then studied in a low pressure environment to increase performance. A numerical model that is used to predict the performance of the collector plate is developed. This is validated based on benchtop testing of a fabricated collector plate in a low-pressure enclosure. Model results indicate that simulated solar input of about 800 W/m^2 results in a collector plate temperature of 298 K in ambient conditions and up to 388 K in vacuum. The model also predicts the various losses in $\text{W/m}^2\text{K}$ from the plate to the surroundings. Plate temperature is validated through the experimental work showing that the model is useful to the future design of these small-scale solar thermal energy collectors.

1. Introduction

There is both need and opportunity to develop small-scale autonomous power supplies that can operate sensors or other devices that require power input for continuous operation. Examples include remote environmental sensors that can monitor water, air, or other critical conditions. Solar thermal power generation for small-scale devices is one means to achieve a low-cost solution that may be deployed to these remote locations.

In these solar thermal systems, maximizing absorption while limiting losses due to convection and radiation is critical in achieving high temperature values. Typically, these systems use a formal collector plate or absorber that is heated by the incoming solar energy. A selective absorber coating is used to enhance absorption and limit reradiation losses. In addition to this plate coating, additional steps that improve collector operation can include transparent thermal insulation. This reduces convection and conduction losses from the heated collector plate, while still allowing incoming solar energy to heat the absorber plate surface. This work examines thermal insulation in solar thermal applications.

In general, there are many types of insulation available on the market. The basic consideration in selecting any particular insulation material is to reduce the flow of heat from one point to the other. Specific parameters such as thermal conductivity, operating temperature, combustibility, chemical stability, mechanical strength and durability, and cost are also considered in the material selection process.

The thermal conductivity of traditional thermal insulation materials like mineral wool, expanded polystyrene (EPS), and extruded polystyrene (XPS) is in the range of 0.033 W/mK to 0.040 W/mK , while polyurethane (PUR) has thermal conductivity ranging from 0.020 W/mK to 0.030 W/mK [1–3]. To achieve very low thermal transmittance, U -value (rate of heat transfer, in watts, across one square meter area divided by the temperature gradient across the surface), high insulation thickness in the range of 40 cm to 50 cm is required [3]. Hence, space and weight constraints limit the application of these materials. More so, these materials are not transparent to solar radiation and therefore do not readily find application in solar thermal collectors.

Another growing insulation material is aerogel. One advantage of this material is its light weight (about 90%

porosity). Further, silica aerogel granulate nanostructured material has been reported to have high solar transmittance and low thermal conductivity and is commercially available with thermal conductivity as low as 0.012 W/mK and thickness in the mm range [4–6]. For a required thermal performance, aerogel exhibits a reduced thickness compared to traditional insulation. Hence, silica aerogel has a promising potential in solar thermal applications. However, the cost of aerogel insulation at this time is still relatively high.

Other techniques being actively explored for flat plate solar thermal applications include vacuum insulation panels [7] and gas-filled panels [8]. In vacuum insulation, the volume between the absorber plate and the cover glass is evacuated thereby limiting convection and conduction losses. The concept of vacuum insulation was invented in 1892 by Sir James Dewar. The Dewar flask consisted of two flasks, one placed within the other and joined at the neck, with the gap between the two flasks partially evacuated of air. Conduction and convection heat transfer is eliminated by the near-vacuum environment. In reality, a perfect vacuum is never achieved. However, low pressure environments positively influence gas conductivity. This technique is also used in glass window panels.

In the absence of sufficient vacuum, there is the possibility to fill the volume above a solar collector plate with a low thermal conductivity gas such as argon (Ar), krypton (Kr), and xenon (Xe). This way the gas-filled panel enhances insulation qualities as gas conductivity is lowered. In both vacuum insulation and gas-filled panel, hermetic sealing is critical. For micro scale applications, there are many established vacuum packaging/encapsulation techniques with airtight seals [9]. This makes the vacuum technique promising in the field of small-scale solar thermal collectors.

This work investigates vacuum insulation technology with a small-scale flat plate solar thermal collector to reduce energy losses from the plate to a minimum. Specifically the effect of low pressure on the thermal performance of the collector plate is modeled and then validated through experimental effort. In final form, the assembled solar collector will capture incoming solar energy and provide power for autonomous sensors or other systems that may be sustainably operated. Figure 1 shows the final assembled system that includes the evacuated space that is the primary focus of this paper. The collector assembly also includes a “selective” thermal collector plate that allows capture of solar energy while limiting losses from the heated plate in the infrared region.

2. Materials and Methods

This section describes numerical and experimental investigations conducted to thermally characterize the performance of solar collector plates in low thermal conductive environments. First, the numerical methods that provide insight and expectations for the operation of these plates in a low pressure environment are presented. Second, the fabrication of the plates is reviewed.

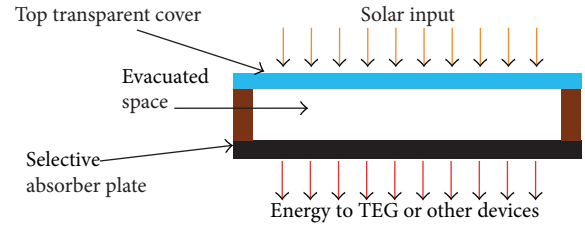


FIGURE 1: Solar collector system for environmental energy scavenging.

2.1. Numerical Methods. This section reviews the approach and methods employed to produce a numerical model of the small-scale STC (solar thermal collector) within a low conductivity space. This begins with an overview of temperature in evacuated spaces and proceeds to describe the equations required to model an overall heat transfer coefficient associated with these environments. These equations formed the foundation for numerical results in this present work.

2.1.1. Temperature Variation in Evacuated Spaces. In an enclosed volume, such as flat plate collectors, the pressure (density) of the gas between the plate and cover glass (top transparent cover, Figure 1) may be sufficiently lowered so that free-convection flow velocities are very small. This way, the only form of heat transfer between the gas molecules is by conduction. The kinetic theory of gases describes a gas as molecules in continuous random motion, colliding with one another and with the walls of the container. The collisions result in exchange of energy and momentum. That is, when a molecule moves from a high-temperature region to a lower-temperature region, it carries with it kinetic energy to the lower-temperature region. The kinetic energy is exchanged with the lower energy molecules through collision. The average distance a molecule travels between collisions is described by the mean free path λ , and can be calculated using [10]

$$\lambda = \frac{1}{n\sqrt{2}\pi d^2}, \quad (1)$$

where n is the gas number density and d is the average diameter (in meters) of the gas molecules. From kinetic theory of gases, the pressure (in Pascals) and number density of a gas molecule are related as shown in [10]

$$P = nkT, \quad (2)$$

where K is the Boltzmann constant ($1.38 \times 10^{-23} \text{ J K}^{-1}$) and T is the gas temperature in Kelvin (K). Applying (2) into (1), the mean free path can be obtained by

$$\lambda = \frac{KT}{P\sqrt{2}\pi d^2}. \quad (3)$$

The average diameter, d , of air ($3.16 \times 10^{-10} \text{ m}$) is obtained by a weighted average (79:21) of the molecular diameters of nitrogen ($3.2 \times 10^{-10} \text{ m}$) and oxygen ($3.0 \times 10^{-10} \text{ m}$). An approximate mean free path equation for the air molecules is therefore given by (4) and (5). When

TABLE 1: Flow regimes versus Knudsen number.

Knudsen number	Pressure (Torr)	Flow regime
$\text{Kn} < 0.001$	$P > 9$	Continuum flow
$0.001 < \text{Kn} < 0.1$	$0.09 < P < 9$	Slip flow
$0.1 < \text{Kn} < 10$	$0.0009 < P < 0.09$	Transitional flow
$10 < \text{Kn}$	$P < 0.0009$	Molecular flow

gases other than air are utilized, the diameter of the gas molecule is used accordingly to determine the mean free path. In all cases, however, the mean free path increases (and hence energy transfer is reduced) as the pressure is lowered, assuming steady-state temperature conditions.

$$\lambda(m) = 3.11 \times 10^{-5} \frac{T}{P_{\text{Pa}}}, \quad (4)$$

$$\lambda(m) = 2.33 \times 10^{-7} \frac{T}{P_{\text{Torr}}}. \quad (5)$$

With an increase in λ , resulting from lowering the pressure of the system, the average distance required for energy exchange between the high-temperature and lower-temperature regions increases. In a flat plate collector, when λ is large, the hot collector plate and the gas molecules in contact or in the immediate neighborhood of the plate will have different temperature values. In this case, the temperature distribution is governed by the molecular activities.

Heat transfer by molecular flow is different from boundary layer (continuum flow) regime where the temperature of the hot plate and the gas in contact with it is assumed to have same temperature values. In the continuum regime, the pressure is near atmospheric and so the mean free path is very small. Hence, heat energy is more easily transferred by collision of molecules. The Nusselt number is usually used in correlating heat transfer in the boundary layer regime [11, 12].

A transition regime exists in which heat transfer is not exactly governed by molecular flow nor by continuum flow. This intermediate regime is further classified into slip and transition regimes [13, 14]. Knudsen number (Kn), a ratio of the mean free path of the gas molecules to the characteristic length L of the device, describes the various regimes. Kn is calculated using (6) [15]. The characteristic length of the collector plate L is defined here as the ratio of plate area to its perimeter. This and the average temperature T_e of the plate was used to verify the flow regimes and pressure ranges based on the Knudsen number. This is as shown in Table 1.

$$\text{Kn} = \frac{\lambda}{L}. \quad (6)$$

As the pressure is lowered, natural convection within the enclosure is also lowered. The main source of heat transfer therefore becomes conduction (by gas molecules) and radiation. At a sufficiently low pressure (the molecular flow regime), natural convection is completely eliminated. The thermal conductivity of gas varies with temperature and pressure. Kaminski [16] presented a correlation for the

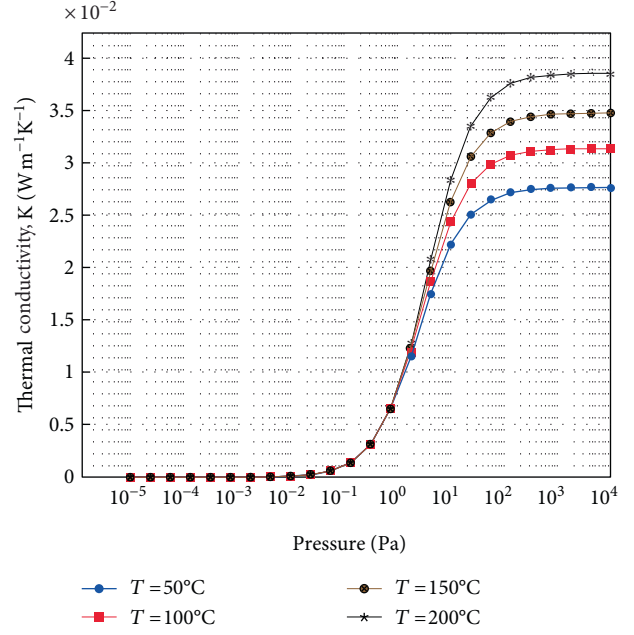


FIGURE 2: Pressure versus thermal conductivity of air at different temperatures.

pressure (Pa) and temperature (K) dependence of thermal conductivity as shown in

$$k_e = \frac{k_o}{1 + 7.657 \times 10^{-5} (T/Pd)}, \quad (7)$$

where k_o and k_e are the thermal conductivity of air at atmospheric and reduced pressure conditions, respectively. d is the distance between the plates.

Overall, k_e decreases with decrease in pressure until the heat conduction is completely eliminated irrespective of operation temperature. The pressure dependence of air thermal conductivity is shown in Figure 2 for different temperatures.

2.1.2. Collector Plate Energy Balance. The useful energy harvested by a solar collector is determined by the ability of the surface to absorb incident radiation as well as the capacity of the body to limit long wavelength radiation from the surface. Further, the convection losses from the collector plate to the ambient air limit the overall useful energy gain. Equation (8) shows the available useful energy \dot{Q}_u harvested by a solar thermal collector plate [17].

$$\dot{Q}_u = q_u A_c = (\tau\alpha) q_s A_c - \bar{U} A_c (\bar{T}_e - T_a) - \epsilon \sigma A_c (\bar{T}_e^4 - T_a^4). \quad (8)$$

Equation (8) notes the overall balance as essentially: [useful energy harvested] = [energy absorbed] – [convection losses] – [radiation losses]. As can be noted, the energy absorbed depends on the transmissivity-absorptivity product ($\tau\alpha$), the area of the collector A_c , and the incident solar radiation intensity q_s . The radiation loss from the surface of the collector plate is directly proportional to the emissivity ϵ of

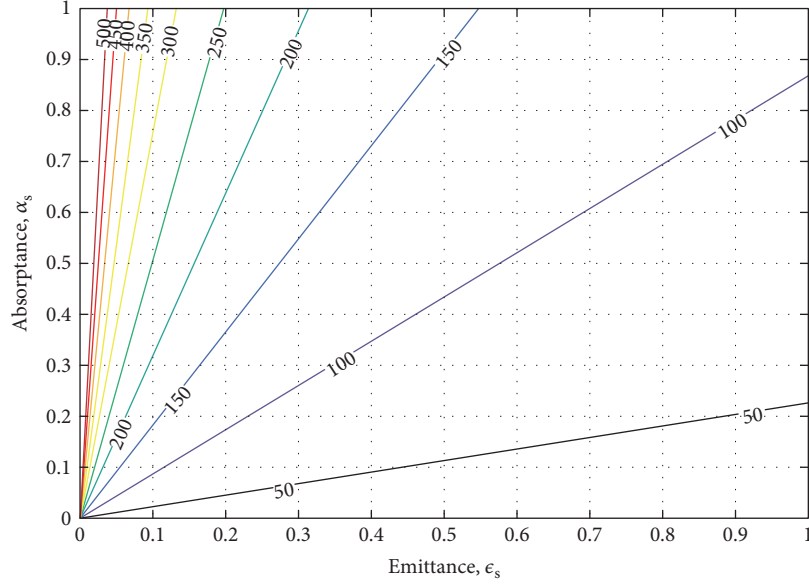


FIGURE 3: Steady-state temperature contour plot of a surface exposed to 750 W/m^2 and ambient temperature T_α of 25°C based on absorptivity and emissivity of the surface.

the surface. Further, since the sides of the collector as well as the top and bottom surfaces are subject to convection and conduction losses, the overall heat transfer coefficient \bar{U} is critical in determining the amount of loss from the plate. These parameters are analyzed as part of this numerical effort as follows.

2.1.3. Steady-State Temperature. The temperature of the absorber element rises as radiation is absorbed. Hence, the temperature varies with time. However, to simplify this analysis, a steady-state (thermal equilibrium) condition is assumed. Hence, this section presents the steady-state temperature conditions for a solar collector element.

At thermal equilibrium, the energy absorbed by the collector is equal to that lost from the surface such that there is no net energy gain as shown in (9). If the cover glass is highly transmissive such that $\tau_g \sim 1$, then the absorbed energy is dependent on the solar absorptivity α_s of the surface while the amount of losses from the collector is related to the emittance ϵ and the heat loss coefficient \bar{U} [17].

$$0 = \alpha_s q_s A_c - \bar{U} A_e (\bar{T}_e - T_a) - \epsilon \sigma A_e (\bar{T}_e^4 - T_a^4), \quad (9)$$

$$\alpha_s q_s A_c = \bar{U} A_e (\bar{T}_e - T_a) + \epsilon \sigma A_e (\bar{T}_e^4 - T_a^4). \quad (10)$$

The ability to achieve high temperature values is critical for a system that relies on thermal energy as input. The goal is, then, to design a system that maximizes temperature gain from the sun's heat energy. Typically, in a flat plate solar collector, there is no optical concentrating device. Hence, the area of the collector A_c is equal to the area of the absorber element of the collector A_e . This reduces (10) to

$$\alpha_s q_s = \bar{U} (\bar{T}_e - T_a) + \epsilon \sigma (\bar{T}_e^4 - T_a^4). \quad (11)$$

2.1.4. Negligible Heat Loss Coefficient. If the collector's overall heat loss coefficient is negligible (i.e., $\bar{U} = 0$) such that there are no convection or conduction losses from the plate, then the stagnation temperature of the collector (from 11) can be rewritten as (12). It has been demonstrated that vacuum packaging at a pressure of 10 mTorr ($\sim 1.3 \text{ Pa}$) or below is sufficient to effectively eliminate conductive and convective heat losses [18]. It should be noted that in a real world setting with a structure formally attached around the collector (Figure 1), additional losses to those supporting structures and sidewalls will increase these losses.

$$\bar{T}_e = \sqrt[4]{T_a^4 + (\alpha_s q_s / \epsilon \sigma)}. \quad (12)$$

Figure 3 shows the achievable temperatures under different α_s and ϵ values. It can be seen that a flat plate collector will achieve a stagnation temperature above 300°C if the infrared emissivity is kept below 0.132 and there are no conduction and convection losses from the plate. Lower values of infrared emissivity will be required depending on the value of the collector absorptivity. A detailed review of absorber coating materials yielding varying absorptivity and emissivity values is given in [19]. Many of these coating materials are commercially available.

In this work, nickel-tin (Ni-Sn) coating has been selected as the collector absorber material. We have previously demonstrated this collector in small-scale application in ambient conditions [20]. This prior work has indicated that black Ni-Sn selective coating has promising potential as a highly effective selective absorber structure with absorptivity α_s of 0.98 and emissivity ϵ of 0.10 [21].

2.1.5. Heat Loss Coefficient Effect. Despite the negligible thermal losses predicted at low pressures, in real world applications, the amount of heat absorbed by the collector is reduced by those losses from the collector. The effect of losses

on the collector plate can be specifically studied through the use of established collector plate models for overall heat loss effects. Results of this study are shown in Figure 4, clearly demonstrating the relationship between heat loss and operating plate temperature. Experimental results correlate well (Section 3.2) and indicate that despite the low pressure conditions of the experimental setup, loss to the surroundings did occur. This was expected given the operating pressure that was above the threshold levels of 10 mTorr (1.3 Pa) [18].

If steady-state condition is assumed, the net useful heat gain absorbed by the collector is zero. Equation (11) is used to evaluate the effect of heat loss coefficient \bar{U} on the steady-state temperature of the absorber element T_e . This assumes known values of incident radiation, solar absorptivity α_s , emissivity ϵ , and ambient temperature T_a .

The overall heat loss coefficient, \bar{U} , is a function of various parameters. These include the temperature of the absorber plate, glass cover, and ambient temperature, emissivity of absorber (ϵ_e) and glass cover (ϵ_g), number of glass cover plates (N), air gap distance, plate tilt angle, β thermal conductivity of insulation material (k) and its thickness (x), and convective heat transfer coefficient (h_a). \bar{U} from the absorber surface to the ambient is the sum of the top loss coefficient \bar{U}_{top} , edge loss coefficient \bar{U}_{edge} , and the back-loss coefficient \bar{U}_{back} , as shown in.

$$\bar{U} = \bar{U}_{top} + \bar{U}_{edge} + \bar{U}_{back}. \quad (13)$$

An equation for \bar{U}_{top} , developed by Klein [22] and modified by Duffie and Beckman [23], is presented in (equation 14). This is used to approximate the thermal loss coefficient to the ambient environment. The ambient wind loss coefficient h_a and the temperature gradient between the glass cover and the ambient influence the top loss heat transfer coefficient.

$$\bar{U}_{top} = \left[\frac{N}{C/T_e[(T_e - T_a)/(N + f)]^e + h_a} \right]^{-1} + \left[\frac{\sigma(T_e + T_a)(T_e^2 + T_a^2)}{(\epsilon_e + .00591Nh_a)^{-1} + (2N + f - 1 + .13 \epsilon_e/\epsilon_g) - N} \right], \quad (14)$$

where

$$\begin{aligned} C &= 520(1 - .000051\beta^2), \\ f &= (1 + .089h_a - .1166h_a\epsilon_e)(1 + .07866N), \\ e &= .43 \left(1 - \frac{100}{T_e} \right). \end{aligned} \quad (15)$$

Further, the back-loss and edge-loss coefficients can be solved using (16) and (17) [24].

$$\bar{U}_{back} = \frac{k_b}{x_b}, \quad (16)$$

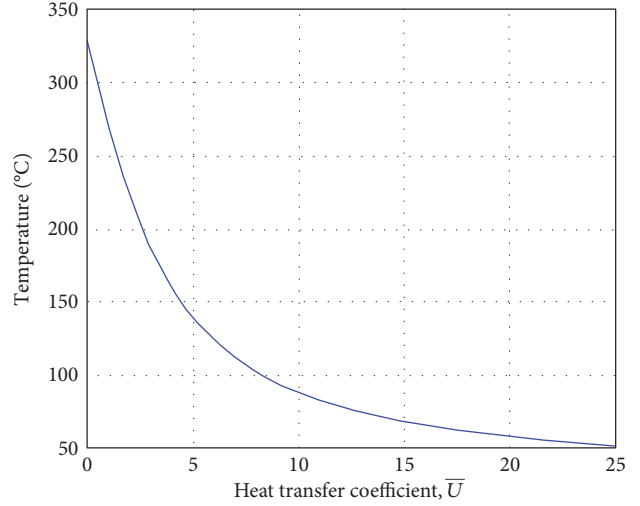


FIGURE 4: Effect of overall heat transfer coefficient \bar{U} on the steady-state temperature of a surface exposed to 750 W/m^2 and ambient temperature T_a of 25°C , based on absorptivity of 0.91 and emissivity of 0.1.

$$\bar{U}_{edge} = \frac{k_e}{x_e} \left[\frac{(L + W)H}{LW} \right]. \quad (17)$$

$L \times W$ is the area of the absorber, and H is the height of the collector casing. Buchberg et al. [25] have suggested the following correlation (18) for solving the natural convection heat transfer coefficient in the enclosed space between the absorber plate and glass cover.

$$h = \frac{\text{Nu} \cdot k}{L}, \quad (18)$$

where Nu is the Nusselt number, k is the thermal conductivity of air, and L is the air gap. Nu may be calculated using [26].

$$\begin{aligned} \text{Nu} &= 1 + 1.44 \left[1 - \frac{1708}{\cos\beta \cdot \text{Ra}} \right] \left[1 - \frac{\sin(1.8\beta)^{1.6} \cdot 1708}{\cos\beta \cdot \text{Ra}} \right] \\ &+ \left[\left(\frac{\cos\beta \cdot \text{Ra}}{5830} \right)^{1/3} - 1 \right]. \end{aligned} \quad (19)$$

Ra is the Rayleigh number (a product of the Grashof and Prandtl numbers) given by

$$\text{Ra} = \text{Gr} \times \text{Pr} = \frac{g\beta(\Delta T)d^3}{\nu^2} \times \text{Pr}. \quad (20)$$

2.2. Fabrication. The fabrication and testing of a solar selective absorber coating in atmospheric pressure conditions have been reported in prior published work. Fabrication of the collector plates that were tested as part of this effort is also reviewed and has been published in prior work [20]. A brief overview of the fabrication of these plates is included in this section.

Fabrication of the solar thermal collector plates began with selection of a copper plate to serve as the substrate. $200 \mu\text{m}$ thick copper sheeting was selected for this work. To

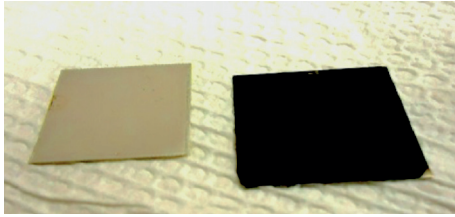


FIGURE 5: Copper solar collector plate with intermediate 10 μm Ni layer (left) and final nickel-tin selective coating (right).

this base, a “selective” absorber coating was applied. Selective coatings have been shown to effectively maximize absorption of incident solar radiation while limiting loss in the infrared region [23]. The coating was applied through an electrodeposition process in two steps. First, a nickel base undercoating layer was applied to a thickness of about $10\ \mu\text{m}$. To this intermediate layer, the final selective absorber coating was applied.

Thickness of the black selective absorber coating was applied based on literature indicating effective thicknesses in the range of 100 to 200 nm [27]. The coating was a bimetallic nickel-tin that was electrodeposited at room temperature in a neutral pH electroplating bath. Current densities and other specific electroplating bath parameters are included in the prior published efforts [21]. An example of the completed collector plate is shown in Figure 5, ready for use in these new low-vacuum condition tests.

2.3. Test Setup and Procedure. This section describes tests conducted to thermally characterize the performance of collector plates in low thermally conductive environments. Two tests were conducted. The first was conducted under atmospheric conditions similar to previously reported tests [20]. These formed the baseline data for this present work. The second test was conducted under an evacuated environmental condition. Lower pressure conditions as noted previously limit heat losses. Hence, the effect of pressure variation on temperature was experimentally studied using the fabricated small-scale STC. Both tests were conducted with the collector plate setup in an enclosed chamber. This further helped to limit and purposefully control convection losses from the ambient.

A halogen lamp was used to simulate solar radiation in this experiment. The simulator lamp used was a Sun System R SS-2 MH 400 W lamp. All tests were conducted by exposing the collector plate to incident radiation from the lamp. Like the sun, the intensity of the radiation from the lamp varied with distance. As the distance from the lamp increased, the intensity of output decreased. A Hukseflux SR11 pyranometer was used to validate the intensity of the radiation at various distances from the simulator lamp. This information was used to select an appropriate distance from the lamp which simulated flux density closely approximating real world availability. A Z-axis laboratory jack was used in adjusting the height of the test setup from the lamp.

An intensity of approximately $796\ \text{W}/\text{m}^2$ was selected. The pyranometer was used to determine the required

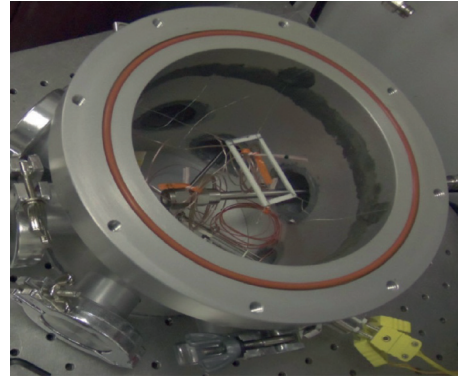


FIGURE 6: Vacuum chamber with suspended fiberglass frame for collector plate mounting.

distance from the simulator lamp. The experiment was placed in a vacuum chamber to minimize heat losses during experimentation. The vacuum chamber was cast and designed specifically for these tests of small-scale collectors. A highly transmissive glass window provided top cover to the chamber. The transmissivity of the chamber glass cover was verified by passing the simulated solar radiation through the lid and measuring its flux density via Pyranometer. The result showed that the glass had a transmissivity of 0.98. This amounted to a radiation intensity of approximately $780\ \text{W}/\text{m}^2$ reaching sample surfaces inside the chamber. Other features of the chamber included different CF style bulkhead fittings that allowed pass-through of wires as needed to fully operate and characterize the collector plates in the altered environment.

A fiberglass material (Garolite G-7 from McMaster-Carr) was used as a frame to support the collector plate at the center of the chamber. The frame was suspended as shown in Figure 6 using 36 SWG (standard wire gauge) nichrome wires. Garolite G-7 was selected due to its very low thermal conductivity (on the order of $0.3\ \text{W}/\text{mK}$) and high mechanical strength. The low thermal conductivity further limited unintended thermal conduction from the collector during operation while the mechanical strength ensured stable support for the collector plate. The nichrome wires were epoxied to the chamber wall. This created a suspended base for the collectors. Each collector was placed on the fiberglass base such that the collectors did not extend to the nichrome wires. This way, heat loss through conduction from the collector plate was only via low conductive fiberglass.

The temperature of the collector plate and chamber environment when exposed to incident radiation were monitored using thermocouples (TCs) (SA1-k-120 from Omega Engineering). The first TC was placed on the back side of the collector plate. This monitored the plate temperature during operation. The second TC was suspended within the chamber to directly monitor the temperature within the chamber. A thermocouple feedthrough (TFT3KY00008B from Lesker, USA) was used to fit the TCs through the vacuum chamber wall. This was useful in maintaining the isolated environment. National Instruments LabVIEW (using a cDAQ-9174 data logger) was used to record all TC data to a computer



FIGURE 7: Top-down view of collector plate (STC) mounted in a vacuum chamber ready for testing.

for analysis. Figure 7 shows the vacuum chamber setup with mounted collector plate ready for testing.

With collector plate mounted within the vacuum chamber and TCs connected, a vacuum pump was connected with pressure sensor to vary the working condition of the collector environment. This readied the plates for testing.

3. Results and Discussion

3.1. Numerical Results. First, results from the numerical analysis are presented. Figure 4 shows the relationship between average heat loss coefficient, \bar{U} , and T_e . Actual absorptivity α_s determined from prior published work was used for this analysis [20]. Hence, this plot utilizes incident radiation of 750 W/m^2 , absorptivity of 0.91, and emissivity of 0.1.

It can be seen from Figure 4 that as the heat loss coefficient increases, there is a significant decrease in the absorber plate temperature. Hence, adequate thermal insulation must be utilized to limit heat losses from the plate. Further, the overall heat loss coefficient and other parameters were estimated based on the formulations of Section 2.1. The range of variables as determined are listed in Table 2. The values obtained were compared to results of experimental tests discussed in the next section. Of note were the predicted temperatures of the plate which were directly validated through the ensuing experimental effort.

3.2. Experimental Results. This section presents results of experimental tests conducted to validate the numerical analysis. Temperature of the collector plates was monitored when exposed to radiation flux as described in Section 2.3. Two tests were conducted. The first recorded the temperature of the plate under atmospheric conditions while the second test was conducted under an evacuated volume. In both cases, the temperature of the plates and the vacuum chamber were monitored until steady-state conditions were achieved.

Figure 8 shows the collector temperature plot for both atmospheric and partial vacuum test conditions. The temperature profile showed that the plate had a stagnation temperature of 96°C under atmospheric conditions. Following the atmospheric condition tests, the collector plate was also tested to characterize the effect of low pressure conditions on the thermal performance of the plate. The pressure of

TABLE 2: Small-scale solar collector specification variables.

Variable	Range
Ambient temperature, T_a	298 K
Absorber plate temperature, T_e	363–388 K
Absorber plate emittance, ϵ_e	0.1
Glass cover emittance, ϵ_g	0.90
Collector tilt angle, β	0°
Collector length, L	0.04 m
Collector width, W	0.04 m
Number of cover, N	1
Insulation material	Vacuum
Wind heat transfer coefficient, h_a	1–10 $\text{W/m}^2 \text{K}$
Top loss coefficient, \bar{U}_{top}	1.68–4.40 $\text{W/m}^2 \text{K}$
Total loss coefficient, \bar{U}	3.10–7.86 $\text{W/m}^2 \text{K}$

the chamber was lowered to 715 mTorr, or 95.3 Pa, (from atmospheric) and held constant at this point throughout each test. The results showed an increased slope of the temperature profile. The stagnation temperature of the plate was 115°C , representing an increase of about 16%. The chamber interior temperature was also monitored in each test. In both cases, the chamber temperature stagnated at about 58°C . This is much lower than the temperature of the plate for each test confirming that the plates were heated directly by thermal radiation and not by greenhouse effect within the chamber.

To further confirm that temperature gain recorded under partial vacuum conditions was primarily due to space evacuation, air molecules were reintroduced into the chamber after steady-state conditions were reached. The vacuum release points are as shown in Figure 8. As the chamber pressure increased, the temperature of the plate declined. As the chamber pressure increased back to atmospheric conditions, the temperature of the collector again matched the temperature obtained previously under atmospheric condition testing. Similar result was also noted for the chamber temperature. The reduction in collector temperature was caused by energy losses occasioned by the presence of air molecules within the chamber. These results agreed with numerical results which predicted an increase in collector temperature that closely agreed with experiment (Table 2). This allows the developed model to be used for design and prediction of different collector plates of different size and scale that will be well suited to a variety of applications or installations.

4. Conclusions

Small-scale energy scavenging through solar thermal application has great potential to provide power to a variety of sensors or other remote devices that may be fully autonomous in their operation. In this effort, a small-scale solar thermal collector (STC) is fabricated and tested in a simulated low vacuum environment. In parallel, a numerical model is developed that can be utilized to design and predict operation of STCs of varying sizes and operating environments.

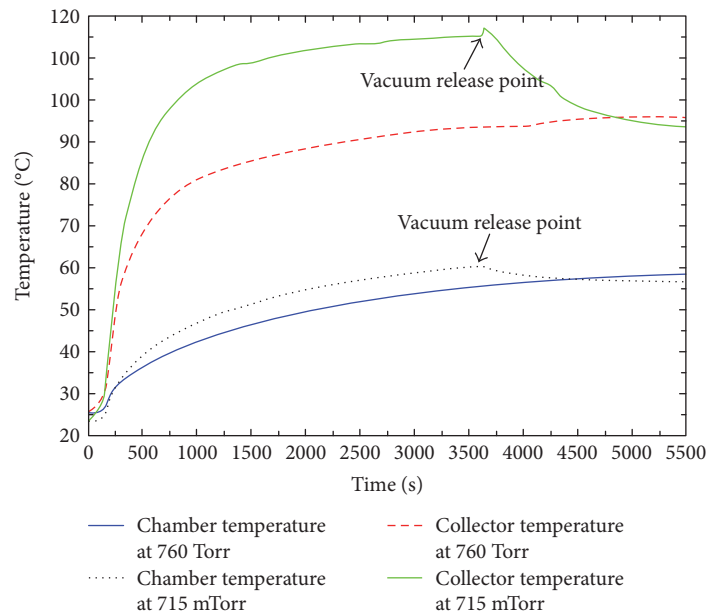


FIGURE 8: Collector plate operating temperature at different atmospheric pressures.

The STC itself was fabricated using a copper substrate and tin-nickel coating to form a selective surface. Tests were conducted to verify the operation temperature of collector plates when exposed to simulated solar radiation. Results showed an improvement in the stagnation temperature of the collector plate when operated in a partial vacuum environment (715 mTorr, 95.3 Pa) compared to results obtained under atmospheric pressure. Total increase was about 16% for a collector plate with surface area of 40 by 40 mm. The model proved a useful tool for future development efforts based on comparison to the experimental results.

Continuing and future work will examine the temperature of the plate under higher vacuum conditions. Effort is also underway to examine the effect of other operation environments with low thermal conductivity gases like argon, xenon and krypton. This way, rather than maintaining a vacuum environment, other gases (with thermal conductivity lower than air) may be utilized to replace air molecules within the operation environment.

Conflicts of Interest

The authors declare that they have no conflicts of interest.

Acknowledgments

The authors gratefully acknowledge the support of this work by the NSF via Grant no. ECCS-1053729.

References

- [1] M. Alghoul, M. Sulaiman, B. Azmi, and M. A. Wahab, "Review of materials for solar thermal collectors," *Anti-Corrosion Methods and Materials*, vol. 52, no. 4, pp. 199–206, 2005.
- [2] A. M. Papadopoulos, "State of the art in thermal insulation materials and aims for future developments," *Energy and Buildings*, vol. 37, no. 1, pp. 77–86, 2005.
- [3] B. P. Jelle, A. Gustavsen, and R. Baetens, "The high performance thermal building insulation materials and solutions of tomorrow," in *Proceedings of the Thermal Performance of the Exterior Envelopes of Whole Buildings XI International Conference (Buildings XI)*, pp. 5–9, Clearwater Beach, Florida, USA, 2010.
- [4] M. Reim, W. Korner, J. Manara et al., "Silica aerogel granulate material for thermal insulation and daylighting," *Solar Energy*, vol. 79, no. 2, pp. 131–139, 2005.
- [5] A. Aergogels, "Spaceloft 3251, 6251, 9251: flexible insulation for industrial, commercial and residential applications," 2007, <http://www.airtightdistribution.com/>.
- [6] A. Aergogels, *Spaceloft 6250, Extreme Protection for Extreme Environments*, 2007.
- [7] R. Baetens, B. P. Jelle, J. V. Thue et al., "Vacuum insulation panels for building applications: a review and beyond," *Energy and Buildings*, vol. 42, no. 2, pp. 147–172, 2010.
- [8] J. Vestlund, M. Ronnelid, and J.-O. Dalenback, "Thermal performance of gas-filled flat plate solar collectors," *Solar Energy*, vol. 83, no. 6, pp. 896–904, 2009.
- [9] J. H. Lau, C. Lee, C. Premachandran, and A. Yu, *Advanced MEMS Packaging*, Citeseer, McGraw-Hill, New York, 2010.
- [10] A. Chambers, R. K. Fitch, and B. S. Halliday, *Basic Vacuum Technology*, Institute of Physics Publishing, London, 1998.
- [11] C. Y. Warner and V. S. Arpaci, "An experimental investigation of turbulent natural convection in air at low pressure along a vertical heated flat plate," *International Journal of Heat and Mass Transfer*, vol. 11, no. 3, pp. 397–406, 1968.
- [12] S. W. Churchill and H. H. Chu, "Correlating equations for laminar and turbulent free convection from a vertical plate," *International Journal of Heat and Mass Transfer*, vol. 18, no. 11, pp. 1323–1329, 1975.
- [13] X. Chen and E. Pfender, "Effect of the Knudsen number on heat transfer to a particle immersed into a thermal

- plasma," *Plasma Chemistry and Plasma Processing*, vol. 3, no. 1, pp. 97–113, 1983.
- [14] S. Kakac, H. Liu, and A. Pramuanjaroenkij, *Heat Exchangers: Selection, Rating, and Thermal Design*, CRC press, New York, 2012.
- [15] J. P. Holman, *Heat Transfer*, McGraw Hill, Inc, New York, 8th edition, 1997.
- [16] D. A. Kaminski, *Fluid Flow Data Book*, General Electric Company, Boston, 1980.
- [17] J. R. Howell, R. B. Bannerot, and G. C. Vliet, *Solar-Thermal Energy Systems: Analysis and Design*, Mcgraw-Hill College, New York, 1982.
- [18] L. R. Arana, S. B. Schaevitz, A. J. Franz, M. A. Schmidt, and K. F. Jensen, "A microfabricated suspended-tube chemical reactor for thermally efficient fuel processing," *Journal of Microelectromechanical Systems*, vol. 12, no. 5, pp. 600–612, 2003.
- [19] C. E. Kennedy, *Review of Mid- to High-Temperature Solar Selective Absorber Materials*, vol. 1617, National Renewable Energy Laboratory Golden, Colo, USA, 2002.
- [20] E. Ogbonnaya, A. Gunasekaran, and L. Weiss, "Micro solar energy harvesting using thin film selective absorber coating and thermoelectric generators," *Microsystem Technologiess*, vol. 19, no. 7, pp. 995–1004, 2013.
- [21] R. Kirilov, P. Stefchev, Z. Alexieva, and H. Dikov, "A high effective selective absorbing coating for solar thermal collectors," *Solid State Phenomena*, vol. 159, pp. 97–100, 2010.
- [22] S. Klein, "Calculation of flat-plate collector loss coefficients," *Solar Energy*, vol. 17, no. 1, pp. 79–80, 1975.
- [23] J. A. Duffie and W. A. Beckman, *Solar Engineering of Thermal Processes*, Intersciences Publication, USA, 1991.
- [24] K. Sukhatme and S. P. Sukhatme, *Solar Energy: Principles of Thermal Collection and Storage*, Tata McGraw-Hill Education, New York, 1996.
- [25] H. Buchberg, I. Catton, and D. Edwards, "Natural convection in enclosed spaces: a review of application to solar energy collection," *ASME Journal of Heat Transfer*, vol. 98, no. 2, pp. 182–188, 1976.
- [26] K. Hollands, T. Unny, G. Raithey, and L. Konicek, "Free convective heat transfer across inclined air layers," *ASME Journal of Heat Transfer*, vol. 98, no. 2, 1976.
- [27] N. Shanmugam, M. Selvam, K. Srinivasan, S. John, and B. Sheno, "Black nickel-tin selective coatings for solar thermal energy conversion," *Metal Finishing*, vol. 82, no. 10, pp. 91–95, 1984.

Research Article

A Solar Heating and Cooling System in a Nearly Zero-Energy Building: A Case Study in China

Zhifeng Sun,^{1,2} Yaohua Zhao,¹ Wei Xu,² Xinyu Zhang,² Huai Li,² Min Wang,² Tao He,² and Dongxu Wang²

¹College of Architecture and Civil Engineering, Beijing University of Technology, Beijing 100124, China

²Institute of Building Environment and Energy, China Academy of Building Research, Beijing 100013, China

Correspondence should be addressed to Xinyu Zhang; zxyhit@163.com

Received 5 January 2017; Revised 21 April 2017; Accepted 18 May 2017; Published 18 July 2017

Academic Editor: Michel Feidt

Copyright © 2017 Zhifeng Sun et al. This is an open access article distributed under the Creative Commons Attribution License, which permits unrestricted use, distribution, and reproduction in any medium, provided the original work is properly cited.

The building sector accounts for more than 40% of the global energy consumption. This consumption may be lowered by reducing building energy requirements and using renewable energy in building energy supply systems. Therefore, a nearly zero-energy building, incorporating a solar heating and cooling system, was designed and built in Beijing, China. The system included a 35.17 kW cooling (10-RT) absorption chiller, an evacuated tube solar collector with an aperture area of 320.6 m², two hot-water storage tanks (with capacities of 10 m³ and 30 m³, respectively), two cold-water storage tanks (both with a capacity of 10 m³), and a 281 kW cooling tower. Heat pump systems were used as a backup. At a value of 25.2%, the obtained solar fraction associated with the cooling load was close to the design target of 30%. In addition, the daily solar collector efficiency and the chiller coefficient of performance (COP) varied from 0.327 to 0.507 and 0.49 to 0.70, respectively.

1. Introduction

The building sector accounts for more than 40% of the global energy consumption [1]. The total energy consumption of Chinese buildings (i.e., 16 billion tons of standard coal) accounts for 20.7% of the total national end energy consumption [2]. Building energy consumption may be lowered by reducing building energy requirements and using a renewable energy system. However, owing to indoor facilities and human activity, basic heating and cooling loads must be met. The corresponding building energy consumption can be reduced by using a renewable energy system, such as a solar energy system and a heat pump system, which are the most suitable renewable energy systems for the building sector. Heat pump systems are normally driven by grid electricity. Solar energy systems can produce electricity, thermal energy for heating and cooling, and can be used with a chiller to meet building energy requirements. The solar energy systems use less grid electricity than the heat pump systems. Therefore, based on the potential energy-saving effect, a solar heating and cooling system

(SHCS) represents the most desirable option for the building sector [3, 4].

An SHCS can supply cooling energy for the chiller during the summer and heat in the winter. A typical SHCS equipped with an absorption chiller is shown in Figure 1. The chiller, solar collector, and thermal energy storage (TES) are the main components of the SHCS, and each influences the performance of the other components. Adsorption chillers and absorption chillers are the two main types of chiller available on the current SHCS market. At values of 0.45 to 0.8, the coefficient of performance (COP) of absorption cooling systems is better than that (0.2 to 0.6) of adsorption systems [5–11]. Most (~70% of) chillers used in European SHCS are equipped with absorption chillers [12], and recent statistics show that the single-effect absorption chiller is a popular choice [5–8, 13]. Cabrera et al. [14] compared the cost of different types of solar collector used in office buildings and hotels in Madrid and Copenhagen, respectively. The results showed that in the case of the parabolic trough solar collectors (PTC), the energy costs for cooling are (i) similar to those of flat plate solar collectors (FPC) and (ii) lower than

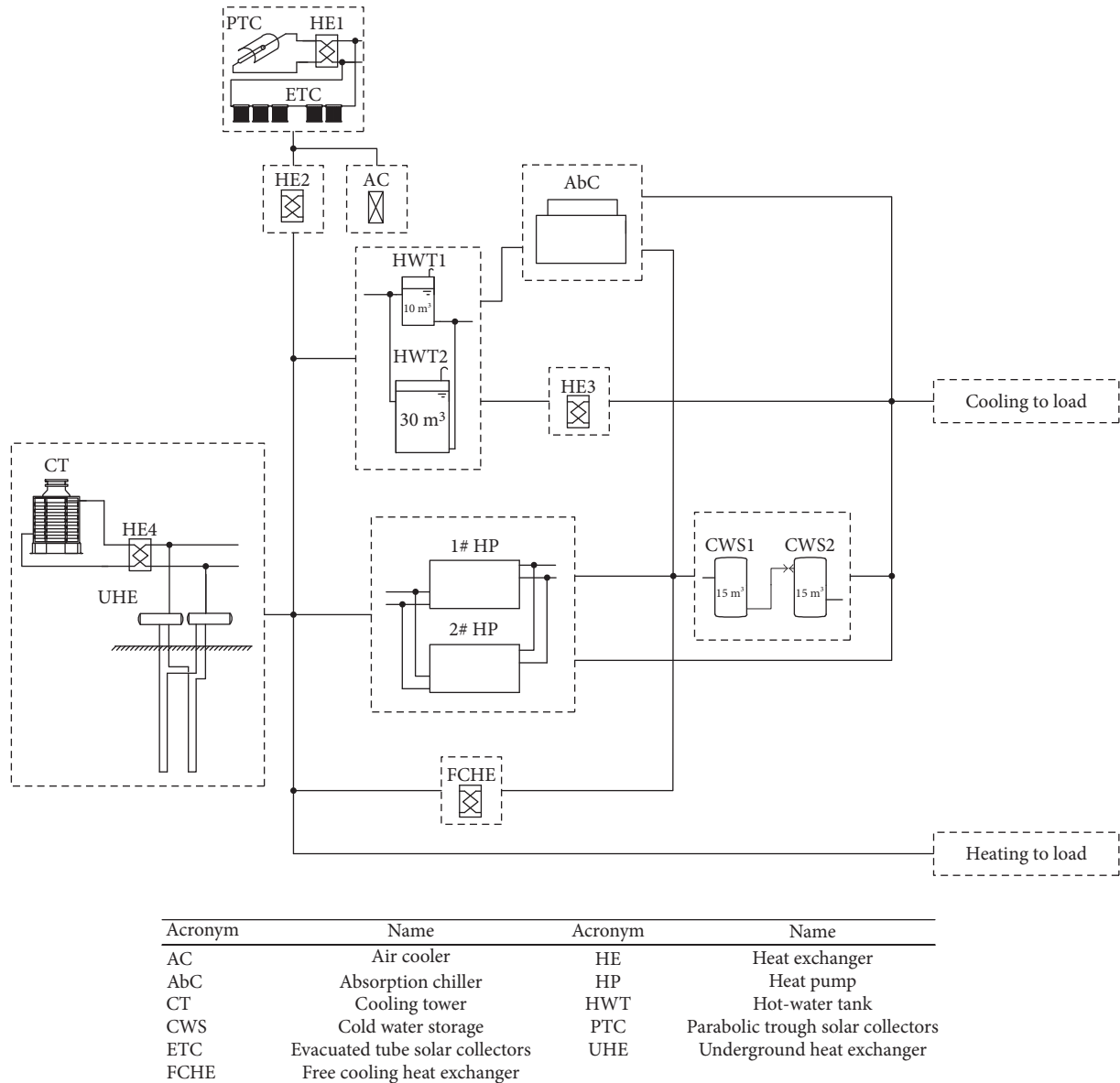


FIGURE 1: General concept of SHC in nZEB.

those of evacuated tube solar collectors (ETC) and compound parabolic solar collectors (CPC). A study of the solar cooling system in Thailand showed that the cost of the absorption chiller and solar collector represented most of the initial investment [15]. Owing to natural variations in solar irradiation, a TES is essential for controlling fluctuations in the heat transfer fluid temperature supplied to the chiller. If cooling demand is less than the required, TES is used to store the cooling energy for further load requirements. The SHCS consisting of single-effect LiBr/H₂O absorption chillers are used in China and other countries (see in Table 1). However, most Chinese SHCS consist of two TESs, and (in recent years) other countries have adopted this practice. Backup energy is crucial for buildings with heating requirements. ETCs are applied in China, whereas FPCs are used mainly in other countries. In fact, China is the largest producer of solar collectors and in 2012,

ETCs comprised 90% of all collectors [16]. Owing to their high performance and low cost, ETCs are also used in SHCS [15, 17–21].

These studies reveal that most SHCSs have been used in conventional buildings. However, some new buildings have been designed in accordance with the national requirements for energy efficiency. The load requirement of nearly zero-energy buildings (nZEB) and net zero-energy buildings (NZEB) differs from that of a conventional building. The application of SHCSs in nZEB and/or NZEB has recently been reported. Moldovan et al. [36] proposed a methodology for determining the optimal energy mix for heating and cooling that transforms a low-energy building to nZEB. In that work, a climatic profile with unbalanced heating and cooling demands through the year was considered. The methodology was applied to a research and development laboratory building in Transilvania University of Brasov, and the optimal

TABLE 1: Characteristics of some conventional SHCSs equipped with a single-effect absorption chiller.

Site	Chiller cooling capacity (kW)	Solar collector/aperture area (m ²)	TES/volume (m ³)		Auxiliary energy source	Air conditioning building type/area (m ²)	Reference
			Heat	Cool			
Shenzhen, China	2X7	ETC/76 + FPC/41	5	5	n.a.	Guest room/80	[22]
Rushan, China	100	ETC/540	8 + 4	6	Oil boiler	Exhibition center/1000	[23]
Tianpu, China	200	ETC/812	1	1200	Ground source heat pump	Office/8000	[24]
Tongzhou, China	105	ETC/228	10	15	Ground source heat pump	Laboratory, partly office/6552	[25]
Beiyuan, China	360	ETC/655	40	30	Electric boiler	Office/3000	[26]
Haikou, China	316	ETC/1492	45	30	Screw chiller	Library/20200	[27]
Qingdao, China	264	FPC/638	12	No	District heating plant	Office/5800	[28]
Dalian, China	200	ETC/733	30+ 24	No	Electric heater	Office/2000, Heating area/4120	[29]
Shunyi, China	176	ETC/523.92	15	8	Biomass boiler	Office/1850	[30]
UC3M, Spain	35	FPC/50	2	No	No	House/80	[31]
CIESOL, Spain	70	FPC/160	2 × 5	No	Electric heater	Institutional building/1100	[4, 32]
Hongkong, China	4.7	FPC/38	2.75	No	Electric heater	n.a.	[33]
Reunion Island, France	30	Double glazed FPC/90	1.5	1	No	Classroom/216	[34]
Cardiff, UK	4.5	ETC/12	No	1	No	Office/82	[19]
New Mexico, USA	70	FPC/124 + ETC/108	34	7 × 50	District energy supply plant	Educational building/7000	[20, 35]
Oberhausen, Germany	35.17	ETC/108	6.8	1.5	No	Office/108	[21]
SERT, Thailand	35.17	ETC/72	0.4	0.2	LPG boiler	Office/n.a.	[15]

energy mix for nZEB was determined from numerical simulations and in-field meteorological data. In addition, Gallo et al. [37] analyzed the integration of photovoltaic (PV) solar domestic hot water and air conditioning systems in NZEB in Spain. The simulation results showed that PV systems play an important role in reducing the use of fossil fuels in NZEB and, hence, these systems may also play a key role in China.

This work focuses on the realization of nZEB in China. The energy supply systems applied in the demonstration buildings were analyzed, especially the concept of SHCS during the design and operating phases. Moreover, the performance of the SHCS was evaluated, via the monitoring data, and optimal conditions for further improving the efficiency of the system were suggested.

2. Building Description, System Design, and Measurements

2.1. Building Description. The building is located at 39°92'N latitude, 116°46'E longitude in Beijing and, based on the Koppen climate classification, experiences a Cwa (warm temperature, dry winter, and warm summer). The outdoor parameters for system design in Beijing (in accordance with Chinese standard GB 50736-2012: design code for heating

TABLE 2: Outdoor climate parameters for system design in Beijing.

Parameters	Unit	Value
Temperature for heating	°C	-7.6
Temperature for ventilation in winter	°C	-3.6
Temperature for air conditioning in winter	°C	-9.9
Relative humidity for air conditioning in winter	%	44
Dry-bulb temperature for air conditioning in summer	°C	33.5
Wet-bulb temperature for air conditioning in summer	°C	26.4
Temperature for ventilation in summer	°C	29.7
Relative humidity for ventilation in summer	%	61
Average temperature for air conditioning in summer	°C	29.6
Average wind speed in summer	m/s	2.1
Average wind speed in winter	m/s	2.6

ventilation and air conditioning of civil buildings) are shown in Table 2. The four-floor office building, with a total cooling area of 4025 m², has 40 office rooms, one conference room, and four meeting rooms.

Details of the building envelope are provided in the following section.

The walls in this building were externally insulated. In addition, the external wall has a decorative coating (2 mm), and the outer layer consists of aerated concrete blocks (200 mm) and a decorative board integrated with an ultrathin vacuum insulation board (25 mm). Values of $0.24 \text{ W}/(\text{m}^2\cdot\text{K})$ and $0.16 \text{ W}/(\text{m}^2\cdot\text{K})$ were obtained for the onsite test-yield heat transfer coefficient of the external wall and roof, respectively. Furthermore, the aluminum alloy window used in the building has the following characteristics: general heat transfer coefficient: $1.0 \text{ W}/(\text{m}^2\cdot\text{K})$, shading coefficient: 0.26, window glass: tempered glass with a 5 mm low-emission film, vacuum layer: 2 mm, glass: 5 mm, air layer: 27 mm, and tempered glass: 5 mm. The vacuum glass used in the window had a transmittance of 38% and an airtightness performance rank of 8 (based on the Chinese national energy efficiency standard GB 50189-2005: design standard for energy efficiency of public buildings). The measures aimed at reducing the thermal bridge in the structure were also taken to further lower the building energy requirements for heating and cooling.

2.2. Load Requirement and System Scheme. The detailed design of the building envelope lists the requirements for the heating and cooling loads. For example, fresh air and sunlight are necessary for people inside the building and (although resulting in energy consumption for cooling) helpful in lowering the heating requirement, respectively. The loads for heating in winter and cooling in summer were calculated in accordance with the Chinese energy efficiency standard (GB 50189-2005: design standard for energy efficiency of public buildings). The load is composed of three components, namely, the basic heating/cooling load, load for fresh-air treatment, and load for humidity treatment. The basic heating/cooling load is generated by the building envelope, whereas the other two components vary with the number of people in the building. A space heating load of 66574.7 W ($16.54 \text{ W}/\text{m}^2$) was calculated, and a fresh-air requirement of $10,570 \text{ m}^3/\text{h}$ yielded a heating load of 90069.5 W . In addition, a value of $-135 \text{ kg}/\text{h}$ (“-” refers to the humidity that must be removed from the building) was determined for the load associated with dehumidification. Therefore, the maximal hourly cooling load, fresh-air requirement, cooling load for fresh-air treatment, and load for dehumidification were 148934.8 W , $10,570 \text{ m}^3/\text{h}$, 26062.9 W , and $-129.99 \text{ kg}/\text{h}$, respectively. The HVAC system should fulfill the heating and cooling requirements. The cooling load, 148934.8 W ($37.00 \text{ W}/\text{m}^2$), is higher than the heating load (66574.7 W). Therefore, the capacity of the system is decided by the cooling load and the fresh-air treatment load in the summer. Fresh air is essential for people inside an extremely airtight building, and hence the load for this treatment is required throughout the year.

2.3. General Concept of System Design. The general concept of an SHCS is shown in Figure 1. The SHCS consists of six circuits, namely, the solar collecting circuit, heat storage circuit, heat to absorption chiller circuit, supply heat/cold energy to building circuit, underground heat exchanger circuit, and cooling tower circuit. In summer time, the solar collectors

collect the heat from the sun and the water in the hot-water tanks are heated. Moreover, the absorption chiller starts working when the temperature in the tanks reach the start temperature required for driving this operation. The resulting cooling energy is stored in the cold-water tank and is later supplied to the building. When the cooling requirement is extremely high, the heat pumps start to work. In winter time, heat is supplied to the building if the temperature in HTWs is sufficiently high. Otherwise, the heat will be used to keep the solar collectors warm during winter nights. The heat supplied to the building comes mainly from the heat pumps.

2.4. Solar Collector System. The roof of the building was divided into two parts. Six light tubes, for guiding natural light into the conference room, were installed at the south of the roof covering the room. The medium-temperature PTC, with an aperture area of 30 m^2 , was installed on the northern part of the roof, and heat transfer oil was used as the heat transfer medium.

The U-type evacuated tube solar collector with a CPC reflector was installed on the lower part of the roof, which was filled with ETCs to maximize heat absorption from the sun. The ETC field, 320.6 m^2 (Figure 2), was tilted by 25° with respect to the roof. When the cooling load is higher than the heating load, this angle enables high heat absorption (by the solar collector) in the summer.

The ETC used in the system was developed as part of the 11th Chinese national scientific project—Large Scale Application of Solar Energy in Buildings (number 2006BAJ01A11). The instantaneous efficiency curve can be described by the following equation:

$$\eta = 0.691 - 0.830U - 0.0035G(U)^2, \quad (1)$$

where η , G , and U are the instantaneous efficiency of the solar collector, solar irradiance (W/m^2), and the reduced temperature difference ($\text{m}^2\cdot\text{K}/\text{W}$), respectively.

In summer and winter, water and an ethylene glycol aqueous solution (to prevent freezing), respectively, are used as the heat transfer media in the circuit. Overheating of the ETC and solar system in summer was prevented by using a rooftop heat exchanger to release the heat to the surrounding air.

2.5. Thermal Energy Storage. Based on the experience from projects in China and other countries [15, 19, 21, 34], two types of TES were used in this system. The air conditioning equipment was tested in a lab, and a 30 m^3 rectangular steel water tank was reused for heat storage. The aim here was to ensure that a rapid temperature increase and consequent cold-water generation were induced by the heat absorbed from the sun (by the solar collector) in the morning. A 10 m^3 rectangular steel water tank, which was also used in the heating time, was added. A 50 mm rubber sponge was used as the insulation material for the tanks. The water temperature for the heating requirement is lower than the water temperature required to generate cooling water from the absorption. Moreover, the solar energy is fully utilized by using two tanks during the heating season.



FIGURE 2: Photograph of evacuated tube solar collector with CPC reflectors.

Furthermore, to maximize solar energy absorption and reduce heat loss, two 10 m^3 cylindrical tanks were used as cooling storage. These tanks can store an hour of cooling energy generated by the absorption chiller. A 50 mm rubber sponge insulation material was also used. The heat storage and cooling storage tanks were installed in the conventional building and new building, respectively. During the intermediate seasons, heat from the sun was used to heat the fresh air of the room from winter to the cooling season. Similarly, from summer to the heating season, the cooling energy from the absorption chiller was used to cool the fresh air of the building.

The peak-valley electricity price for Beijing was adopted. The nighttime valley and peak hour electricity prices of this building are 0.3818 RMB/kWh and 1.4407 RMB/kWh, respectively. Based on the design of the system control, money is saved because the heat pump operates during the night to store energy in the cooling tank.

2.6. Absorption Chiller and Cooling Tower. A single-effect LiBr- H_2O absorption chiller (WFC-10 RT, YAZAKI Corporation) with a rated cooling capacity of 35.17 kW (10-RT) was used in the HVAC system. According to the manufacturer, a COP of 0.7 is obtained when the chiller operates at a hot-water temperature, cooling water temperature, and output temperature of 87°C , 29°C , and 8°C , respectively. The cooling capacity of the chiller accounts for more than 30% of the cooling load.

The cooling tower, which rejects heat from the chiller water to the ambient air, has a capacity of 281 kW at $32/37^\circ\text{C}$ and an ambient air wet-bulb temperature of 28°C .

2.7. Heat Pump and Other Concepts. A ground source heat pump system was used in the nZEB as a principal energy source for cooling and heating. While the cooling energy from the absorption chiller cannot meet the load requirement, the heat pumps start. Two heat pumps were used, namely, (i) 99.5 kW (cooling)/103.7 kW (heating) and (ii) 50 kW (cooling)/51.7 kW (heating). The ground heat

exchanger system consisted of 20 double 80 m (depth) and 50 single 60 m (depth) U pipes.

As the building is for demonstration purposes, the following concepts were considered.

A free cooling concept was used for the building. In this case, a flat plate heat exchanger was installed in the cooling energy supply system. During the cooling season, and based on the load requirement, the energy from the cooling tower and underground pipe heat exchangers supplies cooling energy to the building through this exchanger. This reduces the cost of cooling with marginal pump power consumption.

A fresh-air supply system was used in the building. This building serves as a demonstration, and, therefore, different air conditioning units were used on different floors. In addition, variable refrigerant volume systems, radiation floor systems, radiation ceiling systems, and water loop heat pump systems were used on the first, second, third, and fourth floors, respectively.

2.8. Energy Consumption Monitoring System. An energy management system (EMS) was installed in the energy supply system. The EMS consists of three components: meters, data collectors, and energy consumption data management software. The electricity consumption, water volume, and energy for heating and cooling were measured and recorded. During electricity consumption monitoring, the electricity for air conditioning, lighting, plugs, power for the lift, and power for the EMS was measured. The electricity generated by the PV system (capacity of only 2.88 kWp), connected to the circuit for illumination, was also measured. The energy consumption monitoring system consisted of 68 electricity meters, 40 heat meters, and two water meters.

3. Parameters

To understand the performance of the system, the test results are presented by using a simple data reduction, as described in [38]. The useful energy gained from the sun by the solar collector can be expressed as

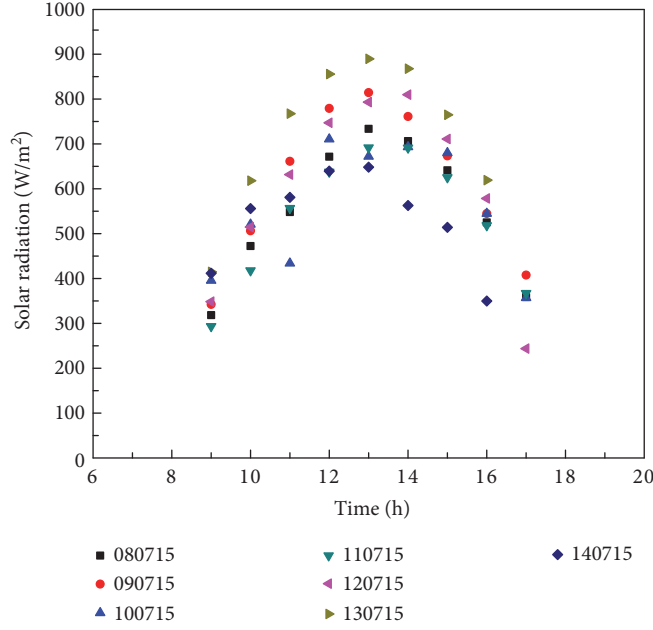


FIGURE 3: Incident solar irradiation from 08 July 2015 to 14 July 2015.

$$q_j = \sum_{i=1}^n \dot{V}_{ji} \rho_w c_{pw} (t_{dji} - t_{bji}) \Delta T_{ji} \times 10^{-6}, \quad (2)$$

where q_j is useful energy gained (MJ), \dot{V}_{ji} is average flow rate (m^3/s) of the solar collection system, c_{pw} is constant specific heat ($\text{J}/\text{kg}\cdot^\circ\text{C}$) of the heat transfer fluid, ρ_w is density (kg/m^3) of the heat transfer fluid, t_{dji} is inlet temperature ($^\circ\text{C}$) of the solar collector, t_{bji} is outlet temperature ($^\circ\text{C}$) of the solar collector, ΔT_{ji} is recorded time interval (s, ΔT_{ji} should be less than 600 s), and n is total number of recorded data points. q_j can be determined from the flow rate, t_{dji} and t_{bji} of the solar collection system, or by using a heat meter.

The efficiency (η) of the solar collection system may be expressed as follows:

$$\eta = \frac{q_j}{AH}, \quad (3)$$

where A and H are the area (m^2) of the collector and the solar irradiation (MJ/m^2) on the aperture area of the collector.

The heating energy consumed by the absorption chiller may be expressed as follows:

$$\dot{Q}_r = \sum_{i=1}^n \dot{V}_{ri} \times \rho_w \times c_{pw} \times (t_{dri} - t_{bri}) \times \Delta T_{ri} \times \frac{10^{-3}}{\Delta T}, \quad (4)$$

where \dot{Q}_r is heating energy (kW) consumed by the chiller, \dot{V}_{ri} is average flow rate (m^3/s) of the system, t_{dri} is temperature ($^\circ\text{C}$) of the water supplied to the chiller, t_{bri} is temperature ($^\circ\text{C}$) of the water returned from the chiller, ΔT_{ri} is recorded time interval (s, which should be less than 600 s), and ΔT_t is total recording time (s).

The cooling energy supplied by the absorption chiller is determined from

$$\dot{Q}_l = \sum_{i=1}^n \dot{V}_{li} \times \rho_w \times c_{pw} \times (t_{dli} - t_{bli}) \times \Delta T_{li} \times \frac{10^{-3}}{\Delta T_t}, \quad (5)$$

where \dot{Q}_l is cooling energy (kW) supplied by the chiller, \dot{V}_{li} is average flow rate (m^3/s) of the system, t_{dli} is temperature ($^\circ\text{C}$) of the water returned to the chiller, t_{bli} is temperature ($^\circ\text{C}$) of the water provided by the chiller, and ΔT_{li} is the recording time interval (s), which should be less than 600 s.

Following AHH et al. [21], the COP can be defined as the ratio of the evaporator cold capacity \dot{Q}_l to the heat input generation \dot{Q}_r :

$$\text{COP} = \frac{\dot{Q}_l}{\dot{Q}_r}. \quad (6)$$

The solar fraction of this SHC is given as

$$f = \frac{\dot{Q}_l}{\dot{Q}_t}, \quad (7)$$

where the solar fraction, f , corresponds to the ratio of the cooling/heating energy from absorption to the total cooling/heating energy supplied to the building (i.e., \dot{Q}_t is the cooling energy supplied to the building in summer and the heating energy in winter).

4. Results and Discussion

4.1. Collector Performance. The SHCS was evaluated via operating parameters (such as the solar irradiation and ambient temperature), which were recorded over a few days. The daily maximal solar irradiation ranged from $648 \text{ W}/\text{m}^2$ to $890 \text{ W}/\text{m}^2$ (Figure 3), while the average and maximal ambient temperatures ranged from 30.9°C to 35.0°C and 32.2°C to 39.0°C (Figure 4), respectively. In addition, the nominal

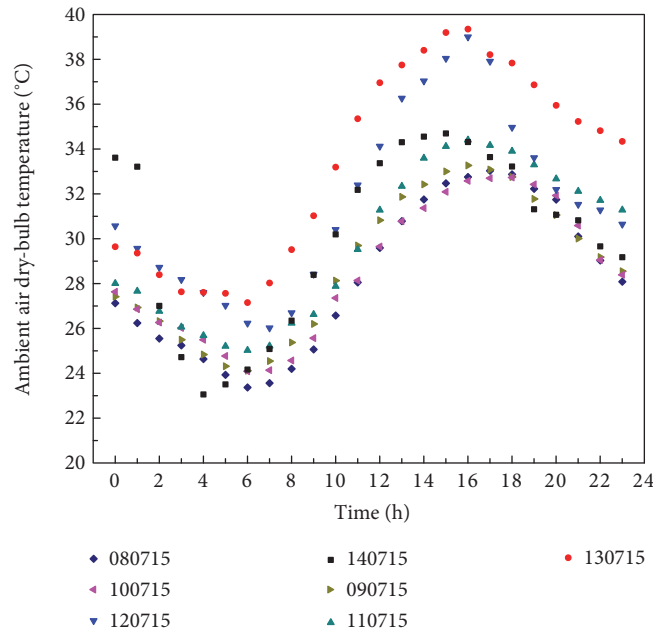


FIGURE 4: Ambient air dry-bulb temperature from 08 July 2015 to 14 July 2015.

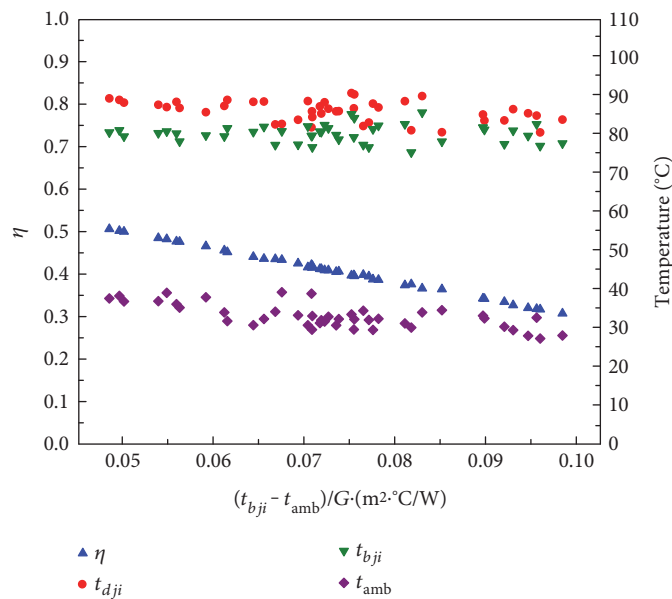


FIGURE 5: Field efficiency of instantaneous collectors.

heat transfer fluid temperature of absorption was $\sim 87^{\circ}\text{C}$, and the efficiency of collector field ranged from 0.327 to 0.507. This change in efficiency (see Figure 5) resulted mainly from changes in the meteorological conditions. The solar collector exhibited a higher heat loss than that reported by the manufacturer, but performed better under clear-sky conditions. Furthermore, dust collected on the CPC reflector persisted even after heavy rain, and in the summer of 2015, steam was released (via evaporation) from the collector fields. These factors all contributed to a decrease in the collector performance. Optimization of the pipe arrangements and regular

cleaning of the collector and CPC reflector surfaces will reduce the potential for evaporation and enhance the collector efficiency, respectively.

4.2. *Performance of the SHC.* The operating parameters recorded from 08 July 2015 to 14 July 2015 are shown in Figure 6. The figure shows the measured temperature of the inlet water to the absorption chiller generator (t_{dri}), temperature of the outlet water from the absorption chiller evaporator (t_{bli}), heat supplied by solar energy to the chiller (\dot{Q}_r), and cooling power load produced by the absorption chiller during

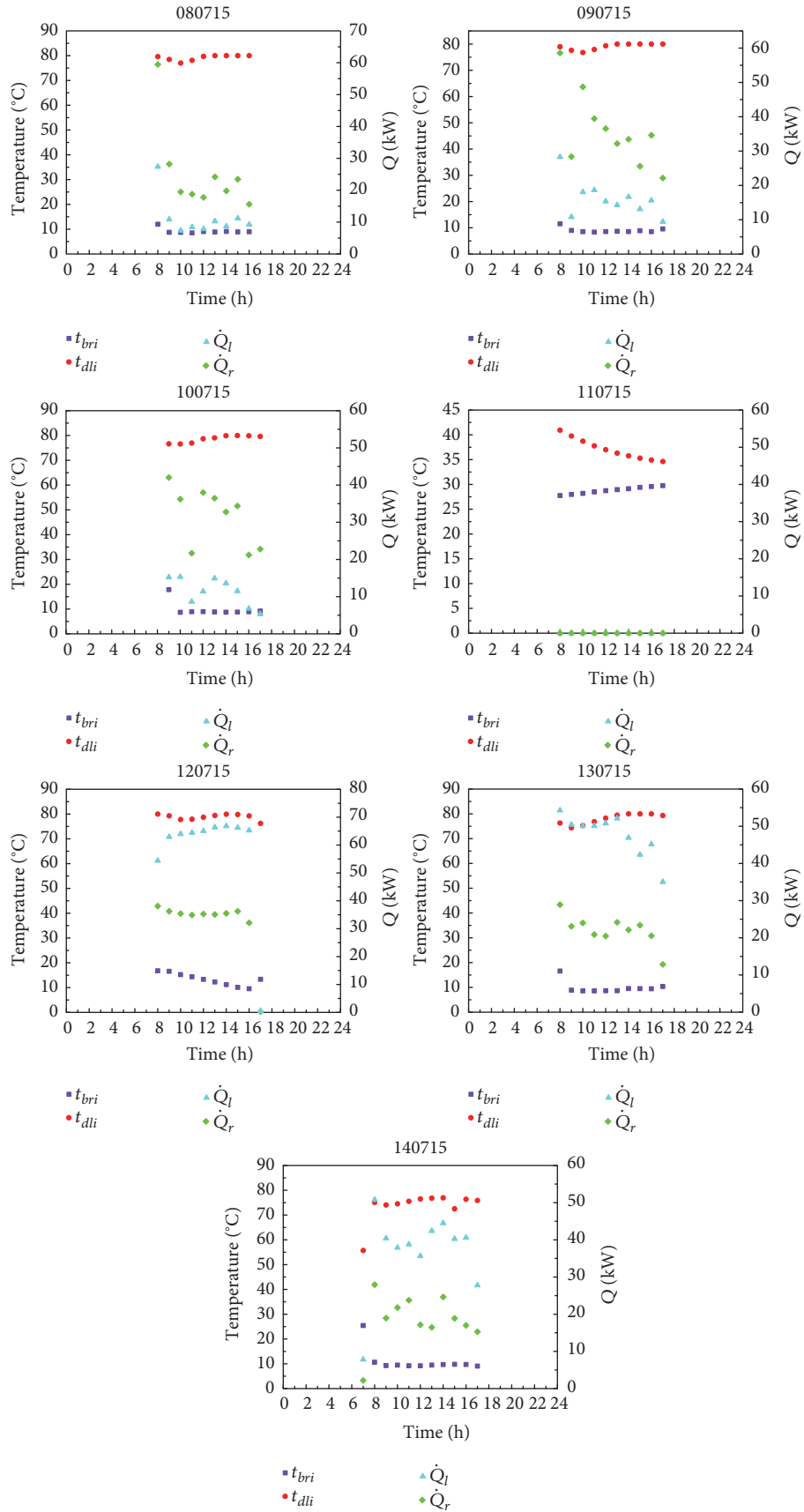


FIGURE 6: Instantaneous characteristics of SHC from 08 July 2015 to 14 July 2015.

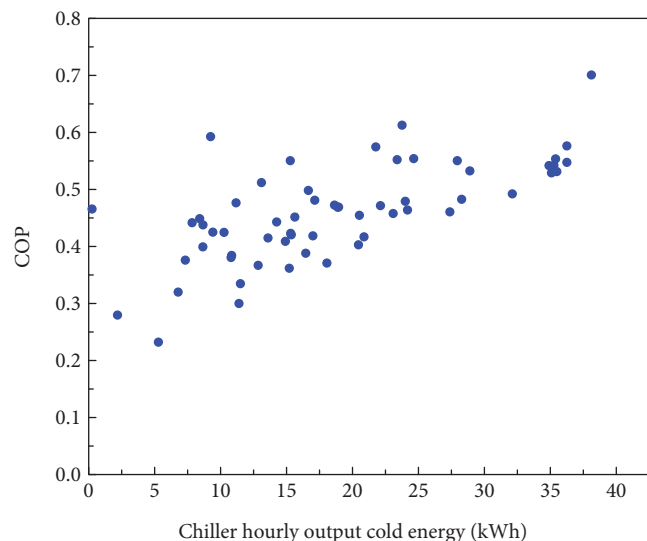


FIGURE 7: Dependence of the chiller daily average COP on the cold energy demand from 08 July 2015 to 14 July 2015.

the day time. The solar collector system and chiller were not operated during the day of 11 July 2015.

The chiller is started at a driving hot-water temperature of $\sim 77^{\circ}\text{C}$ (see Figure 6), which lies in the driving-temperature range (70°C – 95°C) specified by the chiller manufacturer. However, except for the day of 12 July 2015, the output cold power is lower than the nominal value. The operating data for 12 July 2015 show that the input heat power is close to the nominal value, and the temperature of the water to the chiller generator increased from 77.8°C to 80.0°C (see Figures 6–7); at the same time, the cold temperature to the load decreased from 16.8°C to 9.5°C . In addition, the calculated COP ranged from 0.49 to 0.70 and the maximum COP reached the nominal value. The inlet temperature and the heat power supplied to the chiller generator were both lower than the nominal value reported by the chiller manufacturer. Therefore, the chiller temperature and cold power to load were higher and lower, respectively, than the nominal value. However, based on the design concept, the solar collector system can satisfy both the temperature and heat-power requirements. Subsequent investigation of SHCS will focus on determining the underlying principle of and optimizing the SHCS operation.

The variation in COP on the aforementioned days is shown in Figure 7. As reported in a previous study [21], the COP varied with the output cold power supplied to the load. Furthermore, a maximum COP of 0.7 (the nominal value supplied by the chiller manufacturer) was obtained under clear-sky conditions.

A design target of 30% was set for the cooling energy covered by the absorption chiller, but a value of 25.2% was obtained during actual testing in the summer of 2015. The heat fluid of solar collector is water; during the winter of 2014–2015, most of the heat from solar energy was used to keep the solar collector warm during the night (less heat was used by the building).

4.3. Free Cooling Concept and PV System Performance. Though many technical measures were instituted for this nZEB, most of these measures were only demonstrated. For example, the free cooling concept, that is, the ground heat exchanger and the cooling tower constituting the main cooling source, fell short of expectations. A significant amount of work is required to fully exploit this concept. During operation, the solar thermal system and heat pump system are the main cooling/heating source.

The building-integrated photovoltaic was installed on the south wall. In 2015, the total power and daily average output from the PV system were 1031.43 kWh and 2.83 kWh, respectively. The output power is used for illumination of the public areas, and, hence, its contribution to the reduction of electricity consumption is trivial.

5. Conclusions

We presented an initial performance assessment of a solar heating and cooling system in an nZEB building. Values of 13,006 kWh and 38,656 kWh were recorded for the cooling energy supplied by the SHCS and the heat pumps, respectively. Furthermore, a value of 25.2%, which is very close to the design target of 30%, was obtained for the rate of SHCS contribution. The electricity meter revealed that the general energy consumption for cooling, heating, and light from 2014 to 2015 was $<23\text{ kWh/m}^2$. During the intermediate season, the SHCS met most of the load requirements for fresh-air treatment. Although the free cooling concept was adopted, this concept fell short of expectations under actual operating conditions, although the SHCS played an important role in conventional energy consumption reduction.

On sunny days, the daily efficiency of the solar collector and the COP of the chiller varied from 0.327 to 0.507 and 0.49 to 0.70, respectively. The energy requirements must be accurately predicted for a solar heating and cooling system applied in this nZEB building. The load requirements and characteristics of an nZEB differ from those of a conventional building. In the case of a conventional building, the load requirement and changes thereof are affected by outdoor conditions. In the case of an nZEB, changes in the outdoor temperature and solar irradiation have only a modest effect on the cooling load. The main load requirements of an nZEB are to (i) remove heat from equipment, such as personal computers, and (ii) provide energy for fresh-air treatment, which depends on the number of people inside the building. The load characteristics and capacity should be considered during the selection of a solar thermal system. In addition, TES is essential for balancing the load requirement and energy supply of the SHCS in an nZEB.

This building is a demonstration of an nZEB, and the energy system (including the SHCS) is under commission. The optimal operational measurements will be performed in accordance with the recorded data. Further work on the SHCS in an nZEB will focus on improving the efficiency of the solar collector and fully exploiting the use of TES. The phase change material will be carefully selected.

Nomenclature

A :	Aperture area of the solar collector, m^2
A_s :	Collector area per target cold capacity, m^2/kW
c_{pw} :	Specific heat at constant pressure, $kJ/(kg \cdot ^\circ C)$
G :	Solar irradiation on the aperture of the solar collector, W/m^2
H :	Solar irradiation on the aperture of the solar collector, MJ/m^2
\dot{V}_{ji} :	Average flow rate of the solar collecting system, m^3/s
\dot{V}_{li} :	Average flow rate of the cooling water from the chiller, m^3/s
\dot{V}_{ri} :	Average flow rate of the heating water to the chiller, m^3/s
\dot{Q}_l :	Cooling energy supplied by the chiller, kW
\dot{Q}_r :	Heating energy consumed by the chiller, kW
Q_j :	Useful energy gained by the solar collecting system, MJ
\dot{Q}_t :	Cooling or heating energy consumed by the building, kW
U :	The reduced temperature difference, $m^2 \cdot K/W$
t_{amb} :	Ambient temperature, $^\circ C$
t_{bji} :	Supply temperature of the solar collecting system, $^\circ C$
t_{bli} :	Supply water temperature from the evaporator of absorption chiller, $^\circ C$
t_{bri} :	Return water temperature from the generator of absorption chiller, $^\circ C$
t_{dji} :	Outlet temperature of the solar collecting system, $^\circ C$
t_{dli} :	Return water temperature to the evaporator of absorption chiller, $^\circ C$
t_{dri} :	Supply water temperature to the generator of absorption chiller, $^\circ C$.
<i>Greek symbols</i>	
ρ_w :	Density of the heat transfer media, kg/m^3
η :	Efficiency of the solar collecting system, %
$\Delta T_{(j,r,l)i}$:	Recording time interval, s
ΔT_t :	Total recording time, s.

Abbreviations

COP:	Coefficient of thermal performance for the absorption chiller
CPC:	Compound parabolic solar collector
EMS:	Energy management system
ETC:	Evacuated tube solar collector
FPC:	Flat plate solar collector
HVAC:	Heat ventilation and air conditioning
nZEB:	Nearly zero-energy building
NZEB:	Net zero-energy building
PTC:	Parabolic trough solar collector
SHCS:	Solar heating and cooling system
TES:	Thermal energy storage.

Conflicts of Interest

The authors declare that they have no conflicts of interest.

Acknowledgments

This work was funded by the Ministry of Science and Technology, China (2016YFC0700405).

References

- [1] United Nations Environment Program, *Buildings and Climate Change*, Paris, 2009.
- [2] W. G. Cai, Y. Wu, Y. Zhong, and H. Ren, "China building energy consumption: situation, challenges and corresponding measures," *Energy Policy*, vol. 37, pp. 2054–2059, 2009.
- [3] U. Desideri, S. Proietti, and P. Sdringola, "Solar-powered cooling systems: technical and economic analysis on industrial refrigeration and air-conditioning applications," *Applied Energy*, vol. 86, pp. 1376–1386, 2009.
- [4] S. Rosiek and F. J. Batlles, "Renewable energy solutions for building cooling, heating and power system installed in an institutional building: case study in southern Spain," *Renewable and Sustainable Energy Reviews*, vol. 26, pp. 147–168, 2013.
- [5] A. Ghafoor and A. Munir, "Worldwide overview of solar thermal cooling technologies," *Renewable and Sustainable Energy Reviews*, vol. 43, pp. 763–774, 2015.
- [6] Y. Fan, L. Luo, and B. Souyri, "Review of solar sorption refrigeration technologies: development and applications," *Renewable and Sustainable Energy Reviews*, vol. 11, pp. 1758–1775, 2007.
- [7] H.-M. Henning, "Solar assisted air conditioning of buildings - an overview," *Applied Thermal Engineering*, vol. 27, pp. 1734–1749, 2007.
- [8] X. Q. Zhai and R. Z. Wang, "A review for absorption and adsorption solar cooling systems in China," *Renewable and Sustainable Energy Reviews*, vol. 13, pp. 1523–1531, 2009.
- [9] I. Sarbu and C. Sebarhievici, "Review of solar refrigeration and cooling systems," *Energy and Buildings*, vol. 67, pp. 286–297, 2013.
- [10] D. S. Kim and C. A. I. Ferreira, "Solar refrigeration options – a state-of-the-art review," *International Journal of Refrigeration*, vol. 31, pp. 3–15, 2008.
- [11] R. Z. Wang, T. S. Ge, C. J. Chen, Q. Ma, and Z. Q. Xiong, "Solar sorption cooling systems for residential applications: options and guidelines," *mes de refroidissement a ` sorption solaire pour les Systeme ` sidentielles: options et recommandations applications re,* *International Journal of Refrigeration*, vol. 32, pp. 638–660, 2009.
- [12] C. Balaras, G. Grossman, H.-M. Henning et al., "Solar air conditioning in Europe - an overview," *Renewable and Sustainable Energy Reviews*, vol. 11, pp. 299–314, 2007.
- [13] M. Izquierdo, M. Venegas, P. Rodríguez, and A. Lecuona, "Crystallization as a limit to develop solar air-cooled LiBr-H₂O absorption systems using low-grade heat," *Solar Energy Materials & Solar Cells*, vol. 81, pp. 205–216, 2004.
- [14] F. J. Cabrera, A. Fernández-García, S. RMP, and M. Pérez-García, "Use of parabolic trough solar collectors for solar refrigeration and air-conditioning applications," *Renewable and Sustainable Energy Reviews*, vol. 20, pp. 103–118, 2013.
- [15] A. Pongtornkulpanich, S. Thepa, M. Amornkitbamrung, and C. Butcher, "Experience with fully operational solar-driven

- 10-ton LiBr/H₂O single-effect absorption cooling system in Thailand,” *Renewable Energy*, vol. 33, pp. 943–949, 2008.
- [16] X. Zhang, S. You, W. Xu, M. Wang, T. He, and X. Zheng, “Experimental investigation of the higher coefficient of thermal performance for water-in-glass evacuated tube solar water heaters in China,” *Energy Conversion and Management*, vol. 78, pp. 386–392, 2014.
- [17] R. Tang, Y. Yang, and W. Gao, “Comparative studies on thermal performance of water-in-glass evacuated tube solar water heaters with different collector tilt-angles,” *Solar Energy*, vol. 85, pp. 1381–1389, 2011.
- [18] L. J. Shah and S. Furbo, “Theoretical flow investigations of an all glass evacuated tubular collector,” *Solar Energy*, vol. 81, pp. 822–828, 2007.
- [19] F. Agyenim, I. Knight, and M. Rhodes, “Design and experimental testing of the performance of an outdoor LiBr/H₂O solar thermal absorption cooling system with a cold store,” *Solar Energy*, vol. 84, pp. 735–744, 2010.
- [20] M. Ortiz, H. Barsun, H. He, P. Vorobieff, and A. Mammoli, “Modeling of a solar-assisted HVAC system with thermal storage,” *Energy and Buildings*, vol. 42, pp. 500–509, 2010.
- [21] A. H. H. Ali, P. Noeres, and C. Pollerberg, “Performance assessment of an integrated free cooling and solar powered single-effect lithium bromide-water absorption chiller,” *Solar Energy*, vol. 82, pp. 1021–1030, 2008.
- [22] K. Sumathy and Z. HuangZ. Li, “Solar absorption cooling with low grade heat source - a strategy of development in South China,” *Solar Energy*, vol. 72, pp. 155–165, 2002.
- [23] Z. He, N. Zhu, F. Liu, and S. Guo, “Design and performance of a solar absorption air-conditioning and heat-supply system,” *Acta Energiæ Solaris Sinica*, vol. 22, pp. 6–11, 2001.
- [24] J. Li, N. Bai, W. Ma, L. Xianhang, and X. Jiang, “Large solar powered air conditioning-heat pump system,” *Acta Energiæ Solaris Sinica*, vol. 27, pp. 152–158, 2006.
- [25] X. Zhang, R. Zheng, X. Feng et al., “Two demonstrations of solar heating system and air-conditioning system in buildings in China,” in *Proceedings of ISES World Congress 2007*, pp. 926–929, Beijing: Tsinghua University Press, 2007.
- [26] L. Feng, D. Zhu, G. Xie, and G. Liu, “Performance and experiment of Beiyuan solar air conditioning system,” *Heating Ventilation AIR Conditioning*, vol. 40, pp. 84–86, 2010.
- [27] Z. Li, J. Nie, X. Zhang et al., “Application of solar cooling system in a campus library in Hainan, China,” *Energy Procedia*, vol. 30, pp. 730–737, 2012.
- [28] T. He, X. Zhang, Z. Huang, Y. Deng, L. Zhang, and C. Wang, *Report for Solar Heating and Cooling System in Qingdao*, 2008.
- [29] T. He, X. Zhang, Z. Huang, Y. Deng, L. Zhang, and C. Wang, *Test Report for Solar Heating and Cooling System in Dalian*, 2012.
- [30] T. He, X. Zhang, C. Wang et al., “Application of solar thermal cooling system driven by low temperature heat source in China,” *Energy Procedia*, vol. 70, pp. 454–461, 2015.
- [31] A. Syed, M. Izquierdo, P. Rodríguez et al., “A novel experimental investigation of a solar cooling system in Madrid,” *International Journal of Refrigeration*, vol. 28, pp. 859–871, 2005.
- [32] S. Rosiek and F. J. Batlles, “Integration of the solar thermal energy in the construction: analysis of the solar-assisted air-conditioning system installed in CIESOL building,” *Renewable Energy*, vol. 34, pp. 1423–1431, 2009.
- [33] Z. F. Li and K. Sumathy, “Experimental studies on a solar powered air conditioning system with partitioned hot water storage tank,” *Solar Energy*, vol. 71, pp. 285–297, 2001.
- [34] J. P. Praene, O. Marc, F. Lucas, and F. Miranville, “Simulation and experimental investigation of solar absorption cooling system in Reunion Island,” *Applied Energy*, vol. 88, pp. 831–839, 2011.
- [35] A. Mammoli, P. Vorobieff, H. Barsun, R. Burnett, and D. Fisher, “Energetic, economic and environmental performance of a solar-thermal-assisted HVAC system,” *Energy and Buildings*, vol. 42, pp. 1524–1535, 2010.
- [36] M. D. Moldovan, I. Visa, M. Neagoe, and B. G. Burduhos, “Solar heating & cooling energy mixes to transform low energy buildings in nearly zero energy buildings,” *Energy Procedia*, vol. 48, pp. 924–937, 2014.
- [37] A. Gallo, B. T. Molina, M. Prodanovic, J. G. Aguilar, and M. Romero, “Analysis of net zero-energy building in Spain. Integration of PV, solar domestic hot water and air-conditioning systems,” *Energy Procedia*, vol. 48, pp. 828–836, 2014.
- [38] X. Zhang, W. Xu, T. He et al., “Solar thermal system evaluation in China,” *International Journal of Photoenergy*, vol. 2015, Article ID 163808, 12 pages, 2015.

Research Article

Thermal Storage Capacity and Night Ventilation Performance of a Solar Chimney Combined with Different PCMs

Jun Lu, Xiaolong Gao, Qianru Li, and Yongcai Li

Key Laboratory of the Three Gorges Reservoir Region's Eco-Environment, Ministry of Education, Chongqing University, Chongqing, China

Correspondence should be addressed to Yongcai Li; yongcail85@163.com

Received 8 February 2017; Revised 5 April 2017; Accepted 22 May 2017; Published 5 July 2017

Academic Editor: Alibakhsh Kasaeian

Copyright © 2017 Jun Lu et al. This is an open access article distributed under the Creative Commons Attribution License, which permits unrestricted use, distribution, and reproduction in any medium, provided the original work is properly cited.

Thermal storage capacity and airflow rate of a solar chimney combined with different PCMs are numerically studied during nighttime. PCMs with phase change temperatures of 38°C, 44°C, 50°C, and 63°C are selected in this numerical study. Results show that the maximum average ventilation rate of 610 kg/m² and maximum thermal storage of 4750 kJ/m² are achieved at the phase change temperature of 38°C. However, for phase change temperature of 63°C, night ventilation does not occur under the identical conditions. The findings reveal that a lower phase change temperature can increase the chargeability (and therefore the dischargeability) of a solar chimney, since a higher phase change temperature demands higher solar radiation intensity and longer charging time for a solar chimney. For PCM with a phase change temperature of 44°C, most of the heat stored in PCM is lost to ambient through glass cover by radiation and only a small portion is used for heating the air within air channel.

1. Introduction

A solar chimney is a natural draft system that has already been applied in the building ventilation widely and has attracted the interest of many scholars around the world. Extensive numerical or/and experimental studies in terms of evaluating ventilation performance [1–5] and optimizing design of solar chimney [6–10] have been performed. A solar chimney consisted of roof solar collector, and Trombe wall was experimentally investigated by Khedari et al. [11]. Results show that in June–July of a hot and humid climate, the temperature, air velocity, and flow rate per area of a solar chimney inside the room varies from 35–37°C, 0.02–0.08 m/s, and 0.01–0.02 m³/s per 1 m², respectively. Hirunlabh et al. [12] performed a numerical study on four new configurations of roof solar collector under Thailand weather conditions. By using the new configuration of roof solar collector, the highest volume flow rate of air is 0.072 m³/s or 0.0206 m³/s per 1 m² of a solar chimney. Chungloo and Limmeechokchai found that with a solar chimney, the indoor temperature can be reduced by 1.0–3.5°C at high ambient temperature and high solar intensity

(32.0–40.01°C) in the daytime [13]. Miyazaki et al. [14] numerically investigated the effects of solar chimneys on thermal load mitigation of office buildings in Japan. The results showed that in the natural ventilation mode, a larger chimney area was required to reduce the passive cooling load of the building. Between 10 a.m. and 12 p.m. of an average day in May, when the chimney width is 4 m, the cooling load was less than that of the no solar chimney design.

Studies reveal that the height [6], chimney position [7], type of absorber [8], width and depth of cavity [15], inclination angle [16], and the insulation or thermal mass in the solar chimney [17] are the primary factors that should be considered when designing a solar chimney. The above analysis indicated that solar chimney possesses the potential of cooling effect and cooling load reduction, and the potential can be enhanced by optimizing the designing factors. The available studies mainly concentrated on the performance characteristics of solar chimney during the daytime. If the night ventilation or all-day ventilation can be achieved, the solar energy utilization as well as the indoor thermal comfort would be greatly improved. Amori and Mohammed [18]

experimentally investigated the effect of integrating phase change material (PCM) in a solar chimney and found that integrating a solar chimney with PCM yield longer ventilation period after the sunset. In this paper, a PCM unit is integrated into the solar absorber of the chimney to take advantage of PCM's isothermal phase change characteristic as well as high latent heat density. The PCM absorbs the heat radiated from the sun and stores heat during the daytime and then releases the absorbed heat during the nighttime. By this means, night ventilation can be achieved without consuming any additional energy sources. This has been indicated by Liu and Li's study [19], in which the performance of a conventional vertical solar chimney and a PCM-based one with the same geometry was compared. In their study, the paraffin wax with phase change temperature of 38–42°C was selected as PCM. It was found that the effective ventilation time of the PCM-based solar chimney can be as long as 13 h 50 min, while the conventional one's ventilation time is only 1 h 20 min. Similarly, Zhou and Pang [20] experimentally studied the thermal behavior of a system with a collector-storage wall using PCM with phase change temperature $26 \pm 1^\circ\text{C}$. The experimental results indicated that by integrating PCM in the wall, the whole ventilation period of the system is as long as 17.5 h.

It should be noticed that the PCM can significantly influence the ventilation performance of the PCM-based solar chimney, especially the phase change temperature of the PCM, which is a vital factor among the physical properties of the PCM. It directly affects the absorber temperature and consequently affects the air flow rate and thermal storage capacity.

Based on the findings from above literatures, a mathematical model is developed to examine the ventilation performance and thermal storage capacity of a solar chimney using different PCMs under hot summer climatic conditions. The results of this paper could help to enhance the performance of such a PCM-based solar chimney by optimizing the phase change temperature.

2. Description of Mathematical Model

The schematic diagram of the PCM-based solar chimney is shown in Figures 1 and 2. The system mainly consists of glazing cover, air cavity, heat absorber plate, PCM container, and extruded insulation panels.

2.1. Calculation of the Energy Stored during the Day. The inlet and outlet of this system are closed when PCM is storing the solar energy during the day. Solar radiation passes through the glazing cover and is absorbed by the absorber. Then, the absorbed energy is used to raise the temperature of PCM. When the PCM temperature reaches its phase change temperature, the PCM starts to melt and stores latent heat simultaneously. During this period, the temperature of the PCM remains relatively constant.

Applying the energy balance concept on the glazing cover and the absorber plate, the following equations are given:

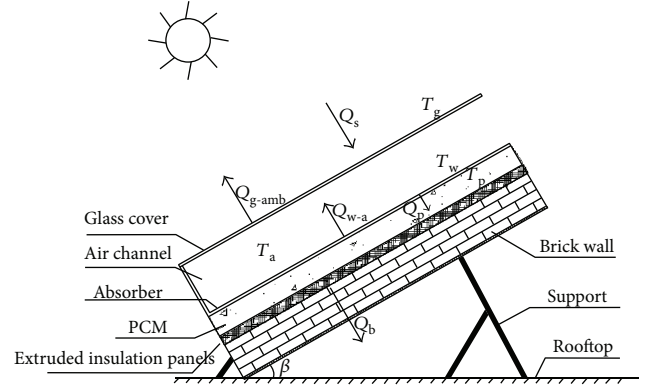


FIGURE 1: Schematic diagram of the PCM-based solar chimney during daytime.

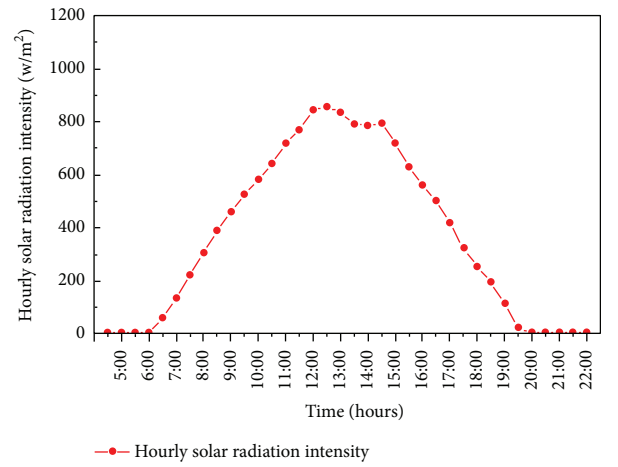


FIGURE 2: Hourly solar radiation intensity for June 26, 2016, in Chongqing, China [27].

$$\begin{aligned} \rho_g C_g \delta_g A_g \frac{dT_g}{dt} &= \alpha_g q_s A_g + h_{r,w-g} (T_w - T_g) A_w - U_t (T_g - T_{amb}) A_g, \\ \rho_w C_w \delta_w A_w \frac{dT_w}{dt} &= \tau_g \alpha_w q_s A_w - h_{r,w-g} (T_w - T_g) A_w - h_{w-p} (T_w - T_p) A_w. \end{aligned} \quad (1)$$

Theoretically, the glass receives heat from solar radiation and radiative heat from the absorber plate while it loses energy to ambient. The absorber plate, made by a thin stainless steel with high thermal conductivity, is used to absorb solar energy. Hence, it is reasonably assumed that there is no thermal gradient across the thickness of the absorber plate. Consequently, the absorber plate absorbs solar radiation through the glass cover while releases heat to the glass cover and the PCM.

In this paper, the PCM is sealed in a metallic container, which is assumed to be in good thermal contact with the PCM. And the absorber plate serves as a heat exchanger between the air and the container. Hence, the control volume method for discrete one-dimensional phase change problems is adopted. The PCM container is divided into n ($n = 10$) cells

along the thickness direction. The one-dimensional energy equation for each internal node “ i ” can be written as follows:

$$\begin{aligned} \rho_p C_p dx A_w \frac{dT_{p,i}}{dt} &= h_{w-p} (T_w - T_{p,i}) A_w - \frac{k_p}{dx} (T_{p,i} - T_{p,i+1}) A_w & i = 1, \\ \rho_p C_p dx A_w \frac{dT_{p,i}}{dt} &= \frac{k_p}{dx} (T_{p,i-1} - T_{p,i}) A_w - \frac{k_p}{dx} (T_{p,i} - T_{p,i+1}) A_w & i = 2, 3, \dots, n-1, \\ \rho_{\text{eff}} C_{\text{eff}} dx A_w \frac{dT_{p,i}}{dt} &= \frac{\kappa_{\text{eff}}}{dx} (T_{p,i-1} - T_{p,i}) A_w - U_{\text{ins}} (T_{p,i} - T_{\text{amb}}) A_w & i = n, \\ \rho_p C_p dx A_w \frac{dT_{p,i}}{dt} &= \frac{k_p}{dx} (T_{p,i-1} - T_{p,i}) A_w - U_b (T_{p,i} - T_{\text{amb}}) A_w & i = n. \end{aligned} \quad (2)$$

The heat transfer between different components of this system is shown in Figure 1, where q_s is the solar radiation intensity.

- (1) The thermal storage capacity of the PCM

$$q_x = q_{w-p} - q_b. \quad (3)$$

- (2) The radiative heat transfer coefficient between the absorber and glass cover has been obtained from [21]

$$h_{r,w-g} = \frac{\sigma (T_w^2 + T_g^2) (T_w + T_g)}{\xi_w^{-1} + \xi_g^{-1} - 1}. \quad (4)$$

- (3) The overall heat loss coefficient from the glass cover to ambient U_t includes the convection caused by wind and radiative heat transfer from glass cover to sky. It can be written as

$$U_t = h_{r,g\text{-sky}} + h_{\text{wind}}. \quad (5)$$

The radiative heat transfer coefficient from the glass cover to the sky may be obtained from [21]

$$h_{r,g\text{-sky}} = \frac{\sigma \xi_g (T_g + T_{\text{sky}}) (T_g^2 + T_{\text{sky}}^2) (T_g - T_{\text{sky}})}{T_g - T_{\text{amb}}}. \quad (6)$$

The sky temperature T_{sky} and the convective heat transfer coefficient between the glazing cover and the surrounding air, which is affected by wind speed, can be calculated by [21, 22]

$$\begin{aligned} T_{\text{sky}} &= 0.0552 T_{\text{amb}}, \\ h_{\text{wind}} &= 2.8 + 3.0 V_{\text{wind}}. \end{aligned} \quad (7)$$

- (4) The overall heat transfer coefficient between the PCM and the absorber plate h_{w-p} is given by

$$\begin{aligned} h_{w-p} &= \frac{1}{\delta_w/k_w + dx/2k}, \\ q_{w-p} &= h_{w-p} (T_w - T_p). \end{aligned} \quad (8)$$

- (5) The heat that the PCM transfers to indoor is given by

$$\begin{aligned} q_b &= U_b (T_p - T_{\text{amb}}), \\ U_b &= \frac{1}{1/h_1 + \Delta w_1/k_{w1} + \Delta w_2/k_{w2}}. \end{aligned} \quad (9)$$

2.2. Calculation of the Air Flow Rate during the Night. The discharging period begins when the chimney starts ventilating during the night. The air exchanges heat with the absorber plate as it passes through the air channel and then flows to ambient through the outlet. For various components of the system, the energy balance equations for the discharging period are presented below.

Applying the energy balance concept on the glass cover, absorber plate, and air flow in the air channel, the following equations are yielded:

$$\begin{aligned} \rho_g C_g \delta_g A_g \frac{dT_g}{dt} &= h_{r,w-g} (T_w - T_g) A_w + h_{cv,a-g} (T_a - T_g) A_g \\ &\quad - U_t (T_g - T_{\text{amb}}) A_g, \\ \rho_w C_w \delta_w A_w \frac{dT_w}{dt} &= h_{p-w} (T_p - T_w) A_w - h_{r,w-g} (T_w - T_g) A_w \\ &\quad - h_{cv,w-a} (T_w - T_a) A_w, \\ \rho_a C_a V_a \frac{dT_a}{dt} &= h_{cv,w-a} (T_w - T_a) A_w - h_{cv,a-g} (T_a - T_g) A_g \\ &\quad - m C_a (T_{\text{out}} - T_{\text{in}}). \end{aligned} \quad (10)$$

Assuming that the natural convection of the air occurs between the glazing cover and the absorber plate, the convective heat transfer coefficient $h_{cv,a-g}$ between the glazing cover and the air in the channel can be calculated as follows [23]:

$$\begin{aligned} h_{cv,a-g} &= h_{cv,w-a} = \frac{\text{Nu} \lambda_a}{\delta_a}, \\ \text{Nu} &= [0.06 - 0.017(\beta/90)] \text{Gr}^{1/3}, \end{aligned} \quad (11)$$

where β is the inclination angle of the absorber plate ($\beta = 90^\circ$ in this study) and the Grashof number is

$$\text{Gr} = \frac{g |T_w - T_g| \delta_a^3}{\nu^2 T_a}. \quad (12)$$

It is assumed that the mean air temperature inside the chimney is equal to the average value of the absorber temperature and the glazing cover temperature at the absorber side.

$$T_a = \frac{T_w + T_g}{2}. \quad (13)$$

The relationship between inlet air temperature and outlet air temperature can be described as follows [24, 25]:

$$T_a = \gamma T_{in} + (1 - \gamma) T_{out}, \quad (14)$$

where γ , the mean temperature approximation coefficient, was found in the literature to be 0.74 [21, 22] and the inlet air temperature T_{in} can be regarded as the outdoor air temperature.

The airflow rate as a result of the buoyancy effect can be calculated as follows [26]:

$$m = \frac{C_d \rho_a A_{out}}{\sqrt{1 + A_r^2}} \sqrt{2g \sin \beta L \left(\frac{T_a}{T_{in}} - 1 \right)}, \quad (15)$$

where C_d is found in the literature to be 0.57 [26].

$$C_a = 1007 + 0.04(T_a - 300). \quad (16)$$

During the daytime, the initial state of all the PCM is in its solid phase and the whole system's temperature is assumed to be the same as the ambient temperature. For the night ventilation period, the temperature of each system component and the PCM temperature depend on the final charging conditions. The inlet air temperature is equal to the ambient temperature. The temperatures of T_w , T_g , T_p , and T_a as well as the airflow rate are obtained with a program solved in "MATLAB." The air outlet temperature T_o can be obtained with the mean air temperature and (14). With the developed code, the performance of the PCM-based solar chimney as well as the heat transfer between various components of the solar chimney has been investigated.

3. Analysis and Discussion of the Numerical Results

The input parameters of the proposed system are given in Tables 1 and 2. The ventilation time is scheduled for 19:00–7:00. The monthly average solar radiation at the horizontal in Chongqing, China is close to the total solar radiation of June, and the solar radiation on June 26 approaches to the daily average solar radiation of June. Therefore, the climatic parameters of June 26 in Chongqing obtained from [27] are applied in this study, and the solar radiation intensity is given in Figure 2.

This paper analyzes the effect of phase change temperature on the ventilation rate of a solar chimney under Chongqing climatic conditions. The PCMs used in this numerical study are myristoyl, dodecylic acid, myristelaidic acid, and palmitic acid, and their corresponding phase change temperatures are 38°C, 44°C, 50°C, and 63°C, respectively.

Figure 3 shows the stored energy and ventilation rate for different PCMs. It is seen that the higher the phase change temperature, the lower the energy storage and the ventilation rate per unit area of absorber. That is to say, the PCM with phase change temperature of 38°C has the best performance among the studied PCMs, while the PCM with phase change temperature of 63°C has the poorest performance. Specifically, for the PCM with phase

TABLE 1: Specifications of the solar chimney and the thermo-physical properties of PCM.

Cover	
Material	Glass
Dimension	1500 × 1000 × 8 mm
Surface coating	0.90
Absorber	
Plate	Aluminum
Thickness	2 mm
Surface coating	0.94
PCMs	
	Myristoyl Dodecylic acid Myristelaidic acid Palmitic acid
Melting temperature	38°C, 44°C, 50°C, 63°C
Thickness of PCM	40 mm
Gap	
Absorber plate to glass	200 mm
Insulation material	
Extruded insulation panels	30 mm

change temperature of 38°C, the solar chimney achieves the maximum energy storage of 4750 kJ/m² and the maximum ventilation rate of 610 kg/m². However, for the PCM with phase change temperature of 63°C, there is little energy stored in PCM, and consequently the airflow is not observed during 19:00–07:00.

Figure 4 shows the absorber temperature and the PCM temperature for four different PCMs when storing heat during daytime. As shown, the thermal behavior characteristics of PCM under the identical conditions are different. The temperature variations of PCM display a typical fully charging process for phase change temperatures of 38°C and 44°C, respectively. The melting times for these two PCMs are 5 and 7.5 h, respectively. However, for the phase change temperatures of 50 and 63°C, the maximum PCM temperatures are 49.6°C and 53°C at the end of charging process accordingly, indicating that PCMs are not fully melting. Especially for phase change temperature of 63°C, the PCM temperature even decreases after the peak solar radiation intensity. This is because the absorber surface temperature descends quickly with solar radiation intensity weakens due to the high surface temperature. Consequently, the sensible heat stored in PCM transfers to the absorber surface.

This indicates that a lower phase change temperature can increase the chargeability and dischargeability of the solar chimney. The larger amount of energy stored and discharged by the solar chimney and consequently a higher ventilation rate is achieved. A higher phase change temperature demands higher solar radiation intensity and longer charging time and results in poor chargeability of the chimney.

Figures 5–7 show the variations of air temperature and the transient ventilation rate with time.

It can be seen from Figures 5–7 that the changing trend of ventilation rate is similar to that of the air temperature

TABLE 2: Initial conditions for numerical modelling.

Item	Value	Item	Value	Item	Value
α_g	0.06	$K_{w2}, \text{Wm}^{-1} \text{K}^{-1}$	0.028	$\nu, \text{m}^2 \text{s}^{-1}$	19.5×10^{-6}
α_w	0.94	ρ_g, kgm^{-3}	2526	$U_w, \text{Wm}^{-2} \text{K}^{-1}$	26
τ_g	0.84	ρ_w, kgm^{-3}	2730	$h_p, \text{Wm}^{-2} \text{K}^{-1}$	4.55
$\sigma, \text{Wm}^{-2} \text{K}^{-4}$	5.67×10^{-8}	ρ_p, kgm^{-3}	1007	$A_{\text{out}}, \text{m}^2$	0.2
λ_a	0.028	$C_g, \text{Jkg}^{-1} \text{K}^{-1}$	837	$A_{\text{in}}, \text{m}^2$	0.2
δ_a, m	0.3	$C_w, \text{Jkg}^{-1} \text{K}^{-1}$	880	$\nu_m, \text{m}^2 \text{s}^{-1}$	17.5×10^{-6}
$\Delta w_1, \text{m}$	0.3	V_g, m^3	0.012	Pr	0.7
$\Delta w_2, \text{m}$	0.03	V_w, m^3	0.003	C	0.57

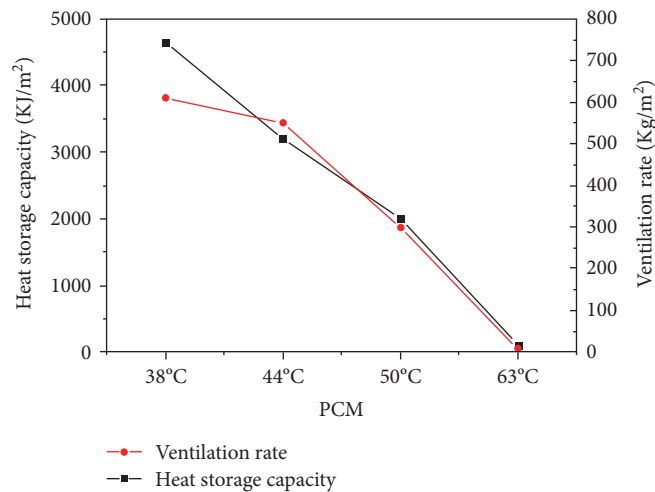


FIGURE 3: Thermal storage capacity and air flow rate for four different PCMs.

difference between inlet and outlet. Higher phase change temperature leads to poor chargeability of the chimney and has the shorter ventilation time. The ventilation times corresponding to different PCMs are shown in Table 3.

As shown in Table 3, when the phase change temperature of the PCM is 38°C, the longest ventilation time of 12 hours was achieved while the PCM with phase change temperature of 50°C has the shortest ventilation time which is only 4.33 hours. This is because more solar energy was stored in the PCM with lower phase change temperature.

Figures 8 and 9 show the energy storage and release of different components of chimney combined with the dodecyclic acid (phase change temperature of 44°C) during the day and night, respectively.

It can be seen from Figure 8 that the available solar energy Q_s is as high as 11,000 kJ/m², while the energy stored in PCM Q_x is only 3150 kJ/m², which accounts for 28.6% of the Q_s . The heat transferred by radiation from glass cover to ambient Q_{g-amb} is 5090 kJ/m² that accounts for 46.3% of Q_s . It means that nearly 50% of the solar energy is lost through glass cover to ambient during the daytime period. The solar energy utility efficiency is still low for PCM of dodecyclic acid.

It can be seen from Figure 9 that most of energy stored in PCM is transferred to absorber surface, Q_{p-w} accounts for

89% of Q_x . However, 80% of Q_{p-w} loses to ambient through glass cover during night ventilation. The heat absorbed by air Q_a is only about 13% of Q_x . This means that most of heat stored in PCM is lost to ambient through glass cover by radiation during the night ventilation; only a small portion is used for heating the air within air channel.

4. Validation of the Numerical Model

The numerical model is validated by comparing numerical predictions of PCM temperature and air mass flow rate with the experimental results obtained from Liu and Li's study [28]. This experiment investigated the thermal performance of a solar chimney integrated with PCM for a given heat flux. The PCM temperature during charging and discharging processes and air flow rate were investigated. As shown in Figure 10, a rectangular PCM container with dimensions of 1000 mm wide \times 1600 mm high \times 40 mm deep was constructed of stainless steel. A total of 50 kg RT42 was used to fill the container, and the physical properties of RT42 was given in [28]. In their experimental testing, the openings of inlet and outlet were closed during the charging period. The discharging period happened right after the charging period. A number of K-type thermocouples with the measurement range of -50 to

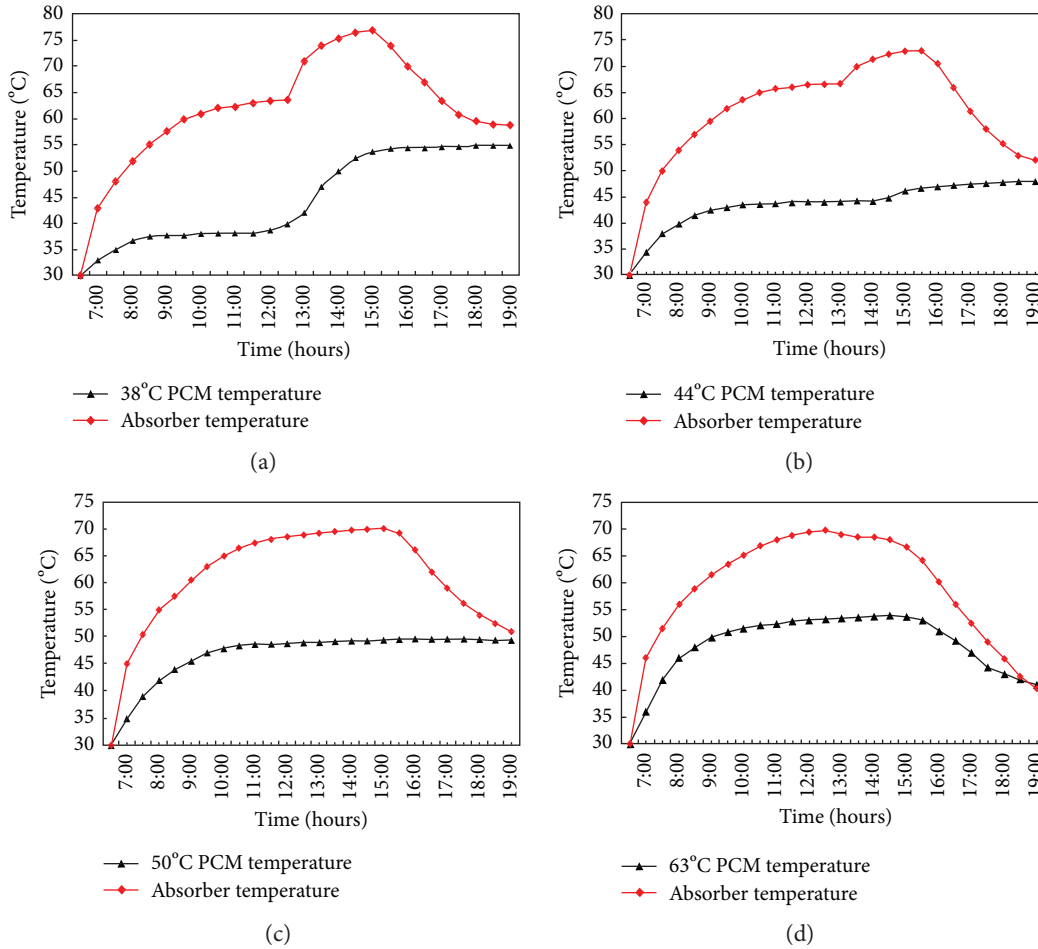


FIGURE 4: Absorber temperature and PCM temperature for four different PCMs when storing heat during the day.

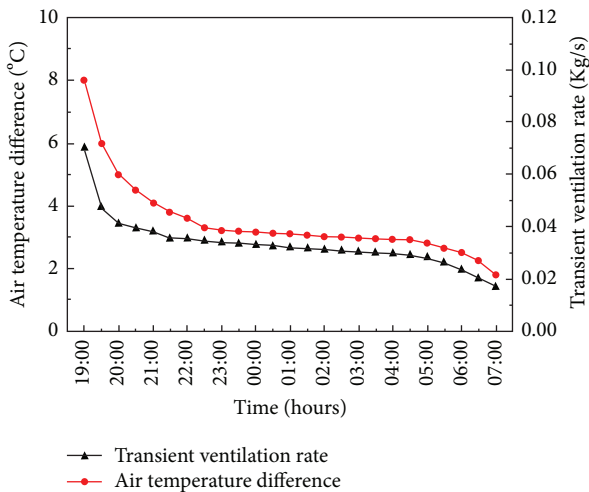


FIGURE 5: Variation of air temperature and ventilation rate for phase change temperature of 38°C.

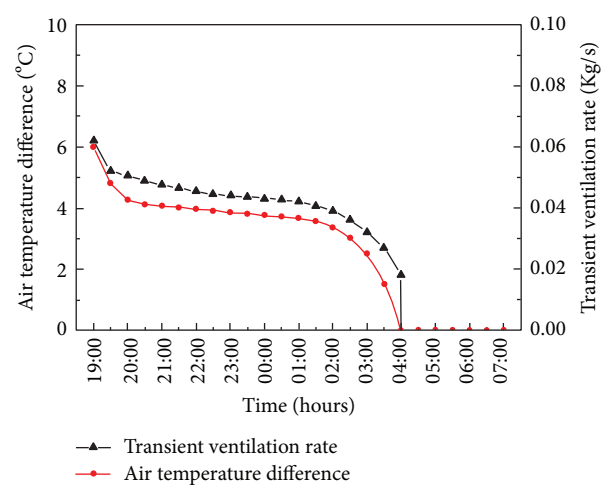


FIGURE 6: Variation of air temperature and ventilation rate for phase change temperature of 44°C.

250°C and accuracy of $\pm 0.3^\circ\text{C}$ were distributed on the glass cover, absorber plate, inside the PCM, and the air channel. Air velocities inside the air channel are measured by a TSI8455 air flow probe with the measurement

range of 0–50 m/s and accuracy of $\pm 3\%$ of reading. The setup of the developed model in this study follows the experimental conditions. Figure 11(a) shows the PCM temperatures obtained by numerical simulation and experiment testing. It can be seen that there was a good

TABLE 3: Ventilation times corresponding to different PCMs.

Type	Phase change temperature (°C)	Time period	Total time (hour)
The myristoyl	38	19:00–7:00	12
The dodecylic acid	44	19:00–4:00	9
The myristelaidic acid	50	19:00–23:20	4.33

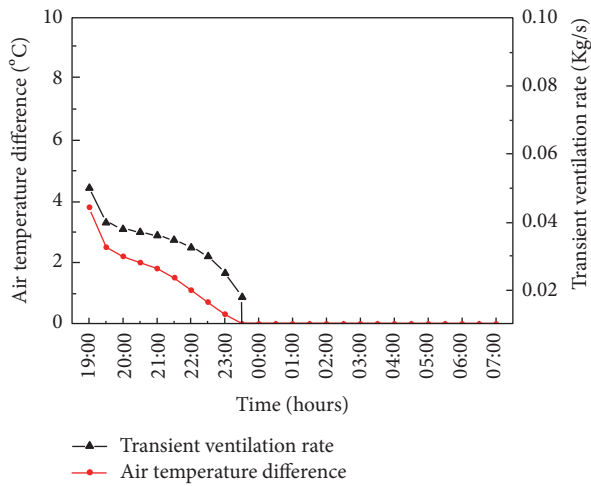


FIGURE 7: Variation of air temperature and ventilation rate for phase change temperature of 50°C.

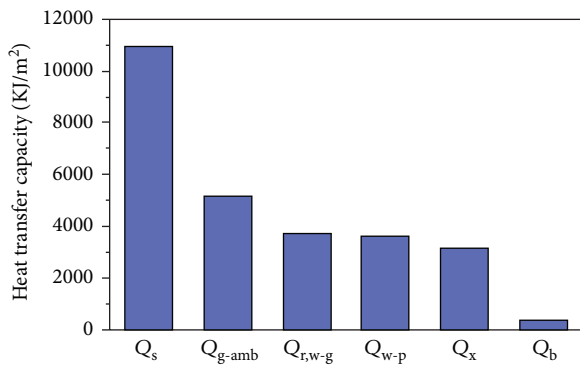


FIGURE 8: Heat transfer between different components of chimney during the day.

agreement between the numerical data and experimental data. The coherence indicates the validity of the developed numerical model. Figure 11(b) shows that the predicted air flow rate varies with the measured one within a small divergence. Therefore, it has the capability to predict the mass flow rate accurately.

5. Conclusions

In this present paper, a numerical model is developed for optimizing the phase change temperature for a PCM-based

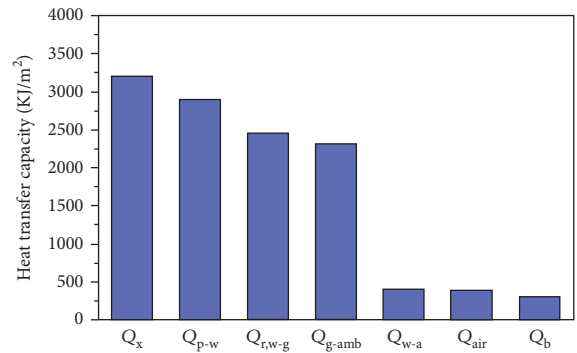


FIGURE 9: Heat transfer between the different components of chimney during the nighttime.

solar chimney by considering the amount of energy stored in PCM and ventilation rate. Based on the numerical results, the following conclusions can be made:

- (1) The higher the phase change temperature, the lower the energy storage and ventilation rate per unit area of absorber. In this study, the PCM with phase change temperature of 38°C has the best performance among the studied PCMs while the PCM with phase change temperature of 63°C has the poorest performance. Specifically, for the PCM with phase change temperature of 38°C, the solar chimney achieves the maximum energy storage of 4750 kJ/m² and the maximum ventilation rate of 610 kg/m². However, for PCM with phase change temperature of 63°C, there is little energy stored in PCM and the ventilation does not occur during the scheduled ventilation time.
- (2) A lower phase change temperature can increase the chargeability and dischargeability of the solar chimney. The larger amount of energy stored and discharged by the solar chimney and consequently a higher ventilation rate is achieved. A higher phase change temperature demands higher solar radiation intensity and longer charging time, and results in poor chargeability of the chimney.
- (3) During daytime, the energy stored in PCM with phase change temperature of 44°C, Q_x only accounts for 28.6% of the available solar energy, while nearly 50% of the solar energy is lost through glass cover to ambient by radiation during daytime period. The solar energy utility efficiency is low.
- (4) During night ventilation period, the heat absorbed by air Q_a is only about 13% of Q_x . This means that most of the heat stored in PCM is lost to ambient through glass cover by radiation; only a small portion is used for heating the air within air channel.
- (5) It can be concluded that most of the stored energy is lost through glass cover to ambient by radiant heat transfer. Therefore, reducing the radiation heat transfer coefficient of glass cover can increase the night ventilation effectively.

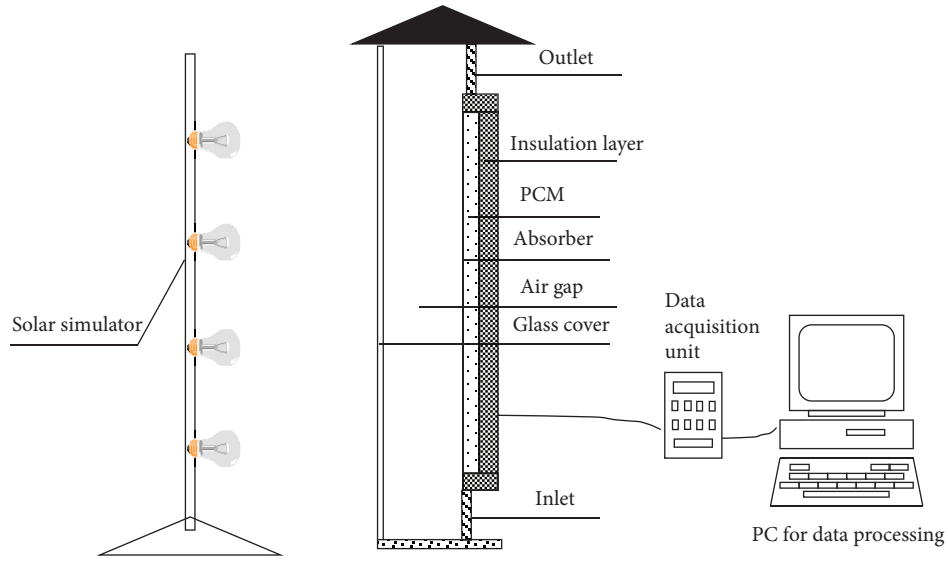


FIGURE 10: The schematic diagram of the experimental solar chimney.

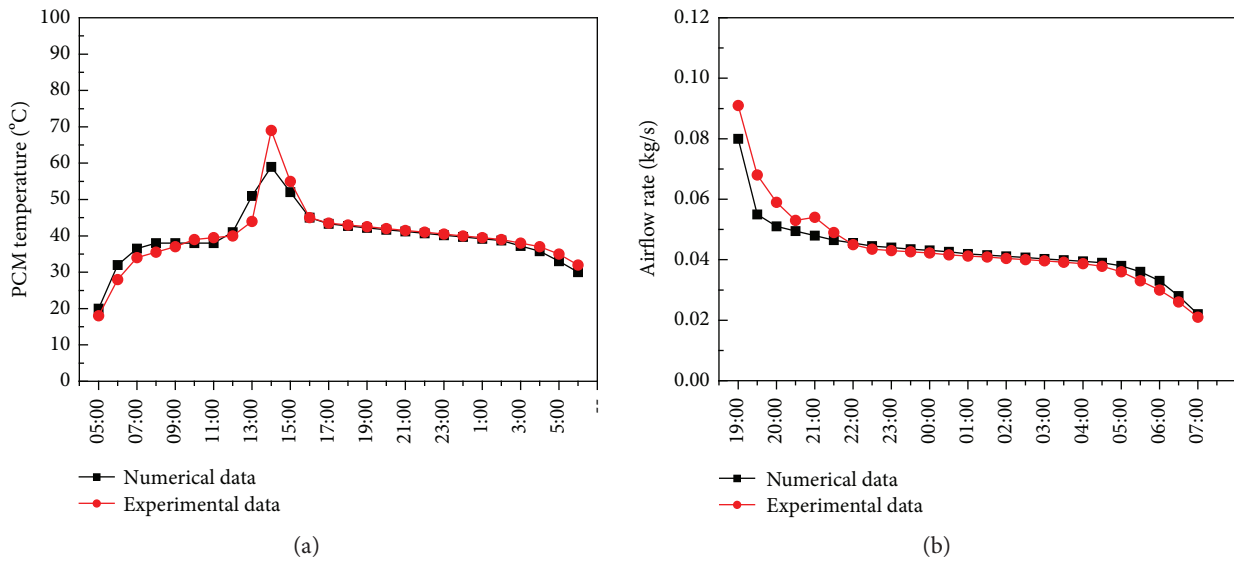


FIGURE 11: Comparison of numerical and experimental results: (a) absorber temperature and (b) airflow rate.

Nomenclature

A :	Surface area (m^2)
$A_{\text{in}}, A_{\text{out}}$:	Cross sectional area of inlet and outlet (m^2)
A_r :	Aspect ratio of $A_{\text{in}}/A_{\text{out}}$
C_d :	Coefficient of discharge of air channel inlet
C :	Specific heat ($\text{J}\cdot\text{kg}^{-1}\text{K}^{-1}$)
h :	Convective heat transfer coefficient
K_{w1} :	Thermal conductivity of brick wall ($\text{W}\cdot\text{m}^{-1}\text{K}^{-1}$)
K_{w2} :	Thermal conductivity of extruded insulation panels ($\text{W}\cdot\text{m}^{-1}\text{K}^{-1}$)
L :	Length (m)
m :	Mass flow rate ($\text{kg}\cdot\text{s}^{-1}$)
Q :	Total heat (kJ)

q :	Heat transfer (W)
q_s :	Solar radiation intensity ($\text{W}\cdot\text{m}^{-2}$)
T :	Temperature (K)
U_b :	Overall heat transfer coefficient from PCM to indoor ($\text{W}\cdot\text{m}^{-2}\text{K}^{-1}$)
U_t :	Overall heat transfer coefficient from glass cover to ambient ($\text{W}\cdot\text{m}^{-2}\text{K}^{-1}$)
V :	Volume (m^3)
v :	Velocity ($\text{m}\cdot\text{s}^{-1}$)

Greek Symbols

Δw_1 :	Thickness of brick wall
Δw_2 :	Thickness of extruded insulation panels

Δt :	Temperature difference (K)
α :	Absorptivity
ρ :	Density ($\text{kg}\cdot\text{m}^{-3}$)
g :	Gravitational acceleration ($\text{m}\cdot\text{s}^{-2}$)
σ :	Stefan-Boltzmann constant
ε :	Emissivity
β :	Inclination angle measured from the horizontal plane
δ_a :	Gap between absorber wall and glass
γ :	Constant for mean temperature approximation
λ :	Thermal conductivity ($\text{W}\cdot\text{m}^{-1}\text{K}^{-1}$)
τ :	Glass transmittance
ν :	Kinematic viscosity ($\text{m}^2\cdot\text{s}^{-1}$)
ζ :	Emissivity.

Subscripts

amb:	Ambient conditions
a:	Air in the air flow channel
a-g:	From air to glass
b:	From PCM to indoor
c:	Chimney
cv,w-a:	Convective from black wall to air
cv,a-g:	Convective from air to glass
in:	Inlet
out:	Outlet
g:	Glass
g-sky:	From glass to sky
i:	From PCM to indoor
p:	PCM
p-w:	From PCM to black wall
r:	Room
r,g-sky:	Radiative from glass to sky
r,w-g:	Radiative from black wall to glass
s:	Sky
t:	Air flow channel of the solar roof
w:	Absorber wall
w-a:	From absorber wall to air
w-g:	From absorber wall to the glass
w-p:	From absorber wall to PCM
x:	Storage capacity of the PCM.

Dimensionless Terms

Nu:	Nusselt number
Pr:	Prandtl number
Ra:	Rayleigh number
Gr:	Grashof number.

Conflicts of Interest

The authors declare no conflict of interests regarding the publication of this paper.

Acknowledgments

The authors gratefully acknowledge the support from the National Science Foundation of China (no. 51478058), the 111 Project (no. B13041), and the Fundamental Research Funds for the Central Universities (no. 106112015CDJXY210006).

References

- [1] J. DeBlois, M. Bilec, and L. Schaefer, "Simulating home cooling load reductions for a novel opaque roof solar chimney configuration," *Applied Energy*, vol. 112, no. 4, pp. 142–151, 2013.
- [2] M. Maerefat and A. P. Haghighi, "Natural cooling of stand-alone houses using solar chimney and evaporative cooling cavity," *Renewable Energy*, vol. 35, no. 9, pp. 2040–2052, 2010.
- [3] W. P. Puangsombut, J. Hirunlabh, J. Khedari, B. Zeghamati, and M. M. Win, "Enhancement of natural ventilation rate and attic heat gain reduction of roof solar collector using radiant barrier," *Building and Environment*, vol. 42, no. 6, pp. 2218–2226, 2007.
- [4] L. Susanti, H. Homma, and H. Matsumoto, "A naturally ventilated cavity roof as potential benefits for improving thermal environment and cooling load of a factory building," *Energy and Buildings*, vol. 43, no. 1, pp. 211–218, 2011.
- [5] J. DeBlois, M. Bilec, and L. Schaefer, "Simulating home cooling load reductions for a novel opaque roof solar chimney configuration," *Applied Energy*, vol. 112, no. 12, pp. 142–151, 2013.
- [6] H. W. Jing, Z. D. Chen, and A. G. Li, "Experimental study of the prediction of the ventilation flow rate through solar chimney with large gap-to-height ratios," *Building and Environment*, vol. 89, pp. 150–159, 2015.
- [7] A. Y. K. Tan and N. H. Wong, "Natural ventilation performance of classroom with solar chimney system," *Energy and Buildings*, vol. 53, no. 53, pp. 19–27, 2012.
- [8] D. S. Lee, T. C. Hung, J. R. Lin, and J. Zhao, "Experimental investigations on solar chimney for optimal heat collection to be utilized in organic Rankine cycle," *Applied Energy*, vol. 154, no. 53, pp. 651–662, 2015.
- [9] R. Bassiouny and N. S. A. Korah, "Effect of solar chimney inclination angle on space flow pattern and ventilation rate," *Energy and Buildings*, vol. 41, no. 2, pp. 190–196, 2009.
- [10] H. H. Al-Kayiem, K. V. Sreejaya, and S. I. U. H. Gilani, "Mathematical analysis of the influence of the chimney height and collector area on the performance of a roof top solar chimney," *Energy and Buildings*, vol. 68, no. 1, pp. 305–311, 2014.
- [11] J. Khedari, B. Boonsri, and J. Hirunlabh, "Ventilation impact of a solar chimney on indoor temperature fluctuation and air change in a school building," *Energy and Buildings*, vol. 32, no. 1, pp. 89–93, 2000.
- [12] J. Hirunlabh, S. Wachirapuwadon, N. Pratinthong, and J. Khedari, "New configurations of a roof solar collector maximizing natural ventilation," *Building and Environment*, vol. 36, no. 3, pp. 383–391, 2001.
- [13] S. Chungloo and B. Limmeechokchai, "Application of passive cooling systems in the hot and humid climate: the case study of solar chimney and wetted roof in Thailand," *Building and Environment*, vol. 42, no. 9, pp. 3341–3351, 2007.
- [14] T. Miyazaki, A. Akisawa, and T. Kashiwagi, "The effects of solar chimneys on thermal load mitigation of office buildings under the Japanese climate," *Renewable Energy*, vol. 31, no. 7, pp. 987–1010, 2006.
- [15] A. A. Imran, J. M. Jalil, and S. T. Ahmed, "Induced flow for ventilation and cooling by a solar chimney," *Renewable Energy*, vol. 78, no. 12, pp. 236–244, 2015.
- [16] N. Saifi, N. Settou, B. Dokkar, B. Negrou, and N. Chennouf, "Experimental study and simulation of airflow in solar chimneys," *Energy Procedia*, vol. 18, no. 4, pp. 1289–1298, 2012.

- [17] J. Arce, M. J. Jimenez, J. D. Guaman, M. R. Heras, G. Alvarez, and J. Xaman, "Experimental study for natural ventilation on a solar chimney," *Renewable Energy*, vol. 34, no. 12, pp. 2928–2934, 2009.
- [18] K. E. Amori and S. W. Mohammed, "Experimental and numerical studies of solar chimney for natural ventilation in Iraq," *Energy and Buildings*, vol. 47, no. 4, pp. 450–457, 2012.
- [19] S. Liu and Y. Li, "An experimental study on the thermal performance of a solar chimney without and with PCM," *Renewable Energy*, vol. 81, pp. 338–346, 2015.
- [20] G. Zhou and M. Pang, "Experimental investigations on the performance of a collector–storage wall system using phase change materials," *Energy Conversion and Management*, vol. 105, pp. 178–188, 2015.
- [21] K. S. Ong, "A mathematical model of a solar chimney," *Renewable Energy*, vol. 28, no. 7, pp. 1047–1060, 2003.
- [22] K. S. Ong and C. C. Chow, "Performance of a solar chimney," *Solar Energy*, vol. 74, no. 1, pp. 1–17, 2003.
- [23] A. P. Haghighi and M. Maerefat, "Solar ventilation and heating of buildings in sunny winter days using solar chimney," *Sustainable Cities & Society*, vol. 10, pp. 72–79, 2014.
- [24] R. Bassiouny and N. S. A. Koura, "An analytical and numerical study of solar chimney use for room natural ventilation," *Energy and Buildings*, vol. 40, no. 5, pp. 865–873, 2008.
- [25] N. K. Bansal, J. Mathur, S. Mathur, and M. Jain, "Modeling of window-sized solar chimneys for ventilation," *Building and Environment*, vol. 40, no. 10, pp. 1302–1308, 2005.
- [26] R. Bassiouny and N. S. A. Korah, "Effect of solar chimney inclination angle on space flow pattern and ventilation rate," *Energy and Buildings*, vol. 41, no. 2, pp. 190–196, 2009.
- [27] China Meteorological Administration, Tsinghua University, *Weather Data for Built Environment Thermal Analysis of China*, China Architecture & Building Press, Beijing, 2005.
- [28] Y. Li and S. Liu, "Experimental study on thermal performance of a solar chimney combined with PCM," *Applied Energy*, vol. 114, pp. 172–178, 2014.

Research Article

Detailed Modeling of Flat Plate Solar Collector with Vacuum Glazing

Viacheslav Shemelin¹ and Tomas Matuska²

¹Faculty of Mechanical Engineering, Czech Technical University in Prague, Technicka 4, 166 07 Prague 6, Czech Republic

²University Centre for Energy Efficient Buildings, Czech Technical University in Prague, Trinecka 1024, 273 43 Buzehrad, Czech Republic

Correspondence should be addressed to Viacheslav Shemelin; viacheslav.shemelin@cvut.cz

Received 10 February 2017; Accepted 6 April 2017; Published 1 June 2017

Academic Editor: Stoian Petrescu

Copyright © 2017 Viacheslav Shemelin and Tomas Matuska. This is an open access article distributed under the Creative Commons Attribution License, which permits unrestricted use, distribution, and reproduction in any medium, provided the original work is properly cited.

A theoretical analysis of flat plate solar collectors with a vacuum glazing is presented. Different configurations of the collector have been investigated by a detailed theoretical model based on a combined external and internal energy balance of the absorber. Performance characteristics for vacuum flat plate collector alternatives have been derived. Subsequently, annual energy gains have been evaluated for a selected variant and compared with state-of-the-art vacuum tube collectors. The results of modeling indicate that, in the case of using advanced vacuum glazing with optimized low-emissivity coating (emissivity 0.20, solar transmittance 0.85), it is possible to achieve efficiency parameters similar to or even better than vacuum tube collectors. The design presented in this paper can be considered promising for the extension of the applicability range of FPC and could be used in applications, which require low-to-medium temperature level.

1. Introduction

The thermal use of solar energy for the production of heat from sunlight is one of the oldest energy transformation methods. This technology has been known and—sometimes even unconsciously—used for ages. It has been rediscovered and used again over the last 45 years. Today, it is ready for application, but after this short growth time, there is a large potential for development in this field, especially in the field of solar collectors.

As of now, the most widely used solar collector type in Europe is a solar flat plate collector (FPC). Simple structure, high optical efficiency, low cost, and safe operation are its main features. However, FPC is generally designed for a low temperature level between 40°C and 60°C, which is mostly the case for the domestic hot water system. Any shifts to a higher temperature level could bring the extension of the applicability range of FPC. Hence, efforts aimed to improve the performance of flat plate solar collectors are ongoing. The performance of a flat plate solar collector is largely influenced by the thermal losses from the absorber to the ambient

via the transparent cover. One way to reduce this heat loss is to reduce the natural convection heat transfer in the space between the absorber and the cover by its partitioning with the use of additional glass pane, plastic film, or transparent insulation materials (TIM). Another way to reduce this heat loss is to use gas with lower thermal conductivity rather than air or by evacuating the space.

Veinberg BP and Veinberg VB [1] investigated the use of “deep narrow meshes” as solar transparent honeycomb insulation. Further, Hollands [2] presented the theoretical performance characteristics of a cellular honeycomb as a convection suppression device placed between the absorber and the outer glass cover of the FPC. Tabor [3] presented a brief picture of the cellular honeycomb construction, indicating that a successful use of honeycomb insulation requires a material with better physical properties and manufacturing techniques. Later, Rommel and Wagner [4] demonstrated that FPC containing 50–100 mm polycarbonate honeycomb layers functions well with a fluid working temperature between 40 and 80°C. Kessentini et al. [5] presented a FPC with plastic transparent insulation and low-cost overheating protection

system destined for heat supply from 80 to 120°C. Hitting higher working temperatures up to 260°C is also possible using glass honeycombs since plastic covers are susceptible to melting at temperatures above 120°C. Svendsen and Jensen [6] and Svendsen [7] experimentally showed that solar FPC efficiency can be significantly improved by filling the air gap between the absorber and the cover with a monolithic silica aerogel and evacuating to 10 kPa. Duan [8] studied the reduction of front side heat loss by placing the aerogel layer between the transparent cover and the absorber plate showing an increase of 21% in the collector efficiency respecting to the conventional collector. These studies have demonstrated that convective heat losses are significantly reduced by the use of TIM due to the partition of the space between the absorber and the cover-restricting heat transport by convection and thus, a higher performance of FPC was achieved. The test results were encouraging, and a performance comparable to that of evacuated tube collectors was obtained.

Yet, most of the available transparent insulation materials are still not a good choice for high-temperature flat plate collectors. They either cannot withstand high temperature levels because they are made of plastics (mostly honeycomb and capillary materials), they are hygroscopic and cannot withstand the humidity inside the collector (aerogels and so forth), or they are very expensive (glass capillaries).

The use of a moderate vacuum in flat plate collectors is known to reduce top heat losses since the work of Eaton and Blum [9]. The concept of an evacuated flat plate collector was commercially realized and is available on the market. Apart from the higher thermal output, these collectors have the advantage of longer lifetime compared to nonevacuated collectors, because no humidity and condensation problems occur within the casing. Typical interior pressures, which can be maintained economically, lie between 1 and 10 kPa. It means that although convection losses are suppressed, gas heat conduction remains fully developed. Further, Benz and Beikircher [10] constructed a prototype collector based on the commercially available flat plate collector. To implement high thermal efficiency in the medium temperature range, the thermal losses of the absorber have been reduced using a low emissive selective absorber, a low pressure krypton filling (5 kPa) in the collector casing. The prototype collector has been dynamically tested and has showed very high efficiencies of more than 60% at 100°C. Later, Benvenuti [11] presented a FPC, which is able to reach 300°C. That has become possible by ultrahigh vacuum (1.33×10^{-7} Pa) maintained by a getter pump powered by the sun. As for the latest studies, Moss and Shire [12] indicate an improvement from 25% for a conventional FPC to 60–65% for vacuum FPC when operating at 140°C above ambient temperatures. More recently, Shire et al. [13] highlight that vacuum FPC collector could provide heat up to 200°C with efficiency greater than 50%.

This paper presents the idea of replacing single glazing, which is used in most of the flat plate solar collectors, with flat vacuum glazing, which, on the one hand, will show a low level of heat losses (low-emissivity coating, high vacuum) and, on the other hand, will demonstrate a high solar energy transmittance. Flat plate solar collectors with low heat loss (at the level of vacuum tube collectors) and with a sufficiently

high optical efficiency could be effectively used for integration into building envelopes (residential, industrial), which are widely available.

2. Vacuum Glazing as a Glazing Cover of Solar Collector

Vacuum glazing consists of two glass sheets sealed together around the periphery. Glass sheets are supported by a pillar array arranged on a regular square grid pattern, and the space between the sheets is evacuated to a pressure lower than 0.1 Pa, thus effectively eliminating both gaseous conduction and convection. Maintaining the pressure below 0.1 Pa for a prospected service life period of 30 years represents a significant engineering challenge. Fang et al. [14] carried out extreme thermal cycling tests. It was found that the heat conductance at the center region had increased by 10% from which the vacuum pressure within the evacuated space was determined to have increased from the negligible level of less than 0.1 Pa to 0.16 Pa. Later, Koebel et al. [15] investigated the possible sources for pressure increase and concluded that, under consideration for the ideal process conditions, it should be possible to keep the total pressure below 0.1 Pa after 30 years. It is essential to avoid any kind of leaking or microcracking because the quality of the vacuum is directly linked to the thermal insulation performance.

Three different heat transfer mechanisms contribute to the total heat transfer coefficient h_{g1-g2} of the glazing: thermal conduction through a residual gas, thermal conduction through spacers, and radiation heat transfer between the two sheets in vacuum glazing. The total heat transfer coefficient h_{g1-g2} between the glass sheets of a vacuum glazing can be approximated by the simple addition of individual heat transfer coefficients as [16, 17]

$$h_{g1-g2} = 0.8P + 4\varepsilon_{\text{eff}}\sigma T_{\text{mean}}^3 + \frac{2\lambda r}{d^2}, \quad (1)$$

where P is internal pressure, σ is the Stefan-Boltzmann constant ($5.67 \times 10^{-8} \text{ W/m}^2\cdot\text{K}^4$), T_{mean} is the average of temperatures T_1 and T_2 of the glass sheets, λ is the thermal conductivity of glass pillars, r is the radius of glass pillars, d is the distance between the pillars, and the effective emittance, ε_{eff} , is conventionally written as follows:

$$\varepsilon_{\text{eff}} = \frac{1}{(1/\varepsilon_1) + (1/\varepsilon_2) - 1}. \quad (2)$$

Equation (1) is valid for the space with pressure less than 0.1 Pa, that is, high vacuum.

Vacuum glazing already appears in the portfolio of the window suppliers for use in buildings (see Figure 1). Commercially available vacuum glazing with configuration 3-0.2-3 mm has a transmittance of solar radiation of $\tau = 62\%$ and glazing center-of-glazing transmittance U value of $1.1 \text{ W/m}^2\cdot\text{K}$. The vacuum provides a high level of thermal insulation which reduces heat loss by conduction and convection. However, heat loss can still occur due to radiation.

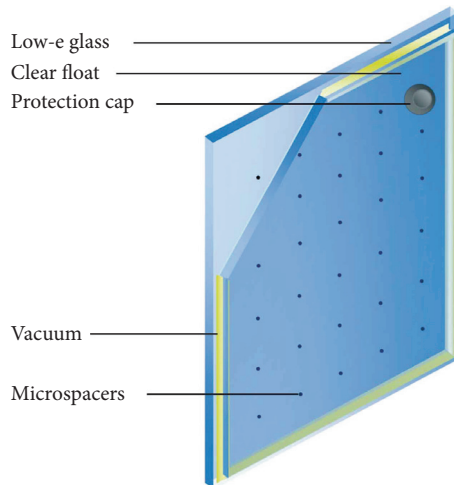


FIGURE 1: Vacuum glazing (Pilkington Spacia).

Using low-e coating on the outer surface of the inner glass pane minimizes radiative heat losses.

State-of-the-art low-e coatings have been almost exclusively developed for architecture. To uphold the thermal and visual comfort in buildings, coating systems based on silver are primarily used, which can provide for extremely low emissivity (less than 0.03) and high visible transmittance (up to 0.90). Solar transmittance (within the whole solar spectrum range), however, is rarely higher than 0.60. A low solar energy transmittance, caused by the reflectance of low-emissivity coating for the near-infrared radiation (NIR) in the solar spectrum, is unsuitable for use in solar collectors. However, values up to 0.80 and the corresponding higher emissivity (between 0.15 and 0.20) can be achieved by using very thin silver layers, which have been developed in the last years for triple glazing, or with metal oxides (Figure 2) [18]. It is also possible to use the external glass antireflection coatings on both surfaces and thus reduce reflection at the two air-glass boundary surfaces.

To evaluate the potential of vacuum glazing application in solar thermal collector design, detailed simulations for three different variants of the collector cover glazing have been carried out. Reference variant (REF) is a simple solar low iron glass. The second variant (VG1) has a vacuum glazing based on two low iron glass without any coating. The last variant (VG2) is an advanced vacuum glazing with a low-emissivity coating on the outer surface of the inner glass (position 3). The optical properties of the coating are IR emissivity of 0.2 and solar transmittance of 0.85. Configurations of considered collector glazings are shown graphically in Figure 3. The parameters of the cover glazings used for the comparative study are listed in Table 1.

3. Theoretical Model of Solar Flat Plate Collector

3.1. Description of the Model. In order to analyze the thermal performance of FPC with considered variants of the transparent cover, a detailed theoretical model of the flat plate collector has been used. The detailed model originated from design tool KOLEKTOR 2.0 [19] originally developed as the Visual Basic program.

To compare the performance of given glazings, the flat plate collector has been considered to be consisting of an absorber placed in the insulated box covered with a given transparent cover. There is an air gap between the absorber and the cover and between the absorber and its back insulation, both defined by thickness and slope. The absorber is designed as a harp with distribution and riser pipes (defined by length, distance, and diameter). The transparent cover is considered with temperature-dependent thermal conductance according to the equation

$$h_{g1-g2} = h_{g0} + h_{g1}T_{g1-g2} + h_{g2}T_{g1-g2}^2, \quad (3)$$

where h_{g0} , h_{g1} , and h_{g2} are coefficients for given cover structures and T_{g1-g2} (°C) is mean glazing temperature. Thermal insulation layers are considered in a similar way as temperature dependent.

The detailed model of flat plate solar collector allows conducting a detailed calculation of heat transfer in the solar collector. Energy flow from the absorber surface to ambient and from the absorber surface to a heat transfer liquid, together with a temperature distribution in the collector, are calculated in the iteration loops. A solar collector can be specified by a number of detailed parameters, optical properties of glazing and absorber, and thermophysical properties of the main components of a solar collector (frame, absorber, and transparent cover) in the model.

3.2. Basic Equations. The mathematical model for solar flat plate liquid collector solves one-dimensional heat transfer balances. Hottel and Woertz [20], Hottel and Whillier [21], and Bliss [22] developed the simplest assumptions: thermal capacities are neglected and a single value of collector overall heat loss coefficient is considered. Based on these assumptions and considering that the heat transfer is mainly one-dimensional and predominant in the direction normal to the absorber, Duffie and Beckman [23] developed a simplified model (with the electrical analogy) to characterize the solar collector in steady-state conditions. The model solves the energy balance of the solar collector under steady-state conditions according to the principle Hottel-Whillier equation for usable thermal output:

$$\dot{Q}_u = A_{\text{abs}} F_R [(\tau\alpha)_n G_t - U(T_{\text{in}} - T_{\text{amb}})]. \quad (4)$$

In this equation, A_{abs} is the absorber area, F_R is the collector heat removal factor, τ is the solar transmittance of the collector cover, α is the solar absorptance of the absorber, G_t is the total solar irradiance, U is the overall heat loss coefficient of collector, T_{in} is the inlet fluid temperature, and T_{amb} is the ambient temperature.

The main planes of the collector are cover exterior surface (f_2), cover interior surface (f_1), absorber (abs), back insulation interior surface (b_1), back frame exterior surface (b_2), edge insulation interior surface (e_1), and edge frame exterior surface (e_2). A surface temperature is determined for each plane of collector during the calculation procedure. The main collector planes are schematically outlined in Figure 4.

The mathematical model in general consists of two parts: external energy balance of absorber (heat transfer from

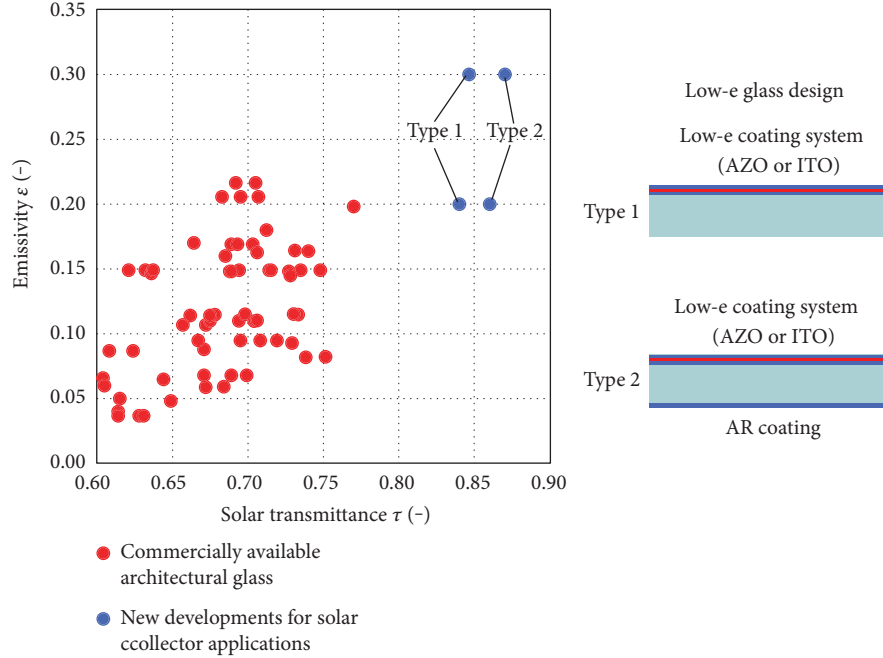


FIGURE 2: Optical properties of spectrally selective glass with high solar transmittance for architecture and solar collector applications [18].

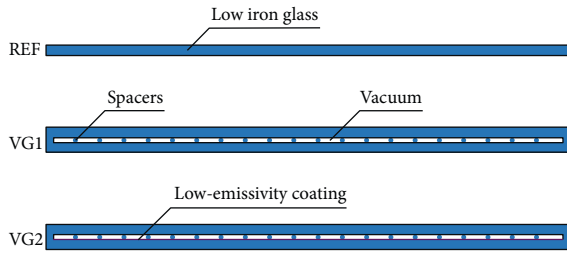


FIGURE 3: Configurations of the investigated cover glazings.

TABLE 1: Comparison of cover glazing physical properties.

Properties	REF	VG1	VG2
Thickness of layers (mm)	4	4-0.2-4	4-0.2-4
Emissivity of surfaces (-)	0.85/ 0.85	0.85/0.85/ 0.85/0.85	0.85/0.85/ 0.2/0.85
Solar transmittance (-)	0.92	0.85	0.79
Thermal conductance at 20°C (W/m ² ·K)	274.39	4.68	1.62

absorber surface to ambient environment) and internal energy balance of absorber (heat transfer from absorber surface into heat transfer fluid). Both external and internal energy balances are mutually dependent. The overall collector heat loss coefficient U as the main output from external balance is one of the inputs for internal balance. On the other side, mean absorber temperature T_{abs} as one of the outputs from internal balance is used as a necessary input for external balance. Iteration loop has been introduced to transfer the results from external balance to starting internal balance

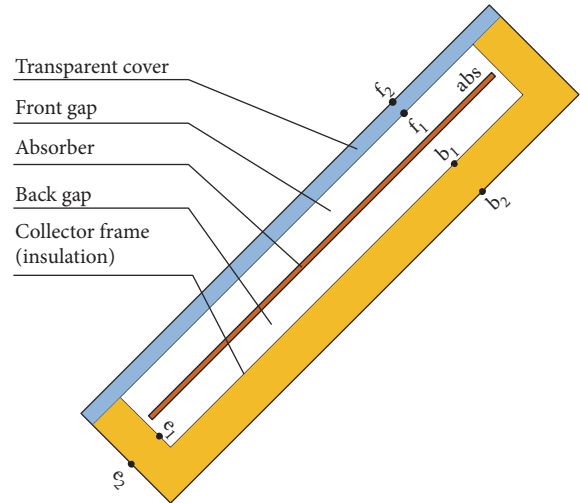


FIGURE 4: The main collector planes (surfaces) in a solar collector model.

and the results from internal balance are put to external balance. Loop iterates as long as the difference between absorber temperatures calculated in two adjacent iteration steps is higher than the required minimum (see Figure 5).

3.3. *Experimental Validation.* The model has been experimentally validated in the frame of solar collectors testing according to the European standard EN ISO 9806 in the accredited Solar Laboratory operated under the University Centre for Energy Efficient Buildings, Czech Technical University in Prague. Solar thermal collectors have been tested to obtain steady-state thermal output at constant operation

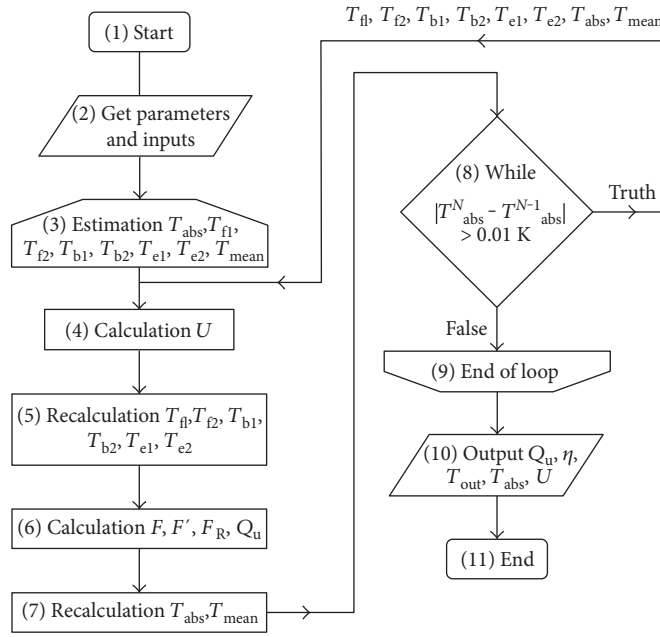


FIGURE 5: Flow chart of the iteration loop.

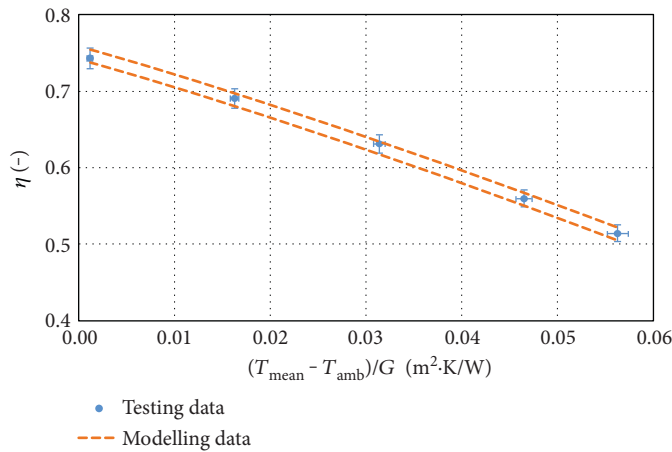


FIGURE 6: Mathematical model validation.

conditions of inlet temperature (± 0.05 K) and mass flow rate ($\pm 0.002\%$) of heat transfer fluid (water) entering collector and at constant climatic conditions of solar irradiation ($\pm 1.4\%$) and ambient temperature (± 0.05 K).

Instantaneous efficiency has been calculated from collector thermal output related to total solar irradiation input (incident on collector reference area: gross area). Experimental data points of solar collector efficiency are coupled with uniform uncertainty bars in the graphs. Expanded uncertainty of efficiency and reduced temperature difference have been assessed for experimental data from both type A (statistical) and type B (instrumental) uncertainties considering the coverage factor $k=2$ with 95% level of confidence (normal distribution).

The theoretical calculation of efficiency characteristic by the model is subjected to the uncertainty of real collector

parameters which are used as inputs for the model. While geometrical parameters are easily available with high degree of confidence, the number of parameters defining the properties of collector parts is found uncertain within narrow range (e.g., absorber and glazing optical parameters, mostly $\pm 2\%$), middle range (e.g., conductivity of insulation layer dependent on its temperature and density, $\pm 10\%$), and quite broad range (e.g., emittance of absorber back side and emittance of insulation layer or collector frame, $>10\%$). Therefore, the results of theoretical calculation could be presented as two delimiting curves where the collector efficiency values can be found in reality.

The mathematical model has been validated in the field of atmospheric solar flat plate collectors (top quality solar collectors with state-of-the-art copper laser-welded absorber coated with a high-performance selective coating and solar

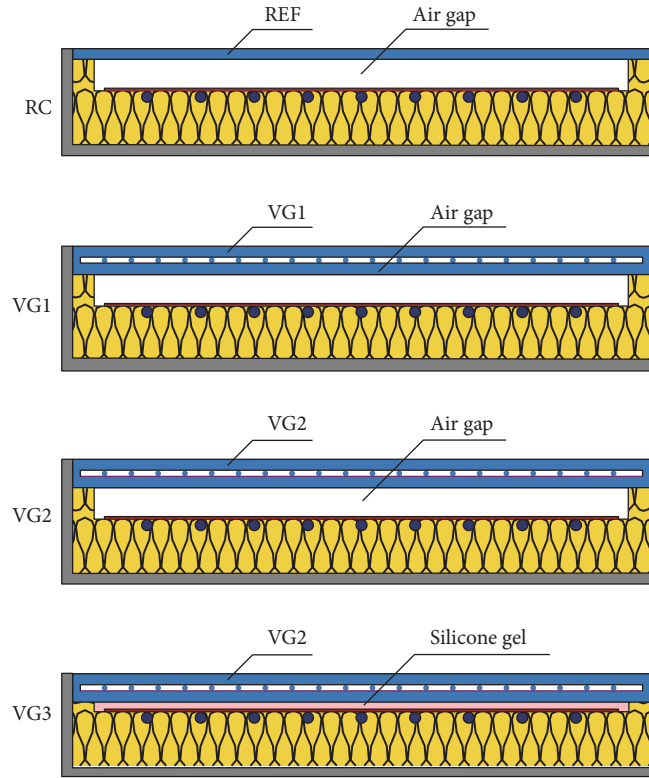


FIGURE 7: Considered solar collector configurations.

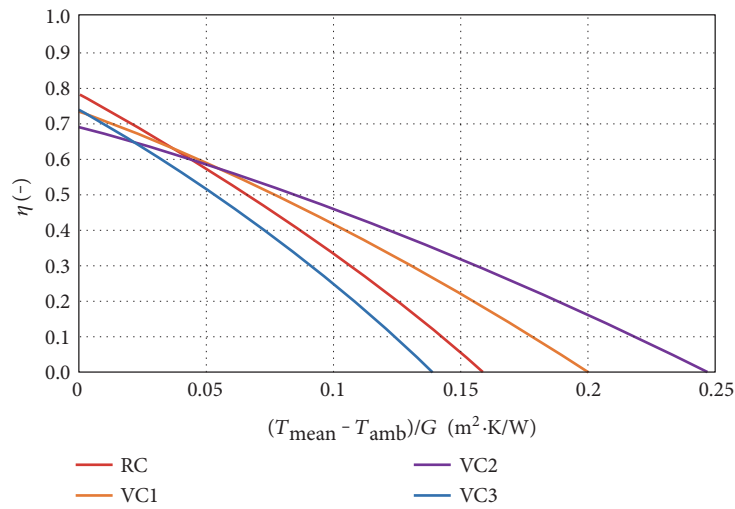


FIGURE 8: Efficiency characteristics of different solar collector variants.

glazing as a transparent cover). Four different solar collectors have been used for detailed model validation. The majority of solar thermal collector parameters (e.g., thermal conductivity of insulation, the solar transmittance of the glazing, and the emissivity of the absorber) have been measured experimentally to reduce the uncertainty range. The model has also been tested in the case of various values of slope, mass flow rate, wind velocity, and incident radiation. More information

TABLE 2: Summary of the collector simulation results.

Collector variants	η_0 (-)	a_1 (W/m ² ·K)	a_2 (W/m ² ·K ²)
RC	0.783	3.788	0.006
VC1	0.734	2.634	0.004
VC2	0.689	1.919	0.003
VC3	0.738	3.890	0.009

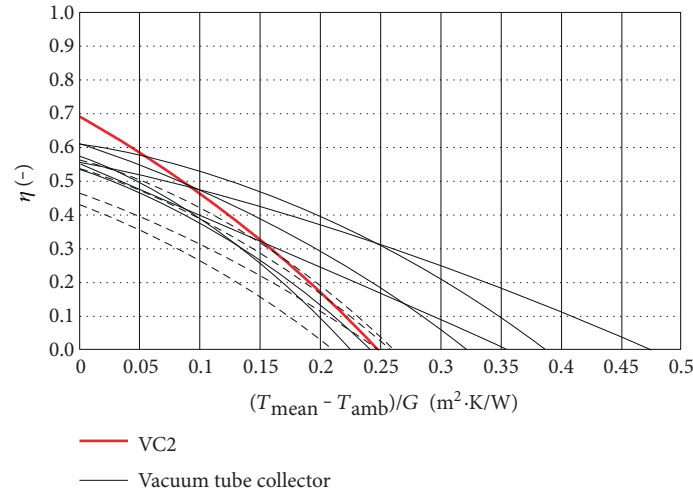


FIGURE 9: Efficiency characteristics of flat plate collector variant VC2 and vacuum tube collectors.

about model validation can be found in Shemelin and Matuska [24]. Figure 6 shows experimentally measured efficiency points and theoretically modeled efficiency characteristics. It is evident from the results that simulated efficiency characteristics fit the measurements relatively well, which gives confidence about the developed model.

4. Results and Discussion

Four configurations of FPC were modeled with dimensions 1×2 m. All variants have common state-of-the-art copper laser-welded absorber with a high-performance selective coating with absorptivity of 0.95 and emissivity of 0.05. The thickness of the absorber is 0.2 mm and the distance between pipes is 100 mm. Back thermal insulation and edge thermal insulation with thermal conductivity of 0.04 W/m·K have thickness 50 and 20 mm, respectively. The thickness of the air gap between absorber and glazing is 30 mm (except variant VC4, explained below). The difference between considered variants is only in the cover glazing.

The first configuration of FPC (RC) has a reference glazing (REF) as a transparent cover with the parameters shown in Table 1. The second configuration VC1 has a vacuum glazing VG1 instead of the reference glazing. The third configuration VC2 considers variant VG2 as cover glazing. The last configuration VC3 has a principally different configuration. This variant has no gap between the absorber and the cover. Here, the absorber is bonded to the VG2 by a permanently flexible, highly transparent silicone gel to reduce the thickness of the collector (“slim” collector alternative suitable for building envelope integration). Considered configurations of FPC collectors RC, VC1, VC2, and VC3 are shown in Figure 7.

The graph in Figure 8 shows the efficiency curves of considered solar collector variants. With respect to the EN ISO 9806, the collector efficiency η is based on the collector gross area A_G . The calculations have been done with the use of early described theoretical detailed model of FPC. The graph shows the difference in energy quality of

TABLE 3: Calculated annual solar collector gain with respect to the collector gross area.

Solar gain (kWh/m ²)	25°C	50°C	75°C	100°C
VC	697	548	422	320
VT1	653	552	462	378
VT2	586	480	386	303
VT3	527	465	390	308
VT4	603	511	421	337
VT5	616	515	416	320
VT6	577	478	386	304
VT7	708	646	583	518
VT8	607	493	400	318
VT9	626	556	494	436
VT10	667	590	510	427

compared FPC variants. The low slope of the efficiency curve of the VC2 is due to the collector VC2 having two low-e coatings—the first inside the vacuum glazing and the second on the absorber surface. Other variants RC, VC1, and VC3 have only one low-e coating. Solar collector alternative VC3 has lower thermal efficiency than the reference alternative REF. Despite the vacuum layer, higher emittance of the glass low-e coating (0.2) in the VC3 variant instead of absorber coating with emittance 0.05 in the REF variant, brings the total top heat loss to similar value, but optical parameters of the VC3 configuration are lower (lower zero loss efficiency η_0). The resulting coefficients of efficiency characteristics η_0 , a_1 , and a_2 are listed in Table 2.

On the other hand, solar collector variant VC3 has the lowest thickness between comparing variants—only 60 mm. Such thickness gives more possibility for integration of FPC into the building envelope because of the slim and compact design. Other variants RC, VC1, and VC2 have thicknesses 87, 91, and 91 mm, respectively.

Figure 9 presents the comparison of efficiency characteristics of flat plate collector variant VC2 and vacuum tube

collectors (with/without reflector, cylindrical/flat absorber) related to the gross area of a collector. Thermal performance of solar flat plate collector variant VC2 is comparable with that of vacuum tube collectors. Moreover, solar collector variant VC2 shows significantly higher efficiency than the majority of vacuum tube collectors (VT).

To get a whole picture, the annual performance of the collector VC2 and VT collectors has been modeled using ScenoCalc [25] software for constant operating temperatures 25, 50, 75, and 100°C and climate conditions of Würzburg. The performance and optical characteristics of the compared collectors were used as input data. The results are shown in Table 3. The results of the modeling confirmed that the flat plate solar collector variant VC2 has higher solar energy gains than the majority of vacuum tube collectors up to operating temperature 100°C.

5. Conclusions

Different designs of flat plate solar collectors based on a flat vacuum glazing have been theoretically investigated by using the detailed mathematical model to show the potential of vacuum glazing application in solar flat plate collectors. The selected variant VC2 has been compared with state-of-the-art vacuum tube collectors by annual simulation of collector heat output in ScenoCalc. Results have shown that there is a significant potential for increasing the efficiency of solar flat plate collectors by using high-performance vacuum glazing as a transparent cover. Collector variant VC2 shows higher performance than the majority of vacuum tube collectors up to operating temperature 100°C.

Conflicts of Interest

The authors declare that there is no conflict of interests regarding the publication of this paper.

Acknowledgments

This work has been supported by the Ministry of Education, Youth and Sports within the National Sustainability Programme I (NPU I), Project no. LO1605, by the University Centre for Energy Efficient Buildings-Sustainability Phase, and by the project SGS16/212/OHK2/3T/12—Modeling, control, and design of environmental engineering installations.

References

- [1] B. P. Veinberg and V. B. Veinberg, *Optics in Equipment for the Utilization of Solar Energy*, State Publishing House of Defense Industry, Moscow, 1959.
- [2] K. G. T. Hollands, "Honeycomb devices in flat plate solar collectors," *Solar Energy*, vol. 9, no. 3, pp. 159–164, 1965.
- [3] H. Tabor, "Cellular insulation (honeycombs)," *Solar Energy*, vol. 12, no. 4, pp. 549–552, 1969.
- [4] M. Rommel and A. Wagner, "Application of transparent insulation materials in improved flat plate collectors and integrated collectors storages," *Solar Energy*, vol. 49, no. 5, pp. 371–380, 1992.
- [5] H. Kessentini, J. Castro, R. Capdevila, and A. Oliva, "Development of flat plate collector with plastic transparent insulation and low-cost overheating protection system," *Applied Energy*, vol. 133, pp. 206–223, 2014.
- [6] S. Svendsen and K. I. Jensen, "Flat plate solar collector with monolithic silica aerogel," in *Proceedings of ISES World Congress*, pp. 620–624, Hamburg, Federal Republic of Germany, 1987.
- [7] S. Svendsen, "Solar collector with monolithic silica aerogel," *Journal of Non-Crystalline Solids*, vol. 145, pp. 240–243, 1992.
- [8] R. Duan, "The efficiency of new solar flat plate collectors," *Advanced Materials Research*, vol. 347–353, pp. 1337–1341, 2012.
- [9] C. Eaton and H. A. Blum, "The use of moderate vacuum environments as a means of increasing the collection efficiencies and operating temperatures of flat-plate solar collectors," *Solar Energy*, vol. 17, no. 3, pp. 151–158, 1975.
- [10] N. Benz and T. Beikircher, "High efficiency evacuated flat plate solar collector for process steam production," *Solar Energy*, vol. 65, no. 2, pp. 111–118, 1999.
- [11] C. Benvenuti, "Evacuatable flat panel solar collector," PCT/EP2004/000503, CERN, 2005.
- [12] R. Moss and S. Shire, "Design and performance of evacuated solar collector microchannel plates," in *EuroSun Conference*, Aix-les-Bains, France, 2014.
- [13] G. S. F. Shire, R. W. Moss, P. Henshall, F. Arya, P. C. Eames, and T. Hyde, "Development of an efficient low-and medium-temperature vacuum flat-plate solar thermal collector," in *Renewable Energy in the Service of Mankind*, vol. 2, pp. 859–866, Springer International Publishing, Switzerland, 2016.
- [14] Y. Fang, T. Hyde, P. C. Eames, P. C. Eames, and N. Hewitt, "Theoretical and experiment analysis of the vacuum pressure in a vacuum glazing after extreme thermal cycling," *Solar Energy*, vol. 83, no. 9, pp. 1723–1730, 2009.
- [15] M. M. Koebel, H. Manz, K. E. Mayerhofer, and B. Keller, "Service-life limitations in vacuum glazing: a transient pressure balance model," *Solar Energy Materials and Solar Cells*, vol. 94, no. 6, pp. 1015–1024, 2010.
- [16] H. Weinlader, "VIG-vacuum insulation glass," in *Proceedings of IVIS—7th International Vacuum Insulation*, Duebendorf/ Zurich, Switzerland, 2005.
- [17] R. E. Collins and T. M. Simko, "Current status of the science and technology of vacuum glazing," *Solar Energy*, vol. 62, no. 3, pp. 189–213, 1998.
- [18] F. Giovannetti, S. Foste, and N. Ehrmann, "High transmittance, low emissivity glass covers for flat plate collectors: applications and performance," *Energy Procedia*, vol. 30, pp. 106–115, 2012.
- [19] T. Matuska and V. Zmrhal, "A mathematical model and design tool KOLEKTOR 2.2," Reference handbook, 2009.
- [20] H. C. Hottel and B. B. Woertz, "The performance of flat plate solar-heat collectors," *Transactions of the ASME*, vol. 64, pp. 64–91, 1942.
- [21] H. C. Hottel and A. Whillier, "Evaluation of flat-plate solar collector performance," *Transactions of Conference on the Use of Solar Energy*, vol. 3, 1954.
- [22] J. Bliss, "The derivations of several "plate-efficiency factors" useful in the design of flat plate heat collectors," *Solar Energy*, vol. 3, no. 4, pp. 55–64, 1959.
- [23] J. A. Duffie and W. A. Beckman, *Solar Engineering of Thermal Processes*, Wiley, New York NY, 4th edition, 2013.

- [24] V. Shemelin and T. Matuska, "Detailed model of flat plate solar collector," 2015, http://users.fs.cvut.cz/tomas.matuska/?page_id=582.
- [25] "ScenoCalc v.5.01. Solar collector energy output calculator – a program for calculation of annual solar collector energy output," <https://www.sp.se/en/index/services/solar/ScenoCalc/Sidor/default.aspx>.

Research Article

Performance Analysis of Photovoltaic Water Heating System

Tomas Matuska¹ and Borivoj Sourek²

¹*Faculty of Mechanical Engineering, Czech Technical University, Technicka 4, 166 07 Prague 6, Czech Republic*

²*University Centre of Energy Efficient Buildings, Czech Technical University, Trinecka 1024, 273 43 Bustehrad, Czech Republic*

Correspondence should be addressed to Tomas Matuska; tomas.matuska@fs.cvut.cz

Received 10 February 2017; Revised 29 March 2017; Accepted 13 April 2017; Published 16 May 2017

Academic Editor: Stoian Petrescu

Copyright © 2017 Tomas Matuska and Borivoj Sourek. This is an open access article distributed under the Creative Commons Attribution License, which permits unrestricted use, distribution, and reproduction in any medium, provided the original work is properly cited.

Performance of solar photovoltaic water heating systems with direct coupling of PV array to DC resistive heating elements has been studied and compared with solar photothermal systems. An analysis of optimum fixed load resistance for different climate conditions has been performed for simple PV heating systems. The optimum value of the fixed load resistance depends on the climate, especially on annual solar irradiation level. Use of maximum power point tracking compared to fixed optimized load resistance increases the annual yield by 20 to 35%. While total annual efficiency of the PV water heating systems in Europe ranges from 10% for PV systems without MPP tracking up to 15% for system with advanced MPP trackers, the efficiency of solar photothermal system for identical hot water load and climate conditions is more than 3 times higher.

1. Introduction

Significant decrease of photovoltaic (PV) technology cost in the last decade has opened a new market with simple solar water heating systems combining the PV modules and direct current (DC) electric heating elements. The public research exhibits a significant lack of publications on the photovoltaic technology dedicated for water heating only. On the other hand, there exist a number of patented photovoltaic water heating system configurations. Fannee and Dougherty [1] disclosed the PV water heater comprising a variable resistive load which is provided by a number of resistances sequentially switched by external controller according to actual irradiance to provide the maximum power output of PV array to DC resistive heating elements. Thomasson [2] uses the PV hot water system with the DC resistive heating elements immersed in two cascade hot water tanks with controlled charging according to priority and power available. Newman and Newman [3] suggested PV water heating system with new resistive heating element comprising an array of individual fixed resistance heating rods controlled by microprocessor unit to vary the resistance of heating element and provide maximum PV power for heating. Butler [4] has patented photovoltaic DC heater based on resistive heating

element designed for immersion into the standard hot water tanks and which can be used also in other applications (open liquid containers, air heating, etc.). The market today offers a number of PV heating systems with a PV array directly coupled to DC electric heater. Simple PV water heating systems with optimized but fixed load resistance of DC resistive heating element do not need an extra control unit. Control of load resistance with the use of switching on and off the number of additional resistive elements by relays to match the load resistance to PV array conditions results in advanced microprocessor control units. A number of techniques and methods to maintain the PV array at maximum power conditions have been developed and widely applied in modern PV system controllers. Extensive summary and comparison of the maximum power point tracking devices can be found in numerous literature [5–8]. Apart from the PV water heating systems, there are conventional solar photothermal water heating systems, which can be considered as a mature technology, despite continuously ongoing research activities. Diverse forms of solar energy water heating systems have been extensively classified and reviewed by Norton [9]. Recent advances in the development of components for active and passive solar water heating systems have been reviewed in the work Shukla et al. [10]. Comprehensive

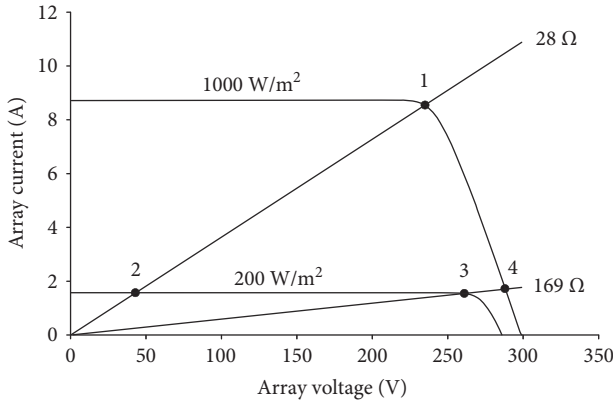


FIGURE 1: Electric (I-V) characteristics of photovoltaic array 2 kW_p (8 × 250 W_p in series).

review of drainback solar heating systems has been done by Botpaev et al. [11]. In the recent decades, water heating with use of photovoltaic-thermal (PV-T) collectors has been extensively investigated. Various designs of PV-T collectors and systems have been modelled and tested. Chow et al. [12] have studied the appropriateness of glass cover on a thermosyphon-based water-heating PV/T system under the influence of main system parameters. Mishra and Tiwari [13] have investigated the configuration of photothermal collector partially and fully covered by PV module. Lämmle et al. [14] have suggested a concept of PV-T collector with inflatable glass-film cushion to control thermal losses of the collector to combine advantages and disadvantages of unglazed and glazed PVT collector and to avoid overheating of PV encapsulation at stagnation conditions. Haurant et al. [15] have investigated glazed PV-T collector with exceptional conversion efficiencies operated in solar water heating system. Matuska et al. [16] have developed glazed PV-T collector with thermally resistant encapsulation and investigated the energy and economic performance in solar water heating system for a multifamily house.

The paper analyses the annual energy performance of PV-only solar water heating system. First part of the paper is focused on the analysis of difference in electricity production of PV array for DC electric heater when using MPP tracking and fixed load resistance. Second part of the paper analyses the solar photovoltaic hot water system with the use of PV modules in both alternatives (MPPT, fixed load resistance) and compares its performance with a conventional solar hot water system with photothermal flat plate collectors operated at identical hot water load and climate conditions. The comparison of given water heating solar systems does not consider anyhow the economic parameters (investment costs, energy price, interest rate, etc.), which are dependent on the country and application field. On the other hand, because economic point of view could influence the optimal sizing of solar collector (photovoltaic, photothermal) area, the analyses have been performed always as parametric ones with a certain range of system size for different climates.

TABLE 1: Parameters of the PV modules used in analysis.

Parameter	Value
Maximum power P_{\max}	250 W
Maximum power voltage V_{pm}	29.8 V
Maximum power current I_{pm}	8.39 A
Open circuit voltage V_{oc}	36.9 V
Short circuit current I_{sc}	9.09 A
Temperature coefficient of voltage $\beta_{V_{\text{oc}}}$	-0.36%/K
Temperature coefficient of current $\beta_{I_{\text{sc}}}$	0.06%/K
Nominal operating cell temperature NOCT	45°C

2. Power Output of PV Array for Water Heating

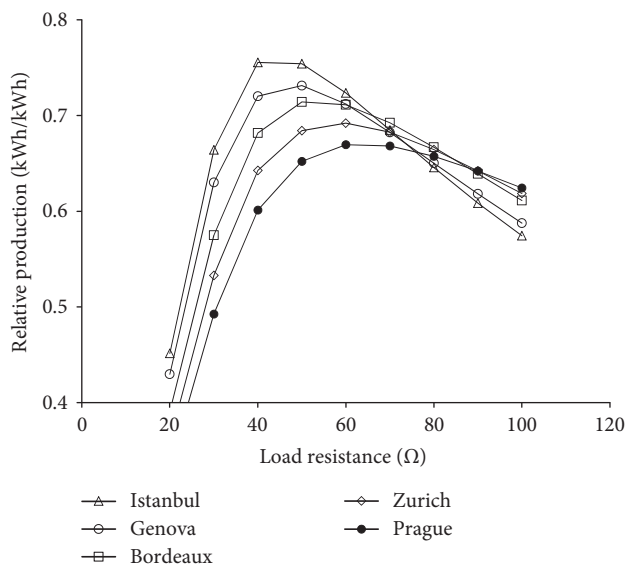
Photovoltaic hot water systems considered in the analysis combine the PV modules for direct current generation which is utilized for electric heating elements immersed in the hot water tank. Photovoltaic modules are electric generators with nonlinear current-voltage (I-V) characteristics. The produced electric power of the PV array is significantly influenced by solar irradiance, less by ambient temperature, but anyway, it depends on the connected electric load (load resistance). Figure 1 shows the I-V characteristics of the photovoltaic array assembled from 8 polycrystalline modules connected in series with a peak power 2 kW_p. I-V characteristics for two different levels of solar irradiance 200 W/m² and 1000 W/m² are given as an example how the load resistance value influences the power output of PV array. Application of load resistance 28 Ω results in maximum power 2000 W at point 1 for solar irradiance 1000 W/m², but the optimum load resistance to provide maximum power output for solar irradiance 200 W/m² (403 W at point 3) is 169 Ω. The application of different load resistance value than the optimum one results in lower electric power output as seen in point 2 (68 W for irradiance 200 W/m²) and point 4 (502 W for irradiance 1000 W/m²). It can be generally concluded that high load resistance values are suitable for low irradiance levels while low load resistance values provide maximum power output for high irradiance levels.

In order to maintain the PV array at maximum power output conditions, the load resistance has to vary and adapt to actual operation conditions of the PV array. Despite this fact, the low-cost PV water heaters available today on the market often miss any MPP tracking device and utilize the PV array directly connected to DC electric heating element with fixed load resistance value optimized from the point of annual performance.

An analysis has been performed to find the optimum load resistance value for given PV array to be used as fixed parameter during the whole year and to provide the maximum performance for given operation conditions. Typical PV arrays used in PV water heaters are based on polycrystalline technology. PV modules with peak power output 250 W_p have been considered in the analysis. Detailed parameters of the PV modules are shown in Table 1.

TABLE 2: Climate characteristics for selected locations.

Location	Average ambient temperature [°C]	Total irradiation horizontal [kWh/m ² .a]	Total irradiation south, tilted 45° [kWh/m ² .a]	Beam irradiation south, tilted 45° [kWh/m ² .a]
Madrid (ES)	13.9	1662	1864	1163
Istanbul (TR)	14.1	1627	1805	1088
Athens (GR)	17.6	1562	1696	914
Genova (IT)	15.8	1447	1637	944
Bordeaux (FR)	12.7	1270	1448	744
Milano (IT)	11.6	1188	1342	657
Zurich (CH)	9.1	1105	1237	585
Prague (CZ)	7.9	998	1115	487
Stockholm (SE)	5.3	980	1232	687

FIGURE 2: Dependence of 2 kW_p PV array relative production on load resistance for selected locations.

Annual performance of 4 PV modules (1 kW_p) and 8 PV modules (2 kW_p) connected in series to PV array has been analysed in the MPPT mode (MPPT-on) and with fixed load resistance (MPPT-off). To model the electricity production of PV array, four-parameter mathematical model [17] has been used. The model allows to evaluate the maximum power of the module (MPP tracking), but also with given electric load resistance (given load voltage applied, model determines the current as a function of load voltage). The analysis of the PV array electricity production in both modes (MPPT-on, MPPT-off) has been performed for different climates in Europe. Climate characteristics of the selected locations are shown in Table 2. PV modules were considered with south orientation and slope 45° in all alternatives.

Figure 2 shows the relative production as a ratio between the annual electricity production of PV array

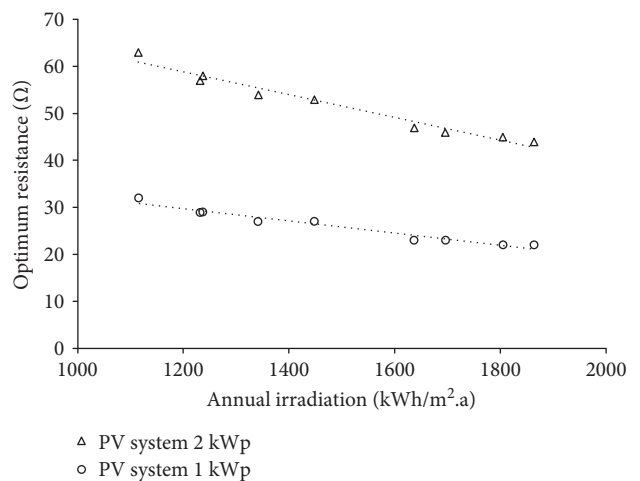


FIGURE 3: Optimum load resistance of PV arrays as a function of annual solar irradiation.

2 kW_p with fixed electric load resistance (MPPT-off) and annual electricity production under maximum power point tracking (MPPT-on). The trends are similar for other sizes of PV array with a serial connection of modules, and optimum load resistance value for MPPT-off mode is directly proportional to open circuit voltage V_{oc} of the PV array. It has been also proved that the optimum load resistance value is significantly influenced by climate conditions, especially by solar irradiation. Figure 3 shows the dependency of the optimum load resistance value on annual solar irradiation for different locations in Europe. Optimum load resistance value is indirectly proportional to the annual solar irradiation.

Figure 4 shows the difference between the specific electricity production of PV array for MPPT-on mode and for MPPT-off mode with fixed load resistance optimized for given European climates. The difference in performance between both modes ranges from 25% for sunny regions to 35% for regions with low solar irradiation.

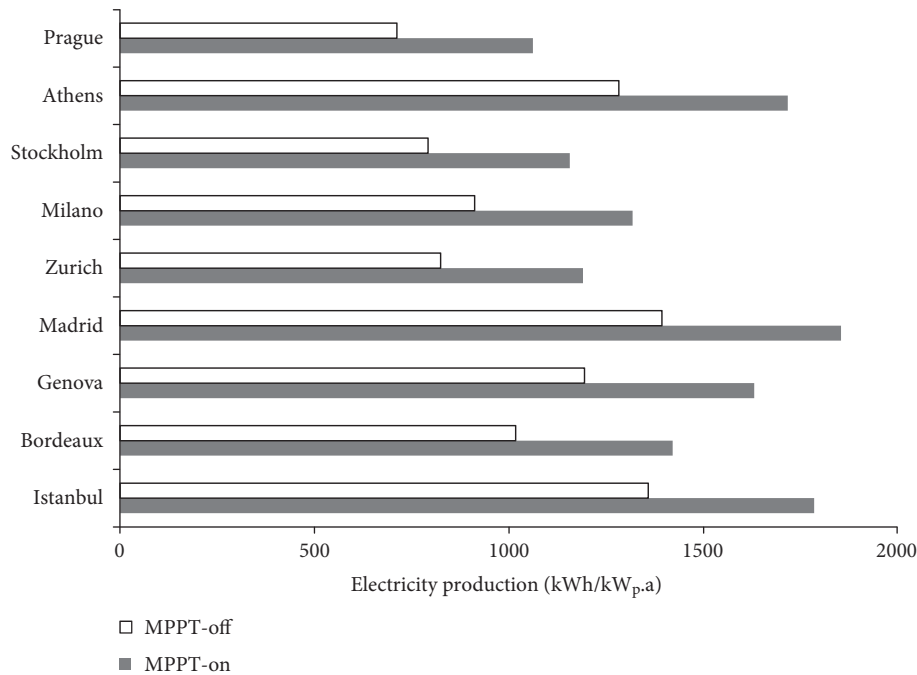


FIGURE 4: Specific electricity yields of PV array in different climates for maximum power point tracking mode (MPPT-on) and for optimized load resistance mode (MPPT-off).

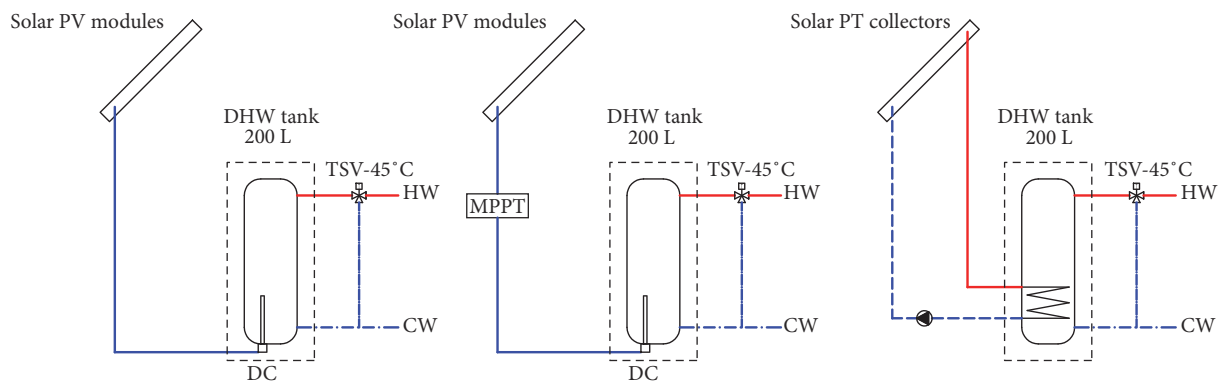


FIGURE 5: Scheme of solar hot water systems (PV without MPPT, PV with MPPT, and solar thermal).

3. Solar Hot Water Systems Analysis

Detailed mathematical models have been used for the solar photovoltaic and solar photothermal hot water systems for family houses to compare the energy performance at identical boundary conditions. Solar systems have been simulated in TRNSYS [18] in the following alternatives (see Figure 5):

- (i) Photovoltaic hot water system without MPPT (MPPT-off)
- (ii) Photovoltaic hot water system with MPPT (MPPT-on)
- (iii) Photothermal hot water system.

Each solar system alternative has been used only for hot water preparation. Daily hot water load 200l (3 to 4 persons) for typical household has been considered with required hot water temperature 45°C and cold water temperature 10°C (considered constant during the whole year in all alternatives to keep the same heat demand for comparison). Relative daily profile of hot water load has been taken from Mandate 324 [19] as profile M. Total hot water heat demand is 2974 kWh/a. Solar water tank volume 200l with a heat loss 1.4 kWh/day has been considered in all alternatives. The water tank was used as a preheating stage for conventional water heater. Maximum temperature in solar water tank has been set to 85°C as recommended by manufacturer for all systems. Output hot water temperature from the solar

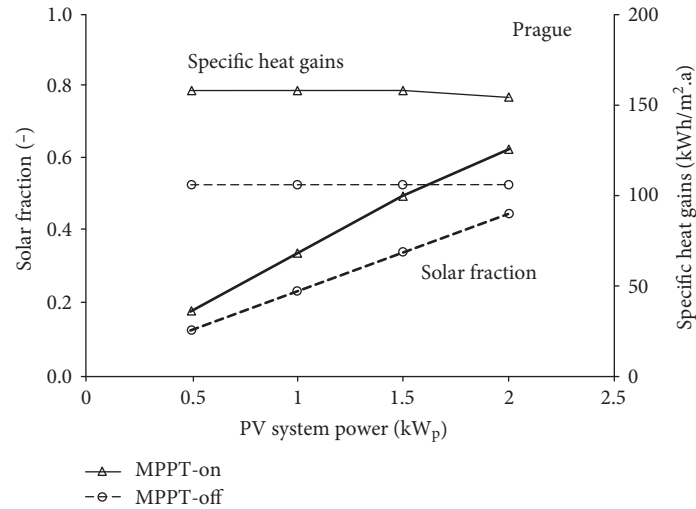


FIGURE 6: Performance characteristics of solar PV hot water system in the climate of Prague.

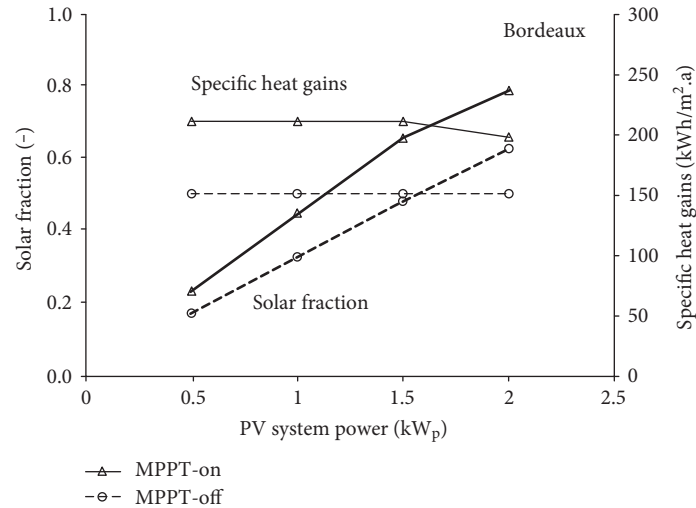


FIGURE 7: Performance characteristics of solar PV hot water systems in the climate of Bordeaux.

preheating systems has been controlled by a thermostatic valve to 45°C (upper limit). Back-up energy has been evaluated from actual water load and temperature difference between thermostatic valve output and required hot water temperature. Solar water tanks have been modelled uniformly with TRNSYS model (type 340) [20], which allows to model the solar water tanks with electric heating elements and with tube heat exchangers. Solar systems have been considered in different climates and with different sizes of the solar source (PV array size, solar thermal collector area).

3.1. Solar Photovoltaic Hot Water System. Annual performance of photovoltaic hot water system has been investigated in two mentioned alternatives of operation mode for PV array: photovoltaic system with MPPT device (MPPT-on) and without MPPT (MPPT-off). PV array has been modelled with use of TRNSYS model (type 180) including electrical and thermal model. PV hot water system has been

designed in several alternatives available on the market today. PV array was considered with a peak power output from 0.5 kW_p to 2 kW_p assembled from standard 250 W_p polycrystalline modules (for parameters see Table 1). Solar PV hot water system has been considered in different climate zones. Dependence of solar fraction and specific heat gains of the system has been evaluated in detail for three selected locations (Prague, Bordeaux, and Istanbul). Results are shown in Figures 6–8 (mind the different scales of graphs for specific heat gains). Optimum load resistance has been used for the PV array operated in MPPT-off mode according to Table 3.

Whole year modelling of PV hot water system performance has considered change of module electric power with solar irradiance incident angle (optical characteristic, incidence angle modifier IAM). Total cable electric losses of the system have been considered 2%. Simulation has not considered long-term degradation of PV module power, usually referred from 0.5 to 1% annually.

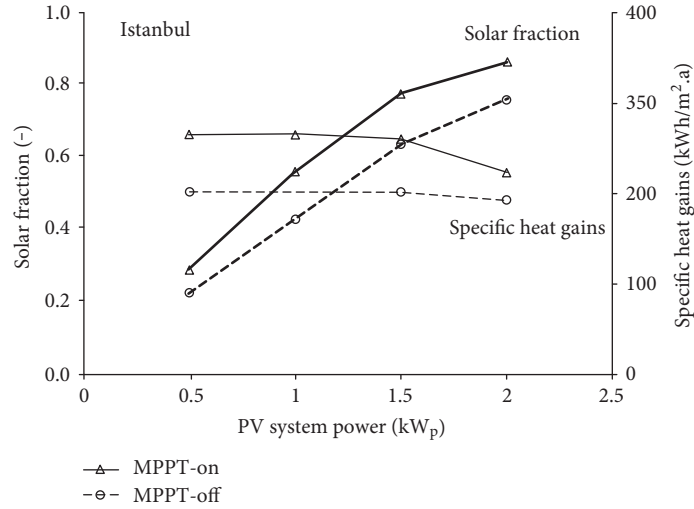


FIGURE 8: Performance characteristics of solar PV hot water systems in the climate of Istanbul.

TABLE 3: Optimum load resistance for different sizes of PV array in different climates.

Number of modules/power [kW _p]	2/0.5	4/1.0	6/1.5	8/2.0
Madrid	11	22	33	44
Istanbul	11	23	34	45
Athens	12	23	35	46
Genova	12	24	35	47
Bordeaux	13	27	40	53
Milano	14	27	41	54
Zurich	15	29	44	58
Prague	16	32	47	63
Stockholm	14	29	43	57

As shown in graphs, the solar fraction increases almost linearly with peak power of PV array, until excess heat gains are present during the summer season when the PV array is oversized. This results in lower energy production for heating than the available potential is. Similarly, the specific heat gains are in principle constant with no dependence on applied size of the system. Only in the case of oversized PV array with respect to hot water load, the specific heat gains are reduced.

3.2. Photothermal Hot Water System. Solar photothermal hot water system has been considered with flat plate solar thermal collectors with forced circulation. Main parameters of solar photothermal collectors required by TRNSYS model type 1b are shown in Table 4. Collector loop flowrate has been considered 40 l/h.m² of collector area. Collector loop consists of copper pipes 18×1 mm at total length 30 m equipped with thermal insulation 19 mm thick. The loop is connected to tube heat exchanger immersed in the lower part of solar water tank identical with tank used in PV hot water system. Tube heat exchanger has a

TABLE 4: Main parameters of solar photothermal collectors used in analysis.

Parameter	Value
Zero-loss efficiency η_0 [-]	0.79
Linear heat loss coefficient a_1 [W/m ² K]	4.0
Quadratic heat loss coefficient a_2 [W/m ² K ²]	0.015
Incidence angle modifier for 50° IAM ₅₀	0.95

surface area 1 m². Nominal specific heat capacity of the heat exchanger has been considered 170 W/K. Solar water tank model considers also the influence of flowrate, temperature difference, and mean temperature on the heat transfer capacity of the heat exchanger.

Solar thermal hot water system has been analysed with different sizes of solar collector array. Alternatives with solar collector area from 1 to 4 m² have been considered. Detailed results are shown in Figures 9–11 for selected locations with different climates (Prague, Bordeaux, and Istanbul). While solar fraction increases with large area of solar collectors, the annual specific heat gains decrease. This is caused by significant dependence of solar collector yields on the operation temperature. Larger collector area delivering higher absolute energy gains into storage tank leads to higher average operation temperatures of solar system and thus lower collector efficiency and higher loss of collector loop piping. Excess solar heat gains in summer, especially present for sunny climates due to oversized collector area, result in worse usability of the system and further decrease in specific heat gains.

4. Experimental Analysis

Three investigated types of solar water heating systems have been analysed also experimentally (see Figure 12). Photothermal system has used two conventional flat plate collectors

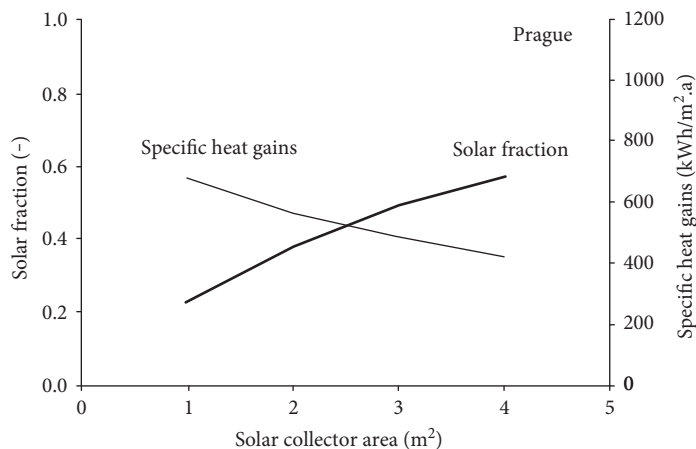


FIGURE 9: Performance characteristics of solar photothermal hot water systems in the climate of Prague.

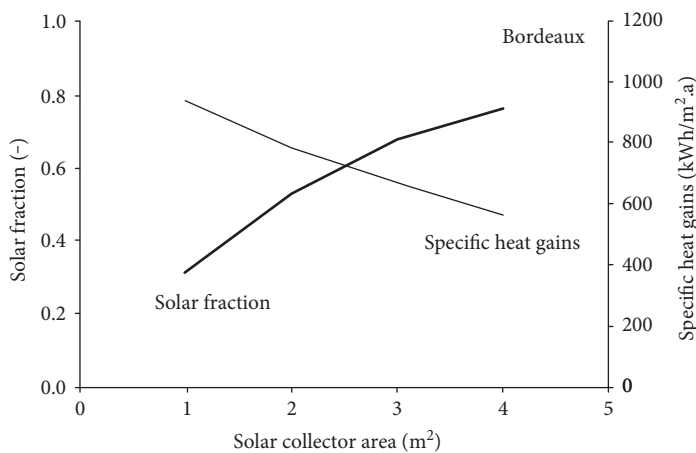


FIGURE 10: Performance characteristics of solar photothermal hot water systems in the climate of Bordeaux.

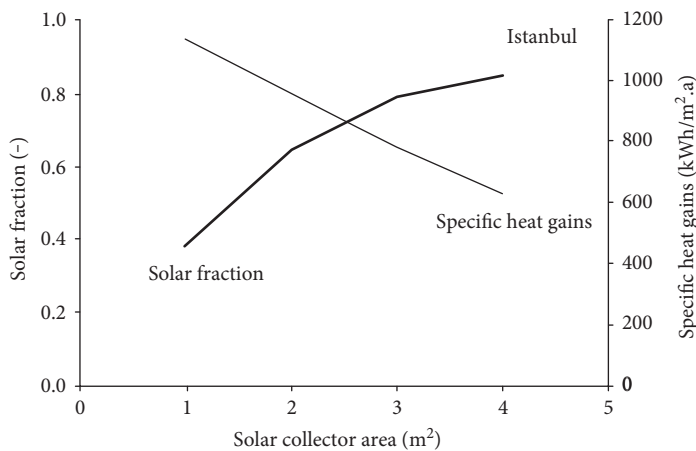


FIGURE 11: Performance characteristics of solar photothermal hot water systems in the climate of Istanbul.



FIGURE 12: View on solar photothermal and photovoltaic collectors installed for experimentally tested system.

TABLE 5: Main parameters of experimental solar water heating systems.

	PV system without MPPT	PV system with MPPT	Photothermal system
Solar collector area	12.8 m ² /1.92 kW _p	12.8 m ² /1.92 kW _p	3.56 m ²
Storage tank volume	200l	200l	200l

with active collector area 3.56 m². Both photovoltaic systems (with MPPT, without MPPT) have used 8 polycrystalline PV modules each with peak power 240 kW_p. All solar water heating systems have been equipped with identical solar storage tank (volume 200l, daily heat loss 1.4 kWh/day). The main parameters of the solar water heating systems are listed in the Table 5. The storage tank for the solar photothermal system has a tube heat exchanger; storage tank for solar photovoltaic systems has a DC heating element with nominal power 2 kW. Storage tanks were not equipped by any additional back-up heater; the solar water heating systems have been used as a preheating stage. The orientation and the slope of solar collectors and PV modules have been the same: orientation 15° to east (from south) and slope 45°. Thus, the identical climate conditions (Ziar nad Hronom, Slovakia) have been ensured for all experimentally tested systems.

The daily hot water load for the solar water heating systems has been 200l of water at temperature 45°C. The usable solar heat gains from water heating systems have been evaluated.

The experimental testing of solar systems has started in September 2013. In the beginning, only solar photothermal system and solar photovoltaic system without MPPT have been operated for water heating. Later in 2014, solar photovoltaic alternative with MPPT has been added for comparison to both water heating systems. The results from experimental testing are shown in Table 6 and in the graph in Figure 13 for all solar water heating systems.

Systems were compared for the first season from the beginning of September 2013 to the end of August 2014. The annual heat gains of the photothermal system are 1544 kWh/a, that is 434 kWh/m².a. Annual heat gains of photovoltaic system without MPPT are 1322 kWh/a, that is 103 kWh/m².a. Both results are in line with values graphically presented in Figure 6 (considering PV module power 1.92 kW_p) and Figure 9 (considering collector area 3.56 m²). The climate of the location with tested systems (Ziar nad Hronom) and climate of Prague used for simulations have similar weather conditions. Comparison of PV heating systems with MPPT and without MPPT

TABLE 6: Experimental evaluation of solar water heating systems.

Month	PV system without MPPT [kWh]	PV system with MPPT [kWh]	Photothermal system [kWh]
Sept 2013	138	0	154
Oct 2013	117	0	134
Nov 2013	37	0	47
Dec 2013	24	0	36
Jan 2014	19	0	29
Feb 2014	54	0	72
Mar 2014	139	0	155
Apr 2014	144	0	172
May 2014	155	0	181
Jun 2014	194	227	220
Jul 2014	171	188	197
Aug 2014	131	143	147
Sept 2014	87	107	116
Oct 2014	74	88	93
Nov 2014	31	46	45
Dec 2014	33	53	42
Jan 2015	26	40	36
Feb 2015	78	110	89

control has shown about 20% higher usable heat gain for system with MPPT control, which confirms presented theoretical simulations.

5. Comparison and Discussion

When comparing the performance of solar water heating systems, the total system efficiency can be taken as parameter which shows the demand of the system on available roof area. Figure 14 shows the dependence of annual specific heat gains on the annual incident solar irradiation for all investigated alternatives (size, climate). Ratio of these quantities results in total system efficiency.

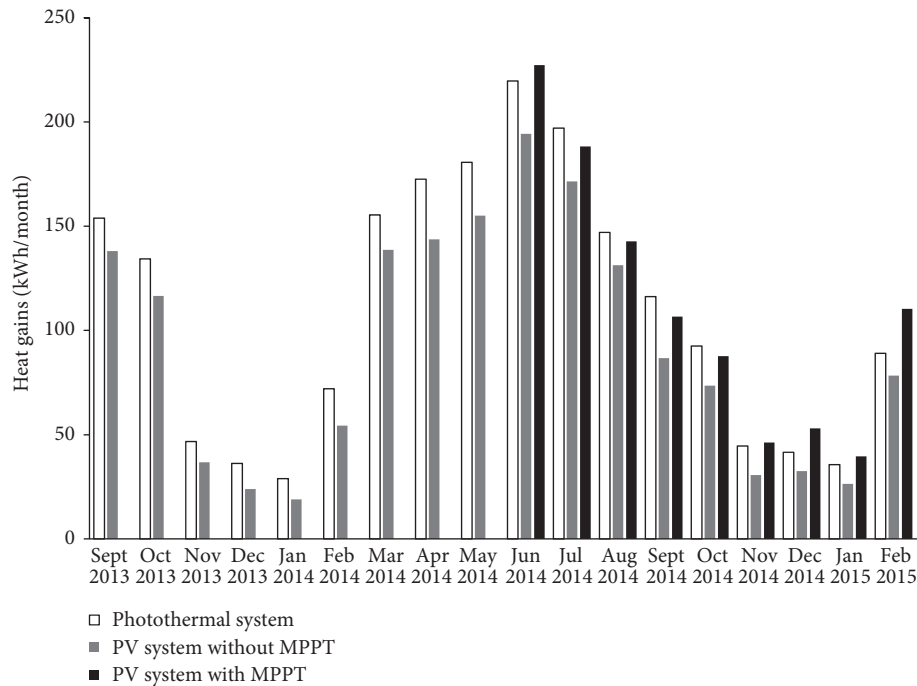


FIGURE 13: Experimental evaluation of solar water heating systems.

Efficiency of PV water heating systems depends only on usability of PV array production for water heating. Excess heat gains during summer season which cannot be utilized degrade the total system efficiency. Difference between the efficiency of PV systems with MPP tracking and with fixed load resistance has been monitored in the analysis. While efficiency of PV water heating system with MPP tracking ranges between 13 and 15% for all climates, the efficiency of simple system without MPPT achieve the efficiency between 10 and 11%.

Performance of the solar thermal systems is much more dependent on the operation conditions. While electricity generation from PV array is independent on the storage tank temperature, heat generation of solar thermal collector decreases with the tank temperature, because it directly influences the collector fluid operation temperature and thus thermal losses of solar collector and collector loop. This is the reason for large dispersion of points in the graph in Figure 14 for solar photothermal (PT) system case. The total efficiency of photothermal systems ranges from 35 to 68%.

The comparison of total system efficiency clearly states that solar thermal system demands about 3 to 6 times less roof area for water heating than the PV water heating system.

6. Conclusion

Solar photovoltaic water heating systems based on direct coupling of PV array to DC resistive heating elements immersed in hot water tank have been studied. Use of maximum power point tracking compared to fixed optimized load resistance increases the annual yield by 20 to 35%. The optimum value of the fixed load resistance depends on the climate, especially on annual solar irradiation level. The total

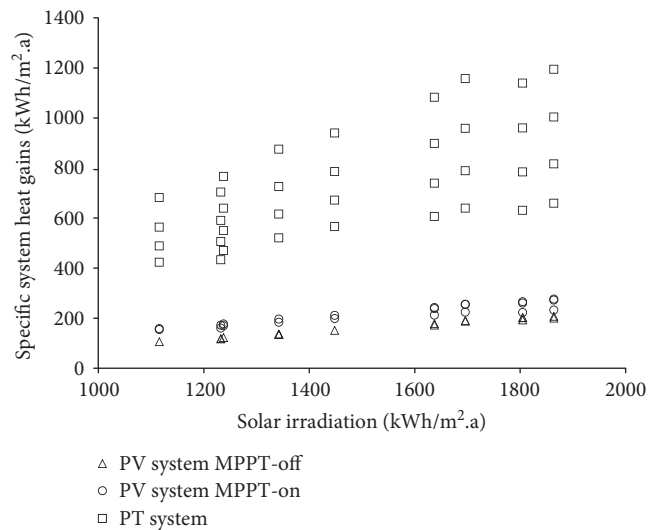


FIGURE 14: Relationship between specific heat gains and solar irradiation for solar hot water systems.

annual efficiency of the PV water heating systems in Europe ranges from 10% for PV systems without MPP tracking up to 15% for system with advanced MPP trackers. However, such values are dramatically lower than the efficiency of solar photothermal system for identical hot water load and climate conditions. Despite the fact that efficiency of solar photothermal system is influenced by sizing more than PV heating system, the efficiency is more than 3 times higher. The theoretical analysis has been verified by experimental testing of the solar water heating systems.

Conflicts of Interest

The authors declare that there is no conflict of interest regarding the publication of this paper.

Acknowledgments

This work has been supported by the Ministry of Education, Youth and Sports within the National Sustainability Programme I (NPU I), Project no. LO1605, University Centre for Energy Efficient Buildings—Sustainability Phase.

References

- [1] A. H. Fanney and B. P. Dougherty, "Photovoltaic solar water heating system," United States Patent 5293447, 1994.
- [2] S. L. Thomasson, "PV water heating system," United States Patent US 20090214195, 2008.
- [3] M. Newman and G. Newman, "Solar photovoltaic water heating system," United States Patent US 20140153913, 2014.
- [4] B. L. Butler, "Photovoltaic DC heater systems," United States Patent US 9518759, 2016.
- [5] H. Rezk and A. M. Eltamaly, "A comprehensive comparison of different MPPT techniques for photovoltaic systems," *Solar Energy*, vol. 112, pp. 1–11, 2015.
- [6] S. Saravanan and N. R. Babu, "Maximum power point tracking algorithms for photovoltaic system – a review," *Renewable and Sustainable Energy Reviews*, vol. 57, pp. 192–204, 2016.
- [7] M. A. M. Ramli, S. Twaha, K. Ishaque, and Y. A. Al-Turki, "A review on maximum power point tracking for photovoltaic systems with and without shading conditions," *Renewable and Sustainable Energy Reviews*, vol. 67, pp. 144–159, 2017.
- [8] N. Karami, N. Moubayed, and R. Outbib, "General review and classification of different MPPT techniques," *Renewable and Sustainable Energy Reviews*, vol. 68, Part 1, pp. 1–18, 2017.
- [9] B. Norton, "Solar water heaters: a review of systems research and design innovation," *Green*, vol. 1, no. 2, pp. 189–207, 2011.
- [10] R. Shukla, K. Sumathy, P. Erickson, and J. Gong, "Recent advances in the solar water heating systems: a review," *Renewable and Sustainable Energy Reviews*, vol. 19, pp. 173–190, 2013.
- [11] R. Botpaev, Y. Louvet, B. Perers, S. Furbo, and K. Vajen, "Drainback solar thermal systems: a review," *Solar Energy*, vol. 128, pp. 41–60, 2016.
- [12] T. T. Chow, G. Pei, K. F. Fong, Z. Lin, A. L. S. Chan, and J. Ji, "Energy and exergy analysis of photovoltaic-thermal collector with and without glass cover," *Applied Energy*, vol. 86, no. 3, pp. 310–316, 2009.
- [13] R. K. Mishra and G. N. Tiwari, "Energy and exergy analysis of hybrid photovoltaic thermal water collector for constant collection temperature mode," *Solar Energy*, vol. 90, pp. 58–67, 2013.
- [14] M. Lämmle, C. Thoma, and M. Hermann, "A PVT collector concept with variable film insulation and low-emissivity coating," *Energy Procedia*, vol. 91, pp. 72–77, 2016.
- [15] P. Haurant, C. Ménézo, L. Gaillard, and P. Dupeyrat, "Dynamic numerical model of a high efficiency PV–T collector integrated into a domestic hot water system," *Solar Energy*, vol. 111, pp. 68–81, 2015.
- [16] T. Matuska, B. Sourek, V. Jirka, and N. Pokorny, "Glazed PVT collector with Polysiloxane encapsulation of PV cells: Performance and economic analysis," *International Journal of Photoenergy*, vol. 2015, Article ID 718316, 7 pages, 2015.
- [17] J. A. Duffie and W. A. Beckman, *Solar Engineering of Thermal Processes*, John Wiley & Sons, Inc., New York, 1991.
- [18] Transient system simulation tool TRNSYS 17.1," University of Madison, 2012, <http://www.trnsys.com>.
- [19] European Commission, *M/324 Mandate to CEN and CENELEC for the Elaboration and Adoption of Measurement Standards for Household Appliances: Water-Heaters, hot Water Storage Appliances and Water Heating Systems*, European Commission, Brussels, Belgium, 2002.
- [20] H. Drucek, *Multiport Store Model for TRNSYS - Stratified Fluid Storage Tank with four Internal Heat Exchangers, Ten Connections for Direct Charge and Discharge and an Internal Electrical Heater (type340)*, University of Stuttgart, Germany, 2006.

Research Article

Design and Optimization of Elliptical Cavity Tube Receivers in the Parabolic Trough Solar Collector

Fei Cao,^{1,2} Lei Wang,¹ and Tianyu Zhu¹

¹College of Mechanical and Electrical Engineering, Hohai University, Changzhou 213022, China

²Sunshore Solar Energy Company Limited, Nantong 226300, China

Correspondence should be addressed to Fei Cao; yq.cao@hotmail.com

Received 8 January 2017; Accepted 28 February 2017; Published 30 March 2017

Academic Editor: Stoian Petrescu

Copyright © 2017 Fei Cao et al. This is an open access article distributed under the Creative Commons Attribution License, which permits unrestricted use, distribution, and reproduction in any medium, provided the original work is properly cited.

The nonfragile cavity receiver is of high significance to the solar parabolic trough collector (PTC). In the present study, light distributions in the cavity under different tracking error angles and PTC configurations are analyzed. A new elliptical cavity geometry is proposed and analyzed. It is obtained from this study that light distribution on the tube receiver is asymmetrical when tracking error occurs. On increasing the tracking error angle, more lights are sheltered by the cavity outer surface. The PTC focal distance has negative correlation with the cavity open length, whereas the PTC concentration ratio has positive correlation with the cavity open length. Increasing the tracking error angle and increasing the PTC focal distance would both decrease the cavity blackness. Introducing a flat plate reflector at the elliptical cavity open inlet can largely increase the cavity darkness.

1. Introduction

Solar energy has been recognized as one of the most important energy sources at present and in the further energy structure. Due to the discontinuous, low energy flux, periodicity, and unsteady characteristics of solar energy, solar concentration is commonly utilized in solar engineering fields, among which the solar parabolic trough collectors (PTC) are the most widely accepted solar concentration style [1]. The light ray tracing [2–4] and structural analysis [5–7] for the PTC have been widely discussed in the literature.

Serrano-Aguilera et al. studied the continuous linear reflectors for flat plate receivers with Inverse Monte Carlo ray-tracing method, where a quasi-planar-concentrated flux distribution is required [2]. Cheng et al. made a 3D numerical study of heat transfer characteristics in the receiver tube of PTC [3], and they then carried out a comparative analysis for PTC with a detailed Monte Carlo ray-tracing optical model [4]. They concluded that the ideal characteristics and optical performance of the PTCs were very different from some critical points determined by the divergence

phenomenon of the nonparallel solar beam [4]. Giannuzzi et al. defined a guideline for steel structures' design and assessment of the components of PTC. Their codes were developed for practical usage and were evaluated under some specific conditions [5]. Liang et al. compared three optical models for the PTC and optimized the geometric parameters according to their models [6]. Cheng et al. optimized the geometrical structure of the PTC based on the particle swarm optimization algorithm and the Monte Carlo ray-tracing method, which found a balance between the calculating speed and result accuracy [7].

With respect to the heat receiver of the PTC, some structures are designed for the PV or PV/T in PTCs [3]. However, tube receivers are more commonly used in PTC combined with thermodynamic cycles [8–10]. In general, two kinds of tubes are commonly utilized in the PTC as the receiver, namely, the vacuum tube [2, 4–10] and the cavity tube [11–13]. The main advantages of the vacuum tube are the high thermal maintenances and low module cost, whereas its structure is frangible. Though a kind of “metal inner and vacuum glass outer” tube is proposed, the connection area of metal and glass is also frangible due to

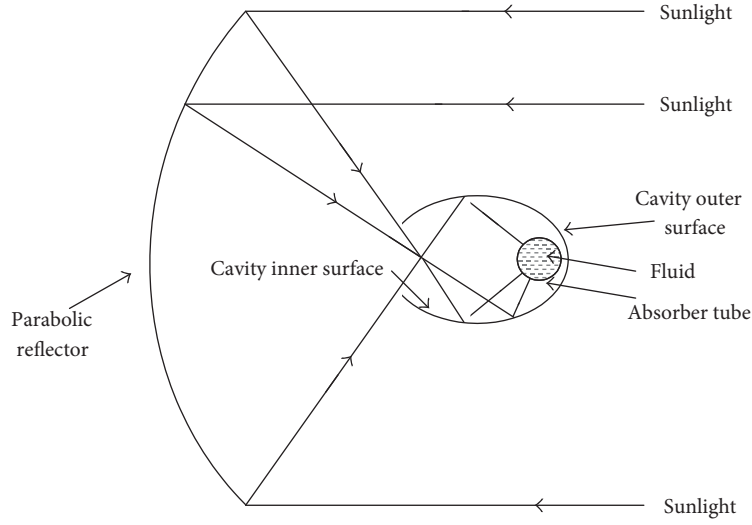
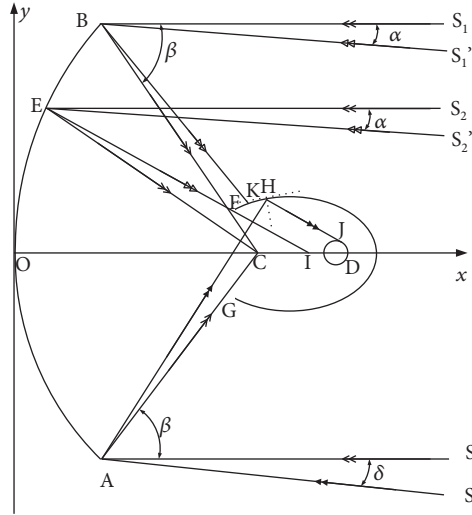


FIGURE 1: Schematic of a cavity tube receiver in the PTC.

FIGURE 2: Sunlight trace in a PTC with an elliptical cavity tube receiver by considering the tracking error angle α under the rectangular coordinate system.

uninterrupted and periodical thermal stress from the inner and outer sides. The other kind of solar receiver is the cavity tube, whose schematic is shown in Figure 1. The outer cover of the receiver is the cavity, with an open inlet towards the parabolic trough reflector. As there is no connection area between the cavity outer cover and the inner absorber tube, this structure is nonfrangible. The incoming lights are reflected by the parabolic reflector and entered the cavity through its open inlet. Sunlight is then reflected for several times and finally reached the tube receiver at the ellipse focus. There are some studies on optical performance of the solar cavity receivers [10–13]. Very limited studies have been presented to the parameter analysis and optimization of the elliptical cavity tube receiver. Considering this, the PTC with the cavity tube receiver is simulated through using the Monte Carlo method. The

TABLE 1: Parameters of the PTC, cavity, and tube absorber.

Parameter/unit	Value
Major axis/mm	100
Minor axis/mm	60
PTC focal distance/mm	800
Elliptic focal distance/mm	80
PTC open width/mm	850
Absorber tube radius/mm	18
Elliptic cavity open length/mm	12

parameters of the PTC with the cavity tube receiver are then discussed. A new geometry is finally proposed according to the parameters' analysis results.

2. Mathematical Models

To track the solar ray in the PTC, the cross section of a PTC with an elliptical cavity tube receiver is established under the rectangular coordinate system as shown in Figure 2. The major axis, minor axis, and the focal distance of the elliptical cavity are A, B, and C in Figure 2, respectively. The open length of the elliptical cavity is L_{el} . The focal distance and open length of the parabolic reflector are f and L_{pr} , respectively. The radius of the tube receiver is r_{tube} . The left focal point of the elliptical cavity is located at the focal point of the PTC. In ideal condition, the sunlight is reflected by the parabolic reflector and concentrated at point C. When the sun tracking error occurs, there is a tracking error angle α in the PTC, which causes part of the sunlight not to be reflected into the cavity, that is, Light $S_1'BK$. There are three representative groups of light paths which can be reflected into the elliptical cavity in Figure 2, namely, the marginal light of the parabolic reflector (i.e., Light $S_1'BC$, $S_2'EC$, and $S_3'AC$), the marginal light of the tube receiver (i.e., Light

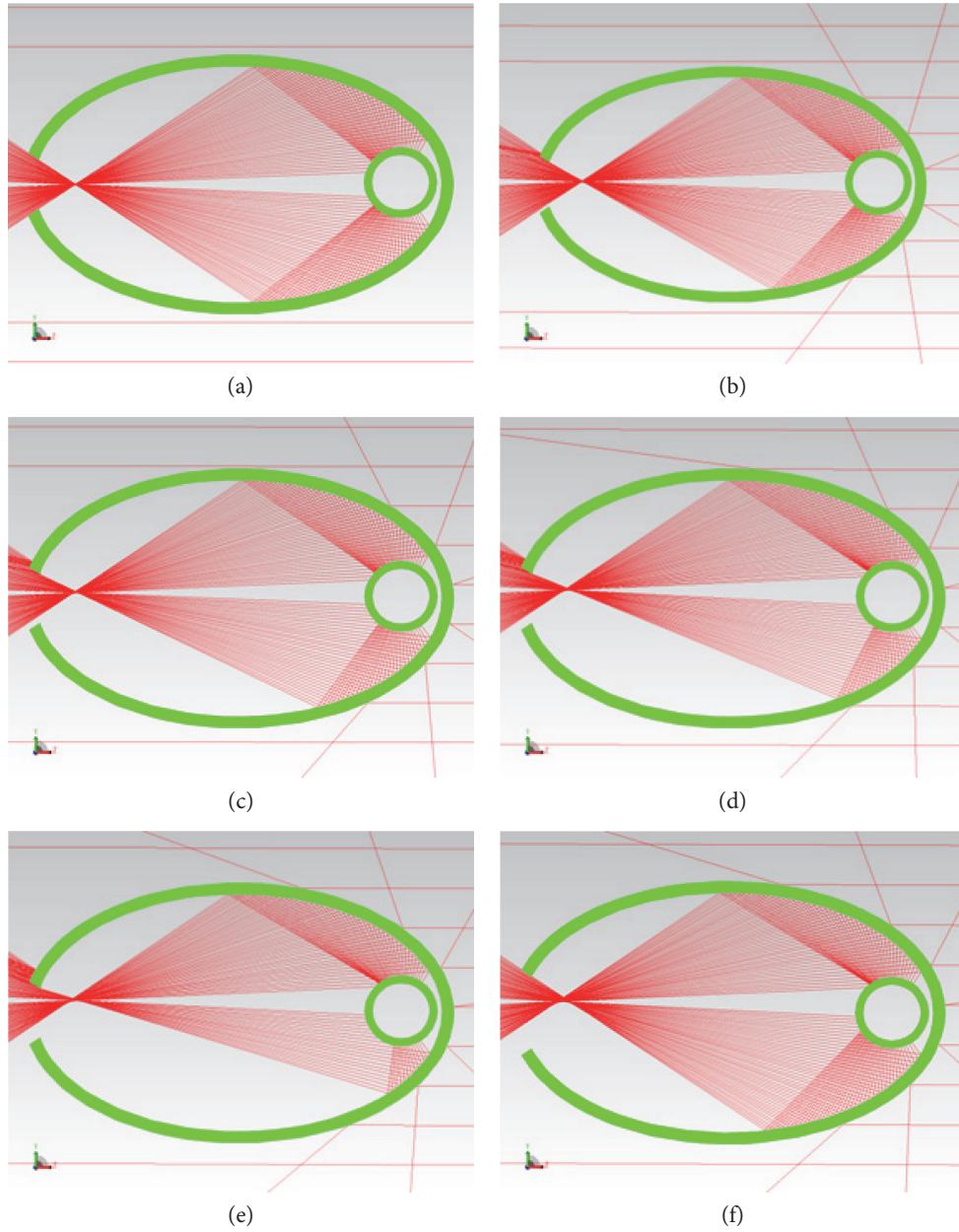


FIGURE 3: Light distribution in the elliptical cavity when (a) under ideal condition; (b) $L_{el} = 12$ mm and $\alpha = 0.05^\circ$; (c) $L_{el} = 12$ mm and $\alpha = 0.1^\circ$; (d) $L_{el} = 12$ mm and $\alpha = 0.15^\circ$; (e) $L_{el} = 12$ mm and $\alpha = 0.2^\circ$; and (f) $L_{el} = 19$ mm and $\alpha = 0.2^\circ$.

S_3 'AHJ), and the light with a tracking error angle of α (i.e., Light S_2 'EFI).

2.1. Tube Receiver. According to Figure 2, the elliptical cavity and the parabolic reflector can be expressed as

$$\frac{(x-f-c)^2}{a^2} + \frac{y^2}{b^2} = 1, \quad (1)$$

$$y^2 = 4fx. \quad (2)$$

The marginal light AC can be expressed as

$$y = k_1(x-f), \quad (3)$$

where

$$k_1 = \frac{-B/2}{(B^2/16)-f}. \quad (4)$$

The angle β between the Light S_3 A and Light AC is

$$\beta = \arctan k_1. \quad (5)$$

The marginal light of the tube receiver AH can be expressed as

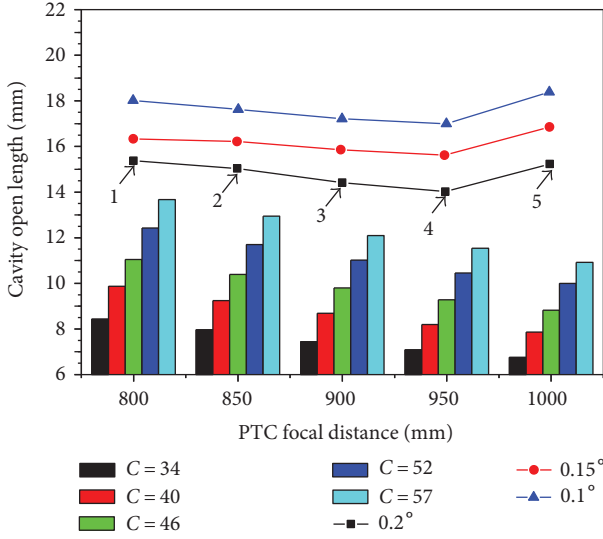


FIGURE 4: Relationship between the PTC focal distance and cavity open length under different concentration ratios and tracking error angles.

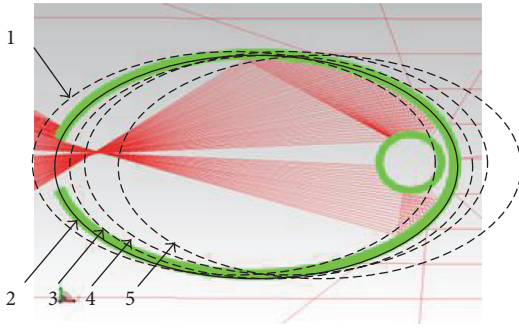


FIGURE 5: Elliptical cavity under different PTC focal lengths when $\alpha = 0.2^\circ$.

$$y = k_2 \left(x - \frac{L_{pr}^2}{16f} \right) - \frac{L_{pr}}{2}, \quad (6)$$

where

$$k_2 = \tan(\delta + \beta). \quad (7)$$

Define point H as (m, n) and the values of m and n can be obtained through (1) and (6). The slope of the tangent light for the tube receiver HJ, which is reflected by the cavity inner surface, is

$$k_4 = \frac{k_2 - k_3 + k_3(1 + k_2 k_3)}{1 + k_2 k_3 - (k_2 - k_3)k_3}, \quad (8)$$

where k_3 is the slope of the tangent light:

$$k_3 = -\frac{b^2(m-f-c)}{a^2 n}. \quad (9)$$

Correspondingly, in order to reach the absorber tube inside the cavity, the relationship between the absorber tube radius and the light slopes is

$$\frac{|k_4(f+2c) - k_4 m + n|}{\sqrt{k_4^2 + 1}} \leq r_{\text{tube}}. \quad (10)$$

2.2. Tracking Error Angle. The Light EC can be expressed as

$$y = k_5(x-f). \quad (11)$$

According to (1) and the open length of the elliptical cavity, the Light EFI with a tracking error angle of α is

$$y = k_6 \left(x - \sqrt{a^2 \left(1 - \frac{L_{el}^2}{4b^2} \right)} - f - c \right) + \frac{1}{2} L_{el}, \quad (12)$$

where k_5 and k_6 are the slopes of Light EFI and Light EC, respectively.

Correspondingly, in order to enter the elliptical cavity, the relationship between the tracking error angle and the light slopes is

$$|\alpha| \leq \arctan \frac{k_5 - k_6}{1 + k_5 k_6}. \quad (13)$$

The concentration ratio in the PTC with the elliptical cavity tube receiver is defined as

$$C = \frac{L_{pr} - 2b}{2\pi r}. \quad (14)$$

The Monte Carlo method is utilized to simulate the light distribution in the elliptical cavity. Equations (1)–(13) are then converted into the Fortran codes to determine the configuration sizes of the elliptical cavity and the tube receiver.

3. Results and Discussion

3.1. Light Distribution in the Elliptical Cavity. Dimensions of the cavity tube receiver are summarized in Table 1. Light distribution in the elliptical cavity is shown in Figure 3. Figure 3(a) shows the light distribution in the cavity under ideal condition. It is found that the light distribution is longitudinally symmetrical. Taking the above half section as an example, some of the incident sunlight is sheltered by the cavity itself, which causes no light reaching the tube receiver at the left of the tube. The other light is reflected by the parabolic reflector, enters the cavity, and reaches the absorber tube, leading to the increase in the heat flux on the tube. After that, the direct light from the cavity open inlet and the reflected light from the elliptic inner surface are merged, generating a peak on the tube. The other reflected sunlight from the elliptic inner surface then reaches the rest tube surface. No light can reach the range at the right of the tube receiver due to the shelter of the tube itself.

Tracking error usually occurs in practical control of PTCs. Four tracking error angles are then considered in Figures 3(b), 3(c), 3(d), and 3(e), respectively. Due to the

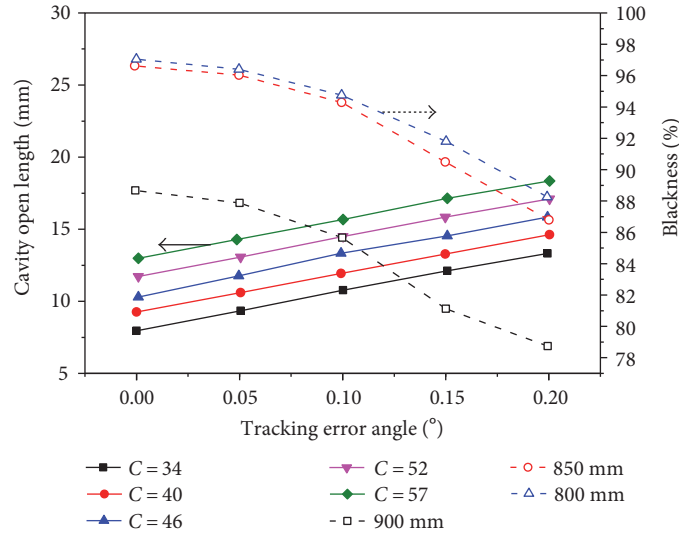


FIGURE 6: The cavity blackness under different tracking error angles, cavity open lengths, concentration ratios, and PTC focal distances.

tracking error, the light distribution on the tube is asymmetrical. Some lights are sheltered by the cavity outer surface. However, the light distribution tendency under ideal condition can also be found in Figures 3(b), 3(c), 3(d), and 3(e), namely, the merged lights directly from the cavity open inlet and reflected from the elliptic inner surface also generate peaks on the above and below half sections of the tubes. On increasing the tracking error angle, more lights are sheltered by the cavity outer surface and less lights reach the below half section of the tube receivers.

The elliptical cavity open length is increased in Figure 3(f). Comparing Figures 3(e) and 3(f), it is found that increasing the cavity open length can allow more lights to enter the cavity. As more sunlight enters, the light distribution on the tube receiver is more close to the ideal condition as shown in Figure 3(a).

3.2. Parameter Analysis. PTC focal distance and cavity open length are two core parameters of the PTC and the cavity tube receiver. Their relationship is discussed in Figure 4. It is found that the PTC focal distance and the tracking error angle have negative correlations with the cavity open length. But the PTC concentration ratio has positive correlation with the cavity open length. When tracking error occurs, on increasing the PTC distance, the cavity open length first decreases and then increases to maintain the concentration ratio. This can be explained by Figure 5. Taking the condition of $\alpha = 0.2^\circ$ as an example, five elliptical cavity locations are shown in Figure 5. It is found that on increasing the PTC focal distance, the elliptical cavity is moved toward right. As the reflected light is first concentrated toward the focal point and then diverges in the cavity, the cavity open length needs to first decrease then increase to allow the light to enter the cavity.

For the cavity tube receiver, the blackness, which is the percentage of the sunlight on the tube receiver surface to the total incident sunlight, is proposed to evaluate the cavity performance. The cavity open length and cavity blackness

under different tracking error angles are shown in Figure 6. It is found that, to a specific PTC and cavity tube receiver, increasing the tracking error angles would decrease the cavity blackness; and in order to maintain the concentration ratio, the cavity open length needs to be enlarged. Under a specific tracking error angle, increasing the PTC focal distance would decrease the cavity blackness. The reason is that more sunlight is sheltered by the cavity outer surface as indicated in Figures 3(b), 3(c), 3(d), and 3(e). Also, when the PTC concentration ratio increases, for example the PTC width increases, the cavity open length needs to be increased to allow more light to transfer into the cavity as indicated by angle β in Figure 2.

3.3. Elliptical Cavity Optimization. According to the discussion above, a flat plate reflector is added at the cavity inlet to enhance the cavity tube receiver performance. The geometry of the proposed cavity is shown in Figure 7(a), and the top flat plate reflector can be described as

$$y = -\tan\beta(x + c). \quad (15)$$

The light distribution in the cavity is shown in Figure 7(b). It is found that the sheltered sunlight is reflected by the flat plate, which can finally reach the tube receiver. The cavity darkness of the new cavity receiver under different tracking error angles and PTC focal distances is shown in Figure 8. According to Figures 3, 6, 7(b), and 8, it is found that introducing the flat plate can largely increase the cavity darkness. The cavity darkness decreases when the tracking error angle increases. But introducing the flat plate reflector breaks the monotonic relationships of the cavity darkness under different PTC focal distances. Moving the elliptical cavity along the long axis direction leads to the incident sunlight reflected by the flat plate under different incident angles, which generates different multireflections inside the cavity, and finally leads to the curves in Figure 8.

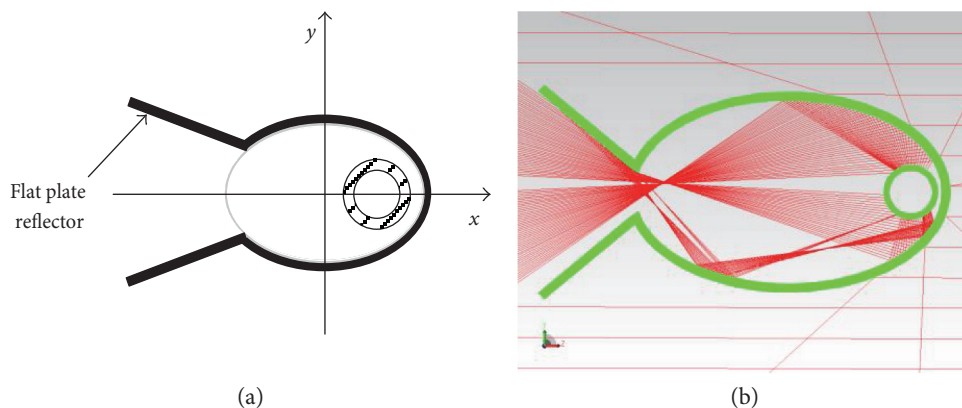


FIGURE 7: (a) Newly proposed elliptical cavity geometry and (b) light distribution in the cavity.

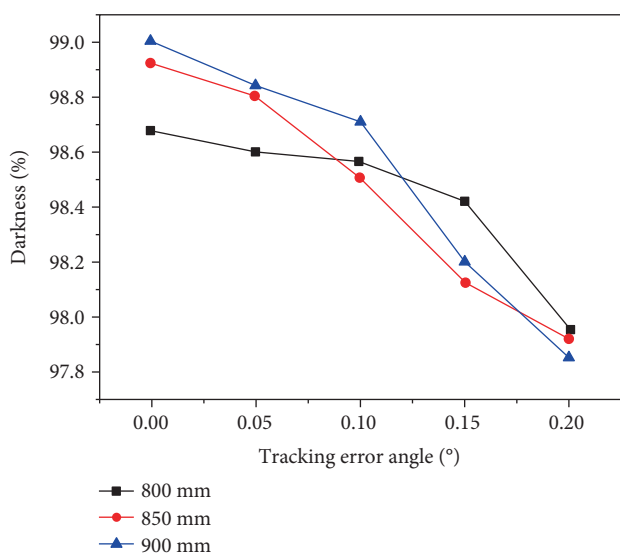


FIGURE 8: Darkness of the newly proposed cavity receiver under different tracking error angles and PTC focal distances.

4. Conclusions

Solar parabolic trough collectors (PTC) are the most widely accepted solar concentration style. The PTC with an elliptical cavity tube receiver has not been well discussed in the literature. In the present study, the light distribution in the cavity under different tracking error angles and PTC configurations are analyzed. A new elliptical cavity geometry is proposed and analyzed. The following conclusions are obtained through this study:

- (1) The light distribution on the tube receiver is asymmetrical. On increasing the tracking error angle, more lights are sheltered by the cavity outer surface and less lights reach the below section of the tube receivers.
- (2) The PTC focal distance and the tracking error angle have negative correlations with the cavity open length, whereas the PTC concentration ratio has positive correlation with the cavity open length. On increasing the PTC focal distance, the cavity open

length needs to first decrease and then increase to maintain the concentration ratio.

- (3) Increasing the tracking error angles would decrease the cavity blackness. Increasing the PTC focal distance would decrease the cavity blackness. Introducing a flat plate reflector at the elliptical cavity open inlet leads to multireflections inside the cavity, which can largely increase the cavity darkness.

Conflicts of Interest

The authors declare that they have no conflicts of interest.

Acknowledgments

This research was funded by the National Natural Science Foundation of China (no.: 51506043), the Fundamental Research Funds for the Central Universities (no.: 2014B19714), and the Applied Basic Research Plan of Changzhou City (no.: CJ20160043).

References

- [1] V. K. Jebsingh and G. M. J. Herbert, "A review of solar parabolic trough collector," *Renewable and Sustainable Energy Reviews*, vol. 54, pp. 1085–1091, 2016.
- [2] J. J. Serrano-Aguilera, L. Valenzuela, and J. Fernandez-Reche, "Inverse Monte Carlo Ray-Tracing method (IMCRT) applied to line-focus reflectors," *Solar Energy*, vol. 124, pp. 184–197, 2016.
- [3] Z. D. Cheng, Y. L. He, J. Xiao, Y. B. Tao, and R. J. Xu, "Three-dimensional numerical study of heat transfer characteristics in the receiver tube of parabolic trough solar collector," *International Communications in Heat and Mass Transfer*, vol. 37, no. 7, pp. 782–787, 2010.
- [4] Z. D. Cheng, Y. L. He, F. Q. Cui, B. C. Du, Z. J. Zheng, and Y. Xu, "Comparative and sensitive analysis for parabolic trough solar collectors with a detailed Monte Carlo ray-tracing optical model," *Applied Energy*, vol. 115, no. 4, pp. 559–572, 2014.
- [5] G. M. Giannuzzi, C. E. Majorana, A. Miliozzi, V. A. Salomoni, and D. Nicolini, "Structural design criteria for steel components

- of parabolic-trough solar concentrators,” *Journal of Solar Energy Engineering*, vol. 129, no. 4, pp. 382–390, 2007.
- [6] H. Liang, S. You, and H. Zhang, “Comparison of three optical models and analysis of geometric parameters for parabolic trough solar collectors,” *Energy*, vol. 96, pp. 37–47, 2016.
- [7] Z. Cheng, Y. He, and D. Baochun, “Geometric optimization on optical performance of parabolic trough solar collector systems using particle swarm optimization algorithm,” *Applied Energy*, vol. 148, pp. 282–293, 2015.
- [8] P. M. Zadeh, T. Sokhansefat, A. B. Kasaeian, F. Kowsary, and A. Akbarzadeh, “Hybrid optimization algorithm for thermal analysis in a solar parabolic trough collector based on nanofluid,” *Energy*, vol. 82, pp. 857–864, 2015.
- [9] G. Kumaresan, R. Sridhar, and R. Velraj, “Performance studies of a solar parabolic trough collector with a thermal energy storage system,” *Energy*, vol. 47, no. 1, pp. 395–402, 2012.
- [10] V. S. Reddy, S. C. Kaushik, and S. K. Tyagi, “Exergetic analysis and performance evaluation of parabolic trough concentrating solar thermal power plant (PTCSTPP),” *Energy*, vol. 39, no. 1, pp. 258–273, 2012.
- [11] F. Chen, M. Liu, P. Zhang, and X. Luo, “Thermal performance of a novel linear cavity absorber for parabolic trough solar concentrator,” *Energy Conversion and Management*, vol. 90, pp. 292–299, 2015.
- [12] F. Chen, M. Liu, R. H. E. Hassanien et al., “Study on the optical properties of triangular cavity absorber for parabolic trough solar concentrator,” *International Journal of Photoenergy*, vol. 2015, Article ID 895946, 9 pages, 2015.
- [13] W. Gao, G. Q. Xu, T. T. Li, and H. W. Li, “Modeling and performance evaluation of parabolic trough solar cavity-type receivers,” *International Journal of Green Energy*, vol. 12, no. 12, pp. 1263–1271, 2015.